UNIVERSITY OF SOUTHAMPTON

FACULTY OF ENGINEERING, SCIENCE AND MATHEMATICS

Optoelectronics Research Centre

Modelling of Capillary High Harmonic Generation

Edward Thomas Foss Rogers

Thesis for the degree of Doctor of Philosophy

September 2008

UNIVERSITY OF SOUTHAMPTON

ABSTRACT

FACULTY OF ENGINEERING, SCIENCE AND MATHEMATICS

OPTOELECTRONICS RESEARCH CENTRE

Doctor of Philosophy

MODELLING OF CAPILLARY HIGH HARMONIC GENERATION

Edward Thomas Foss Rogers

High harmonic generation (HHG) is now an accepted method for laboratory based generation of XUV and soft x-ray light. HHG produces pulses that are highly coherent, with a pulse length in the femtosecond or attosecond timescales. To predict the XUV output from an HHG experiment, both the emission from a single atom and the build-up of intensity over the interaction length must be accounted for. In addition, the propagation of the driving laser pulse in a gas-filled capillary has a significant effect on generation. To improve the understanding of these processes, this thesis presents a spatio-temporal phasematching model for capillary HHG, and a modal-based model of laser propagation in an ionising gas.

The phasematching model takes into account the full spatio-temporal nature of the capillary HHG process to determine the harmonic build-up as a function of radius, time and harmonic number. A very simple single atom response is assumed, consisting of a plateau and hard cutoff. Good agreement is shown between the theoretically predicted and experimentally measured spectra for a number of gases. The model is extended to gas mixtures and shows qualitative agreement with experimental results.

The spatial output of the phasematching model, together with phase information from the semi-classical model, is used to investigate the propagation of the XUV beam as it leaves the capillary. The divergence of the harmonic beam is predicted and found to be in agreement with preliminary experiments.

The modal propagation model (MPM) is simple and computationally fast. The effect of misalignment of the laser into the capillary is investigated and it is shown that radial symmetry can be assumed within the capillary. Predictions of the ionisation fraction as a function of propagation distance show good agreement with experimental measurements of fluorescence.

The MPM assumes that the time envelope of the pulse does not change and the plasma-induced nonlinear mode coupling is weak, and so is valid in the low pressure, low intensity regime. For extension to higher intensities and pressures, a more sophisticated model is proposed that is currently under development.

Contents

List of Figures

List of Tables

DECLARATION OF AUTHORSHIP

I, Edward Thomas Foss Rogers, declare that the thesis entitled "Modelling of Capillary High Harmonic Generation" and the work presented in it are my own. I confirm that:

- this work was done wholly or mainly while in candidature for a research degree at this University;
- where any part of this thesis has previously been submitted for a degree or any other qualification at this University or any other institution, this has been clearly stated;
- where I have consulted the published work of others, this is always clearly attributed;
- where I have quoted from the work of others, the source is always given. With the exception of such quotations, this thesis is entirely my own work;
- I have acknowledged all main sources of help;
- where the thesis is based on work done by myself jointly with others, I have made clear exactly what was done by others and what I have contributed myself;
- parts of this work have been published as:

  S.L. Stebbings, E.T.F. Rogers, A.M. de Paula, M. Praeger, C.A. Froud, B. Mills, D.C. Hanna, J.J. Baumberg, W.S. Brocklesby and J.G. Frey, *Molecular variation of capillary-produced soft x-ray high harmonics*, Journal of Physics B: Atomic, Molecular and Optical Physics, 41(14):145602, 2008.

  E T F Rogers, S L Stebbings, A.M. de Paula, C.A. Froud, M. Praeger, B. Mills, J. Grant-Jacob, D.C. Hanna, J.J. Baumberg, W.S. Brocklesby and J.G. Frey, *Spatio-temporal phasematching in capillary high harmonic generation*, in preparation.

M.Praeger, A.M. de Paula, C.A. Froud, E.T.F. Rogers, S.L. Stebbings, W.S. Brocklesby, J.J. Baumberg, D.C. Hanna and J.G. Frey, *Spatially resolved soft X-ray spectrometry from single-image diffraction*, Nature Physics, 3(3):176-179, 2007.

C.A. Froud, E.T.F. Rogers, D.C. Hanna, W.S. Brocklesby, M. Praeger, A.M. de Paula, J.J. Baumberg, J.G. and Frey, *Soft-x-ray wavelength shift induced by ionization effects in a capillary*, Optics Letters, 31(3): 374, 2006. Also selected for the June 2006 issue of Virtual Journal of Ultra-fast Science, Volume 5, Issue 6, Ultrafast Methods And Measurement Techniques, `www.vjultrafast.org`

Signed: _____

Date: _____

Acknowledgements

It is not possible to get to the end of a PhD without numerous sources of help, advice and encouragement, and a number of people deserve credit for my getting this far.

Bill Brocklesby, my supervisor, who questioned my assumptions and taught me to do the same. The question "Is that a true statement?" is often surprisingly difficult to answer. He has taught me that research is not about finding answers, but asking the right questions.

The other academic staff on this project, Jeremy Frey, Dave Hanna, and Jeremy Baumberg, for inspiration and advice.

Chris Froud and Matt Praeger for answering interminable question about Matlab, and Ben Mills, Richard Chapman, James Grant-Jacob and Tom Butcher for asking the same questions in their turn.

I am very grateful to those who did the experiments, Ana De Paula and Sarah Stebbings, as well as Chris, Matt, Ben, Richard, James and Tom, to give me something to compare my theory to, even if they did sometimes get the 'wrong' results.

Peter Horak, for his advice on nonlinear propagation in waveguides and collaboration on the latest propagation modelling.

My parents for moral support and "encouragement" — usually along the lines of "but Katrine finished ages ago" — and my parents-in-law, who never once compared me unfavourably with my wife...

Finally, my wife, Katrine, who supported the writing of this thesis at the same time as writing her own, and to whom I am indebted for a working knowledge of black hole x-ray binaries — a very different source of x-rays to the ones described here.

"The most exciting phrase to hear in science, the one that heralds new discoveries, is not 'Eureka!' but 'That's funny...' "

Isaac Asimov

Chapter 1

Introduction

The invention of the laser by Maiman [1] and its subsequent development have given scientists access to light intensities much higher than those from any natural process. The interaction of these high intensity light beams with matter shows many more complicated effects than the linear refraction and absorption that had previously been observed. These nonlinear interactions have provided new probes into the nature of matter and light, as well as being the source of many technological developments.

The field of nonlinear optics (NLO) can be traced back to 1961, when Franken *et al.* [2] demonstrated second harmonic generation from the ruby laser line at 694.3 nm to produce a new wavelength in the ultraviolet. This first experiment showed $\sim 10^{11}$ second harmonic photons demonstrated from $\sim 10^{19}$ fundamental photons, an efficiency of $\sim 10^{-8}$. However, shortly afterwards, significant increases in efficiency were achieved [3] by Giordmaine [4] and Maker *et al.* [5]. These experiments paved the way for a whole new field of optics investigating the nonlinear interactions of light and matter. As well as harmonic generation, many other process have been discovered, including four-wave mixing, sum- and difference-frequency generation, parametric amplification, two-photon absorption, self focusing, self phase modulation and stimulated Raman scattering.

Nonlinear optics has been exploited to produce many new optical devices, in-

cluding coherent radiation sources in wavelength regions where lasing is difficult or impossible to achieve, new pulse measurement techniques, mode-locked lasers and pulse compression systems. On the other hand, the light pulses that show these remarkable nonlinear properties are also difficult to control, for exactly that reason. Controlling of unwanted nonlinear effects in laser systems is a significant challenge as, unlike linear optical effects, changes to the pulse due to nonlinear effects are difficult or impossible to reverse.

1.1 The origin of optical nonlinearities

When an electromagnetic wave is propagating through any material, it causes the electrons in that material to oscillate; it is this oscillation that, in turn, generates a new electromagnetic wave which continues to propagate. If the oscillations of the electron in the medium are in a harmonic potential, then the optical system has a linear response to the incoming wave. In this case the effect of the medium on the wave is independent of the amplitude of the wave and the frequency of the wave is unaltered. The only effects of such a linear system on wave propagation are phase delay between the incoming and outgoing waves and damping of the wave. These effects lead to a modified speed of propagation — refractive index — and absorption respectively.

If, on the other hand, the electron binding potential is anharmonic, then the electron motion can exhibit oscillations with a modified frequency, and these oscillations will generate electromagnetic waves with new frequency components.

Consider an electron bound in an arbitrary 1-dimensional potential well $V(x)$ (figure 1.1). If the electron has an equilibrium position at $x = 0$, then a Taylor expansion about the equilibrium point gives

$$V(x) = V(0) + \frac{V'(0)}{1!}x + \frac{V''(0)}{2!}x^2 + \frac{V'''(0)}{3!}x^3 \dots \tag{1.1}$$

where $'$ denotes differentiation with respect to x. $V(x)$ has, by definition, a minimum

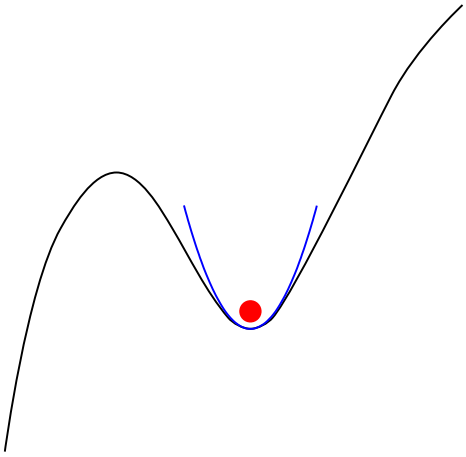

Figure 1.1: *Electron bound in arbitrary potential well (black line) and a parabolic approximation (blue line) to the potential at the equilibrium position.*

at $x = 0$, therefore $V'(0) = 0$. If $V(0)$ is defined as the zero potential, then

$$V(x) \approx \frac{1}{2} V''(0)\, x^2. \tag{1.2}$$

This parabolic approximation is shown as the blue line in figure 1.1. Thus for small displacements about equilibrium, the electron can be treated as a simple harmonic oscillator. In this case, the restoring force on the electron F is given by $F = -\frac{\mathrm{d}V}{\mathrm{d}x} = -V''(0)x$. The net movement of the electron cloud relative to the nucleus (assumed to be fixed), which is called the polarisation of the medium P, is simply

$$P = \epsilon_0 \chi E \tag{1.3}$$

where the electric field E is in the plane of our 1-dimensional potential[1], ϵ_0 is the permittivity of free space and χ is the susceptibility of the medium, related in this case to $V''(0)$.

When this electron is driven by an electromagnetic wave $E = E_0 e^{i\omega t}$ of frequency

[1] In this simple example, the vector nature of E and P and the tensor nature of χ, together with its frequency dependence, are neglected.

ω, it oscillates at frequency ω, and re-radiates at that frequency. The emitted radiation will have a phase lag with respect to the driving radiation, provided the driving radiation is below the resonant frequency of the oscillator, which is the case for normal atoms and optical frequencies. The bulk response of a sheet of emitters with this phase lag gives rise to absorption and a reduced phase velocity in the medium [6]. These quantities can be represented by the (complex) susceptibility χ or the refractive index $n = \sqrt{1+\chi}$ of the medium.

If the oscillations of the electron become larger, as occurs when driven by a larger amplitude wave, then the parabolic approximation to the potential no longer holds. This occurs as the strength of the electric field begins to be comparable to the atomic field strength, which is why the invention of the laser, and the associated increases in peak intensity, was necessary for the observation of most nonlinear phenomena in optics.[2] In this case the polarisation, instead of being linear in E becomes

$$P = \epsilon_0 \left(\chi^{(1)} E + \chi^{(2)} E^2 + \chi^{(3)} E^3 + \dots \right) \tag{1.4}$$

where $\chi^{(2)}, \chi^{(3)}, \dots$ are derived from the higher order terms of the Taylor expansion of V. Considering, for the moment, the simplest case of interaction between a medium with only $\chi^{(1)}, \chi^{(2)} \neq 0$ and an electromagnetic wave with two frequency components $E = E_1(\omega_1) + E_2(\omega_2)$:

$$\frac{P}{\epsilon_0} = \chi^{(1)} E + \chi^{(2)} E^2$$

$$\frac{P}{\epsilon_0} = \chi^{(1)} \Big[E_1(\omega_1) + E_2(\omega_2) \Big] + \chi^{(2)} \Big[E_1(\omega_1) + E_2(\omega_2) \Big]^2 \tag{1.5}$$

$$\tag{1.6}$$

It should be noted that in a symmetric potential $V'''(0) \equiv 0$ and, therefore, $\chi^{(2)} \equiv 0$ as well. This demonstrates the well-known result that it is necessary to have a material without inversion symmetry to obtain processes based on a $\chi^{(2)}$ nonlinearity.

[2] Raman scattering was first obeserved with the use of focused sunlight [7]

Frequency component	Physical process
$2\omega_1$	second harmonic generation of ω_1
$2\omega_2$	second harmonic generation of ω_2
$\omega_1 + \omega_2$	sum frequency generation
$\omega_1 - \omega_2$	difference frequency generation
$\omega_1 - \omega_1$	optical rectification of ω_1
$\omega_2 - \omega_2$	optical rectification of ω_2

Table 1.1: *Summary of the frequency components generated by interaction of a two-frequency (ω_1, ω_2) electromagnetic wave with a material of nonzero $\chi^{(2)}$. The colours correspond to the colours of the terms in equation (1.7).*

Since $E_j(\omega_j) = \frac{1}{2}|E_j|\, e^{i\omega_j t} + \text{c.c.}$ where c.c. is the complex conjugate

$$\begin{aligned}\Big[E_1(\omega_1) + E_2(\omega_2)\Big]^2 = \frac{1}{4}\Big[&|E_1|^2\, e^{i(+\omega_1+\omega_1)t} + |E_1|^2\, e^{i(+\omega_1-\omega_1)t} + \\ &|E_1|\,|E_2|\, e^{i(+\omega_1+\omega_2)t} + |E_1|\,|E_2|\, e^{i(+\omega_1-\omega_2)t} + \\ &|E_1|^2\, e^{i(-\omega_1-\omega_1)t} + |E_1|\,|E_2|\, e^{i(-\omega_1+\omega_2)t} + \\ &|E_1|\,|E_2|\, e^{i(-\omega_1-\omega_2)t} + |E_2|^2\, e^{i(+\omega_2+\omega_2)t} + \\ &|E_2|^2\, e^{i(+\omega_2-\omega_2)t} + |E_2|^2\, e^{i(-\omega_2-\omega_2)t}\Big].\end{aligned} \tag{1.7}$$

This equation shows the number of different frequency components generated in even a simple case. The colours of the terms correspond to their descriptions in table 1.1. As higher order processes become available — i.e. $\chi^{(3)}, \chi^{(4)}, \ldots \neq 0$ — the number of frequency combinations becomes even greater. The complexity is also increased by the fact that, in general, $\mathbf{E}$ and $\mathbf{P}$ are vectors and $\boldsymbol{\chi}^{(n)}$ is a tensor of rank n and dependent on the frequencies of all the fields being mixed.

This description of nonlinearity relies on the motion of the electron being small compared to the potential well that contains it. This allows the Taylor series in V to be truncated after a small number of terms. The next section discusses the effect of laser fields that are strong enough for the perturbative description used here to break down completely.

1.2 High harmonic generation

In the previous description of nonlinearities, the discussion was confined to small oscillations of an electron in a potential well. However, in the case of even stronger electric fields, it is possible for the electromagnetic wave to distort the potential barrier so that the electron is no longer fully confined and has a possiblity of ionising and becoming a free electron. In this regime, the perturbative approach is no longer appropriate, and the effect of the subsequent particle motion must be fully considered. This is the regime of high harmonic generation (HHG).

The standard model of the generation process is the three-step, semi-classical model [8–10]. This model describes the generation process as a series of three steps, each of which can be considered separately: firstly, the atomic potential is distorted by the high intensity fundamental laser field, allowing an electron to undergo quantum mechanical tunnelling to an unbound state; secondly, the electron is allowed to propagate as a classical particle under the influence of the oscillating laser field; and thirdly, the electron can return to the nucleus, recombine with the parent ion, and emit a photon.

Consider an isolated atom in free space where the outermost electron is bound in a spherically symmetric potential. As the atom comes under the influence of a strong laser field, the potential confining the electron is distorted to form a potential barrier (figure 1.2). Some proportion of the electron wavefunction can then undergo quantum mechanical tunnelling through this barrier into free space. This tunnelling is most likely to occur when the distortion to the potential is strongest i.e. at the peak of the laser field. Ionisation is treated in detail in section 2.2.

The wavefunction is now localised in two states, both spatiallly near the ion, but one in the ground state, and one in an unbound state. The unbound part of the wavefunction is then treated as a classical particle and is accelerated by the electric field of the laser. Assuming a linear polarisation for the fundamental, the electron is accelerated away from the ion, and then, as the electric field reverses direction, the electron is slowed and accelerated back (figure 1.3). When the two parts of

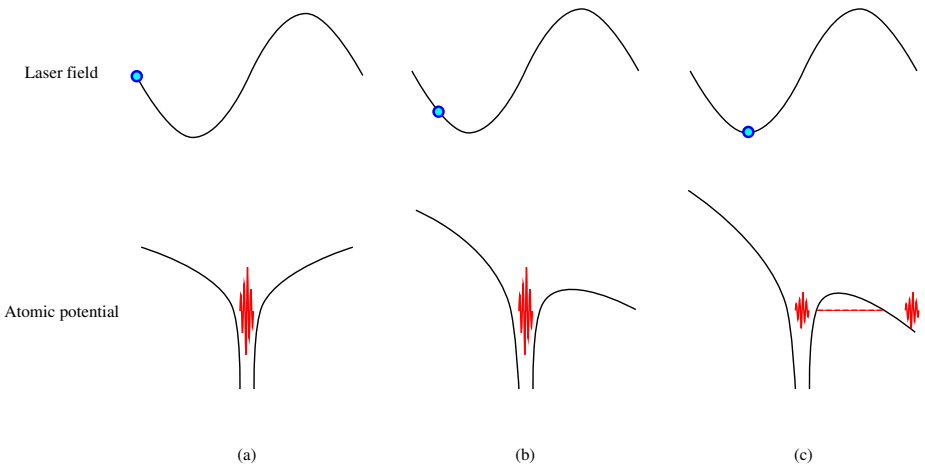

Figure 1.2: *(a) The electron is in a bound state of the atom, the laser field is zero and the potential is undisturbed. (b) A strong electric field is applied by the laser, tilting the potential. (c) Part of the electron electron can tunnel through the potential barrier to an unbound state.*

the wavefunction overlap spatially, the unbound wavefunction has been shifted in frequency (by its change in energy) and so interferes with the bound (unshifted) part of the wavefunction. This interference causes a dipole oscillation which emits a photon at the beat frequency between the two parts of the wavefunction. The energy of the emitted photon is therefore given by the difference in energy between the bound and unbound states. This is equal to the kinetic energy of the travelling electron plus the ionisation potential of the atom;

$$E_{\text{photon}} = \frac{m_e v^2}{2} + I_p, \tag{1.8}$$

where E_{photon} is the energy of the photon, m_e and v are the mass and velocity of the electron respectively and I_p is the ionisation potential of the atom.

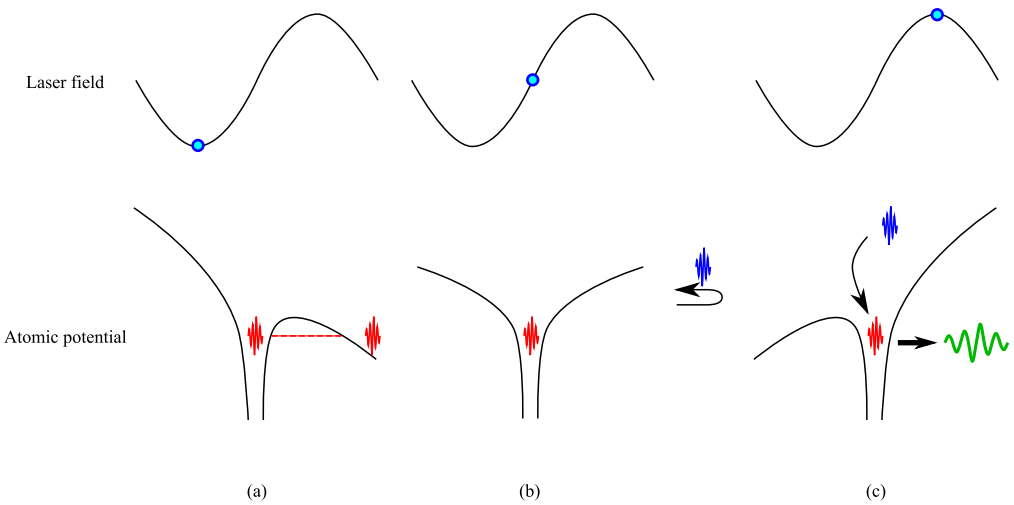

Figure 1.3: *(a) After tunnelling, the electron is accelerated by the laser field. (b) As the electric field reverses direction, the electron is slowed and then accelerated back toward the ion. (c) When the electron returns to the ion, the bound and unbound parts of the wavefunction can interfere, emitting a photon.*

This ionisation-recollision cycle does not directly produce harmonic frequencies, but instead produces a continuous spectrum up to the maximum energy obtainable by the photon. This energy is given by the semi-classical cutoff formula [11, 12]

$$E_{\text{max}} = I_p + 3.17\,U_p \tag{1.9}$$

where $U_p = \frac{e^2 E_0^2}{4\omega^2 m_e}$ is the pondermotive potential. The origin of this formula is discussed in section 2.1.

The harmonic structure is imposed on the spectrum by interference between pulses of extreme ultraviolet (XUV) radiation generated at different times. The ionisation-recollision process is driven by the electric field of the laser and so emits a burst of photons associated with each maximum and minimum of the field. These bursts in time correspond to spikes in frequency space. Since the spikes in time are spaced at $T/2$ where $T = 1/f$ is the period of the fundamental laser, the frequency spikes are separated by $2f$. Since successive time bursts are π rad out of phase (the electron motion is in the opposite direction and therefore the dipole oscillator is out of phase), the harmonics produced are odd, rather than even. This produces harmonics at wavelengths

$$\lambda_q = \frac{\lambda_0}{q} \tag{1.10}$$

where λ_q is the harmonic wavelength, λ_0 is the fundamental wavelength and $q = 1, 3, 5, 7, \ldots$ is the order of the harmonic (the harmonic number).

Further details and the consequences and limitations of this model are discussed in section 2.1

A typical HHG experiment involves focusing a high intensity laser into a gas;[3] either a gas jet near the focus of the fundamental laser, or a waveguide of some form filled with the gas. The gas used in HHG experiments is usually a noble gas, as a high ionisation potential is desirable. Argon, neon and helium are all commonly used [18–22], although some recent work has been carried out, both within this group and elsewhere, to investigate the possibilities of HHG in molecular gases [23–26].

[3]HHG experiments [13–17] have also been carried out on surfaces or thin films, although the mechanism is different from that of HHG in gases.

1.3 Motivation

1.3.1 A table-top system for XUV generation

The ultimate aim of the project of which this thesis is a part, is the development of a table-top system for the generation of XUV pulses. The scientific uses of such a system are widespread, and a number of these are discussed in section 1.3.2. An XUV generation system based on high harmonic generation would provide a relatively cheap and compact source of coherent, short pulse XUV radiation. Alternative XUV generation sources include free electron lasers (FELs) and synchrotrons, however these are large, expensive, multi-user facilities. A HHG system would be a fraction of the cost to build and run, and could feasibly be deployed in a small laboratory for the sole use of one research group.

A qualitative comparison of the specifications of synchrotrons, FELs and HHG sources is shown in table 1.2. Although FELs and synchrotrons remain capable of far higher fluxes of photons than current HHG sources, the HHG source is capable of much shorter pulse lengths, and therefore more accurate time resolution in areas such as electron dynamics that occur on the attosecond timescale [27]. An HHG source also has the benefit of producing, as a byproduct of the generation process, a highly synchronised laser pulse at the fundamental frequency, allowing access to a range of highly accurate pump-probe experiments that are more complicated with synchrotron and FEL sources due to jitter between the XUV and infra-red beams [28].

A parallel investigation, currently being undertaken in the Optoelectronics Research Centre, University of Southampton as part this project [34–36], is to develop a fibre oscillator and amplifier system with sufficient peak intensity to replace the current solid state oscillator and amplifiers. This would further reduce the size, cost and complexity of the generation system and lead to the possible development of a "black box" XUV generation system for use in laboratories where dedicated support for a complex laser system would not be available. This system would have many

Source	HHG Source	Flash FEL	Diamond Synchrotron
Coherence	Coherent	Coherent	Incoherent
Footprint	Tabletop: ~ 5 m^2	45 000 m^2	260 m long
Cost	$\sim$ £3M	$\sim$ €117M [29]	£263M
Pulse length	10 fs–130 as [30]	10–50 fs	ps
Wavelength	2.7–60 nm [20]	6.5–47 nm	0.01–15 nm
Focused spot size	1 µm [21]	25 µm	10 µm

Table 1.2: *Comparison of the specifications of currently available high harmonic generation sources, the FLASH FEL at DESY in Hamburg and the UK Diamond Light Source. FLASH specifications from [31, 32]. Diamond specifications from [33].*

uses in the chemical and biological sciences as described below.

1.3.2 Uses of a short pulse XUV radiation source

A reliable HHG source of XUV radiation could have many uses in a range of scientific fields across the physical and life sciences. Discussing all possible uses is beyond the scope of this thesis, but selected uses are summarised here.

Nanoscale imaging

In general, to image an object with characteristic size l in the far field, it is necessary to use light with a wavelength λ such that $\frac{\lambda}{2} < l$.[4] This is known as the diffraction limit [41]. Therefore, to image objects on the nanometre scale using light, XUV or x-ray radiation is needed. Electron microscopy [42, 43] can also be used to achieve high resolution imaging, but this has a specific set of requirements that limit the available samples. XUV and x-ray imaging also have requirements of the sample, but these are different, making the two approaches complementary.

For example, scanning electron microscopy (SEM) is widely used for imaging of nano-structures, but requires that the imaged object is electrically conducting to avoid a build-up of electrons on the sample surface and subsequent loss of resolution [42, 43]. Non-conductive samples can be coated with a thin layer of gold to meet

[4] In some cases it is possible to overcome this limit, either by imaging using the evanescent field components [37–39], or by using negative refractive index lenses [40].

this requirement, but this is a destructive process as the sample is changed by the preparation. For XUV or x-ray imaging, the sample does not have to be conductive, but it does have to be sufficiently transparent to light of the relevant wavelength that a detectable number of photons can pass through the sample and mount (if used in a transmission imaging geometry).

In both the electron and electromagnetic illumination cases, it is necessary that the sample to be imaged is sufficiently resistant to the effects of the radiation that it survives for long enough for the imaging to be completed. In the case of manufactured nano structures, this is not normally a problem as the structures are relatively robust. However, if the subject of the imaging is a large molecule, as is of interest in the biological sciences, illumination by any particle — electron or photon — of sufficient energy to image the shape of the molecule may cause multiple ionisation of the molecule. As the molecule then contains several positive ions, it will undergo Coulomb explosion [44]. Modelling has shown that the timescale of this explosion is of the order of tens of femtoseconds, so if the entire experiment can be performed in less than 10 fs, the shape of the molecule can be captured before it has time to explode [44, 45]. This single shot imaging experiment, where the sample is destroyed by the illumination, has been demonstrated by Chapman *et al.* [46] on the FLASH FEL using a nanostructured sample.

Currently imaging of biological molecules is carried out at synchrotrons using crystallised molecules, but the crystallisation process can cause complex molecules to change shape. It is also estimated that between 20–40 % of biologically important molecules are difficult or impossible to crystallise [47, 48].

In the case of imaging a sample with an HHG source, the optics required to form a direct image of the sample are difficult to obtain. For example, currently available focusing mirrors have low reflectivities and long focal lengths, requiring long integration times to detect sufficient photons, and large propagation distances to achieve magnification. It would therefore be advantageous if the observed diffraction pattern of the object could be inverted to obtain an image of the sample. The process

for doing this is now well understood [49–52] and has been demonstrated in several experimental regimes [46, 53].

Attosecond probes of electron dynamics

The availability of a high intensity infrared laser beam that is highly synchronised and coherent with the XUV pulse generated by an HHG source allows access to many pump-probe experiments. The potential for generation of a single attosecond pulse allows physical systems to be investigated with an attosecond resolution. These experiments have been proposed and demonstrated in several regimes.

The HHG process can, in itself, reveal considerable information about the atom or molecule used to generate the XUV radiation. Analysis of the emitted radiation and electron spectra has been used to investigate the shape of molecular orbitals [54] and the dynamics of the molecule during the emission process [55].

Alternatively, the generated XUV pulse can be used probe some dynamic system with attosecond resolution. For example, Stockman *et al.* [56] propose an experiment in which a low frequency (near-UV to near-IR) pulse is used to excite a surface plasmon in a metal surface; an attosecond XUV pulse is then used to ionise electrons from the metal surface. The ionised electrons have a velocity that is determined by the local electric field. If the electron energy spectrum is recorded as a function of position, then the local plasmon field strength can be determined as a function of position. If the delay between the pump and probe pulses is varied, the field can determined as a function of position and time with attosecond resolution. A similar experiment has been proposed in gas phase atoms by Hu and Collins [27] in which a helium atom is pumped into an excited state with an ultraviolet pulse, allowed to evolve and probed, after a varying time delay, by an XUV pulse. The energy of the ionised electrons provides information about the relative position of the electrons within the atom at the time of ionisation and so provides an attosecond resolution probe of electron dynamics within an atom.

These experiments allow investigation of physical systems with unprecedented

temporal resolution.

Electromagnetic nonlinearity in the XUV region

One possible use of the high coherence and tight focusing of an HHG source is the investigation of electromagnetic nonlinearity in the XUV regime. For a currently achievable experimental pulse of 10^7 photons/pulse centred at the 25th harmonic of an 800 nm fundamental [57], the energy in the pulse is 3.18×10^{-7} J. Assuming a 10 fs pulse length and a Gaussian focus with $w = 1$ μm, the peak intensity is 1.9×10^{12} W cm^{-2}. The assumption of a 10 fs pulse length underestimates the intensity as the produced XUV pulses are a series of attosecond pulses under a ~ 10 fs envelope. Even with these pessimistic assumptions, this intensity is comparable to that needed to excite nonlinear effects in crystals in the infra-red. As the nonlinearity of materials in the XUV region is not well known, further theoretical and experimental work is needed to determine the feasibility of these experiments, though the first steps have been taken toward this [58, 59].

1.4 Thesis aims

Having discussed the aims and motivation of the project in general, the specific aims of this thesis will now be presented.

In summary, the aims of this thesis are:

- to investigate the effect of phasematching on the high harmonic generation process when carried out in a hollow capillary waveguide; and
- to investigate the effect of propagation of a high intensity laser pulse in an ionising gas with reference to the use of the subsequent pulse for high harmonic generation.

The investigation of phasematching considers the various contributions to the static phasematching problem, namely neutral gas, plasma and waveguiding contri-

butions, and finds the balance between these factors that allows optimum phasematching. The situation in a capillary HHG experiment, however, is more complicated than the simple static case, as there is a spatially and temporally varying ionisation fraction during the generation process. The next step in the modelling, therefore, is to investigate the effect of this dynamic ionisation fraction on the generation process, both spatially and spectrally. The model is valid for various different generation gases and is extended to include gas mixtures. These simulations are then compared with experimental data and used to further the understanding of the HHG process and the factors limiting XUV generation. The model can also be used to make predictions of properties of the XUV radiation, such as the temporal and spatial profile, that can not yet be accurately measured. These results are used to make predictions of the experimental developments required to build a more efficient, tunable and controllable source.

The propagation section looks at the effect of ionisation induced losses in a capillary filled with ionising gas and the subsequent spatial reshaping. Coupling into the capillary is investigated to give a greater understanding of the effect of capillary misalignment. The model enables the investigation of previously observed [60, 61] mode beating effects and their dependence upon the coupling conditions at the capillary entrance. Comparison with experimental observations of the number of ions in the capillary and experimentally measured capillary transmissions is used to validate the model. This simple model guides the development of a more complex model to include temporal and spectral effects that the simple model cannot include. The output of these models can then be used as input to the phasematching model already developed.

Chapter 2

Background work

Before undertaking the development of the models described in chapters 3, 4 and 5, several areas of background theory must be understood. These are discussed in this chapter. Section 2.1 describes the semi-classical, three-step model and looks at the predictions that can be made using it. Section 2.2 presents the models used to predict the levels of ionisation caused by the interaction of a high intensity laser with a gas. This is followed by a review of the modes of a hollow capillary waveguide and their properties in section 2.3. A brief description of the experimental arrangement is given in section 2.4, followed by a description of the gas flow and pressure profiles in the experimental capillary (section 2.5). The last section in this chapter discusses the methods used for determining the refractive index of gases in the infrared and XUV spectral regions.

2.1 Semi-classical model

As described in the introduction, the most intuitive model of the HHG process is the semi-classical model where the electron undergoes quantum-mechanical tunnelling[1] in which a proportion of the electron wavefunction is ionised to free space. The ionised electron is then treated as a classical particle in free space and is accelerated

[1]The probability of tunnelling is discussed quantitatively in section 2.2.

by the laser field. Depending on the instantaneous properties of the driving laser at the time of emission, the electron can return to its parent ion and interfere with the part of the wavefunction that remains in the atom. This interference produces a dipole oscillation at the beat frequency of the two wavefunctions and emits a photon. The energy of this photon is determined by the kinetic energy of the electron at recombination plus the ionisation energy of the atom. Since ionisation is localised in time at the peak of the laser field, this ionisation-recollision process generates a burst of x-rays associated with each peak of the driving electric field. Consequently, one burst is generated every half cycle of the driving laser pulse. The interference between these bursts produces the characteristic HHG spectrum consisting of odd harmonics of the fundamental laser.

The semi-classical model can provide useful information about the phase of emission from a single atom, and qualitative information about the emitted spectrum. However, he model cannot make quantitative predictions of the efficiency of generation or the strength of the electric field, as that requires knowledge of the strength of the dipole oscillator created at recombination. This dipole strength can only be obtained from quantum mechanical modelling of the system. The model also conceptually fails to explain coherent processes, such as phasematching effects, if the recombination process is described as 'emitting a photon'. To explain these effects, the coherent summation of field over all the created dipole oscillators must be considered.

This section presents calculations within the limitations of the semi-classical model to provide an understanding of the factors affecting HHG. All calculations in this section are carried out under the adiabatic approximation; that is, the envelope of the electric field varies slowly on the timescale of an optical cycle. This approximation has been shown to be valid for pulses with a central wavelength of 810 nm (or less) and durations longer than 27 fs [62]. For the case of the 35 fs Gaussian pulse used here, the fractional change in electric field over any 1 optical cycle is less than 1 %.

2.1.1 Free space motion

This section considers the motion of the electron after tunnelling. The laser field as a function of time $\mathbf{E}(t)$ is assumed to be linearly polarised in the x direction with angular frequency ω and amplitude E_0. This gives

$$\mathbf{E}(t) = E_0 \cos(\omega t)\hat{\mathbf{x}}. \tag{2.1}$$

By integrating the (classical) equations of motion, a classical position and velocity for the electron as a function of time is obtained (assuming that the electron tunnels into free space at time t_0 with $\mathbf{x}(t_0) = 0$ and $\mathbf{v}(t_0) = 0$):

$$\begin{aligned}
\mathbf{v}(t) &= \int_{t_0}^{t} \mathbf{a}(t')\,\mathrm{d}t' \\
&= \int_{t_0}^{t} \frac{-e\mathbf{E}(t')}{m}\,\mathrm{d}t' \\
\mathbf{v}(t) &= v_0\big[\sin(\omega t) - \sin(\omega t_0)\big]\hat{\mathbf{x}}
\end{aligned} \tag{2.2}$$

$$\begin{aligned}
\mathbf{x}(t) &= \int_{t_0}^{t} \mathbf{v}(t')\,\mathrm{d}t' \\
\mathbf{x}(t) &= \big\{x_0\big[\cos(\omega t_0) - \cos(\omega t)\big] + v_0 \sin(\omega t_0)\big[t_0 - t\big]\big\}\hat{\mathbf{x}},
\end{aligned} \tag{2.3}$$

where e and m are the electronic charge and mass respectively, $v_0 = -eE_0/m\omega$ and $x_0 = -eE_0/m\omega^2$. Note that the nucleus of the atom/ion is defined to be at position $x = 0$.

For HHG to occur, the electron must be accelerated away from the nucleus, then return to its original position, $x = 0$, in order to recombine and emit the required high energy photon (as in figure 1.3). Therefore, the interesting property of the electron is its kinetic energy as it returns to the nucleus. Only the first return of the electron to the nucleus is considered here as a) for most tunnelling times, the electron only passes the nucleus once (figure 2.1) and b) if the electron does pass

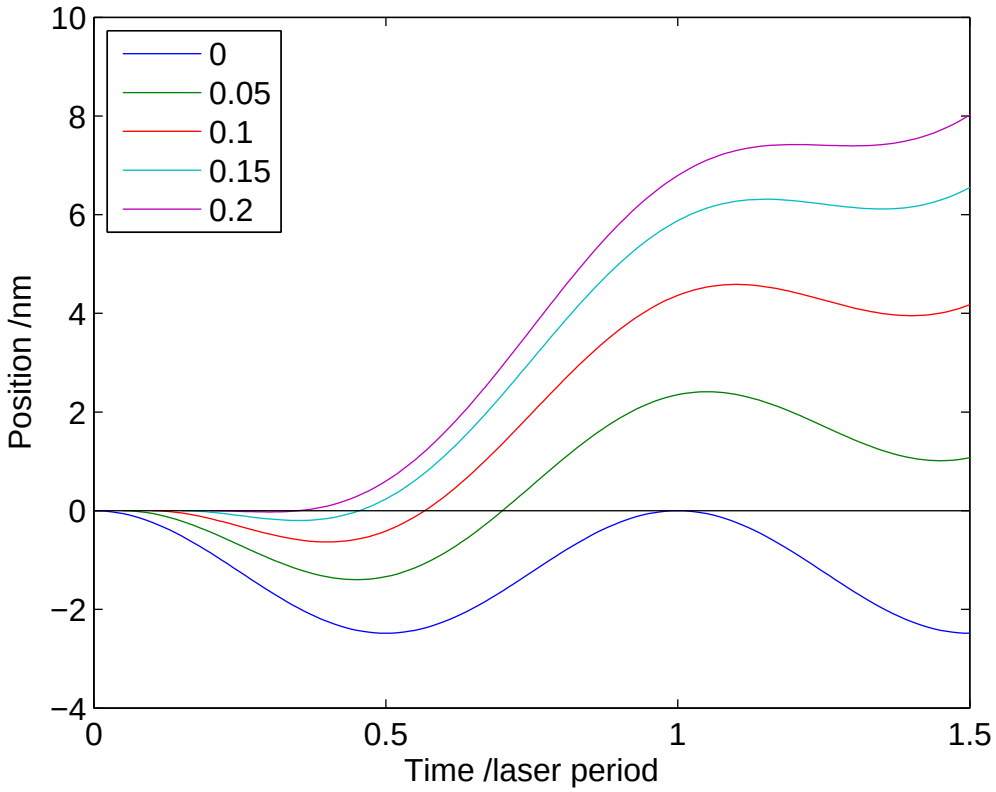

Figure 2.1: *Electron position as a function of time for varying tunnelling times.*

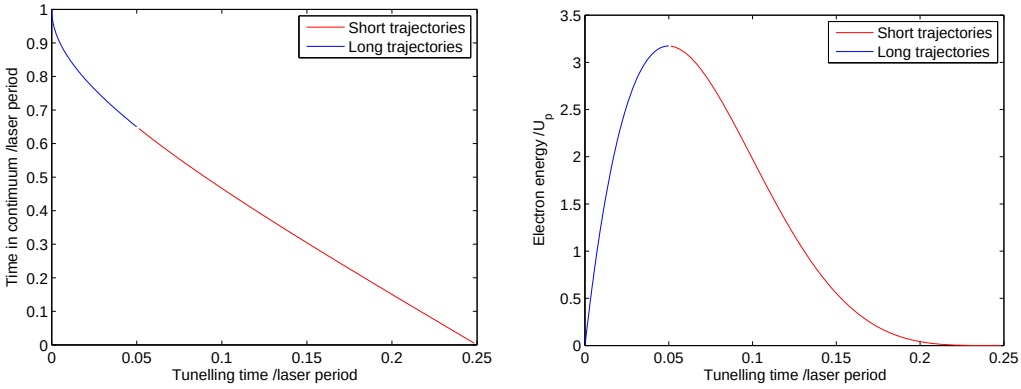

(a) Time spent in the continuum (b) Kinetic energy

Figure 2.2: *Time spent in the continuum τ and kinetic energy of the electron as it returns to its parent ion for the first time as a function of tunnelling time t_0.*

the nucleus a second time, the recombination probability is greatly reduced. This reduction in probability can be thought of as being due to the spreading of the electron wave-packet over time [8, 63].

Figure 2.1 illustrates the paths of electrons for various different tunnelling times (calculated from equation (2.3)). The return time t_1 is found by solving equation (2.3) for t given $x = 0$. Following the approach of Lindner *et al.* [64], the following relationship is found (plotted in figure 2.2(a)) between the tunnelling time t_0 and the time spent in the continuum $\tau = t_1 - t_0$

$$\tan(\omega t_0) = \frac{\omega\tau - \sin(\omega\tau)}{1 - \cos(\omega\tau)}. \tag{2.4}$$

To calculate the kinetic energy, the return time is calculated by solving equation (2.4), and this is used to calculate the velocity using equation (2.2). This gives the graph in figure 2.2(b). The energy unit in this graph is the pondermotive energy given by

$$U_p = \frac{e^2 E_0^2}{4\omega^2 m_e}, \tag{2.5}$$

which is the average kinetic energy of an electron oscillating in an electromagnetic field of amplitude E_0 and angular frequency ω. This graph shows the peak value of

the kinetic energy at 3.17 U_p, and the time at which this peak occurs, 0.05 T (where $T = 2\pi/\omega$ is the laser period). This peak in energy gives the maximum possible energy of the emitted photon. From equation (1.8) it can be deduced that

$$E_{\max} = I_p + 3.17\,U_p. \tag{2.6}$$

The factor 3.17 is found to be independent of the properties of the atom or laser involved, as has been shown previously in, for example, [11, 12]. In this way a simple expression for the maximum value of the frequency of the emitted photon is obtained, based only on the ionisation potential of the atom used for generation and the field strength and frequency of the fundamental laser.

The other significant feature of figure 2.2(b) is that for each return energy, there are two possible tunnelling times and therefore two possible trajectories for the electron to follow. Physically, the two trajectories occur because electrons tunelling early and late in the pulse can reeturn with the same velocity, and hence emit the same frequency photon. By comparison with figure 2.2(a), it is seen that all those trajectories where tunnelling occurs after 0.05 T spend less time in the continuum than those tunnelling before 0.05 T. It is conventional therefore to divide the possible trajectories of the electron into two groups: short trajectories, with $t_0 > 0.05\,T$; and long trajectories, with $t_0 < 0.05\,T$. It will be seen in section 2.1.3 that the phase acquired during electron propagation can be very different for these two trajectories, so single atom models of HHG must consider possible interference between these two paths [65].

It has been shown [9, 12] that full quantum mechanical modelling of the ionising and travelling electron in a laser field recovers the semi-classical approximation. It is shown the most significant contributions to the dipole oscillator come from those electrons that tunnel into the continuum with momentum equal to 0 and return at the times predicted by the semi-classical model. This demonstration of equivalence gives greater weight to the predictions of the semi-classical model and allows them to be used with greater confidence.

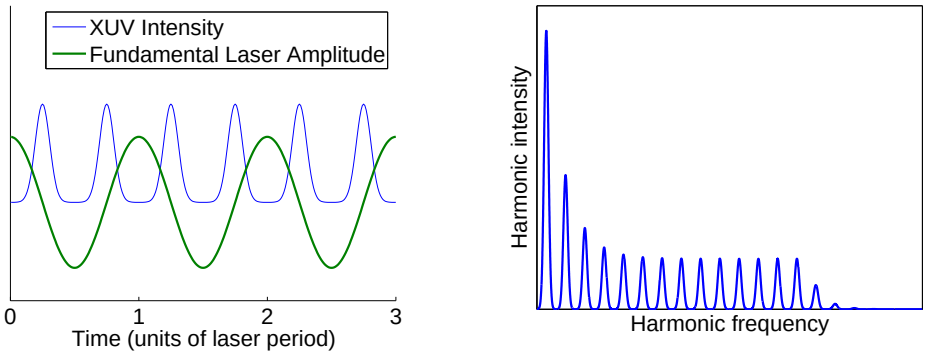

(a) (b)

Figure 2.3: *(a) Schematic of XUV intensity as a function of time, with one spike every half cycle of the fundamental laser. (b) An idealised high harmonic spectrum; only odd harmonics are seen. The typical pattern is a sharp drop over the first few orders followed by a plateau region of constant intensity, then a sharp cutoff as the maximum energy limit (equation (2.6)) is reached.*

2.1.2 Semi-classical predictions of emitted spectrum

Considering only the semi-classical model, qualitative predictions of the high harmonic spectrum can be made, but quantitative predictions are limited by lack of knowledge of the dipole oscillator properties, which can only be determined by quantum mechanical modelling. The XUV intensity in the time domain is a series of spikes, one every half laser cycle (figure 2.3(a)). When the Fourier transform of this time domain signal is taken, the result in the frequency domain is a series of harmonics of the fundamental frequency. Since the spikes occur twice in a laser cycle in the time domain, they are at double the expected frequency spacing (i.e. only even or odd harmonics are produced). Since alternate XUV emission events have a π phase shift with respect to each other (the returning electrons are recombining from opposite directions), the odd harmonics are produced. The phenomenon of the sharp cutoff in figure 2.3(b) is explained by the maximum photon energy derived in equation (2.6). The probabilities of obtaining energies up to this value are roughly equal, but any energy greater than $E_{\max}$ is not attainable.

2.1.3 Semi-classical predictions of phase

The semi-classical model can be used to obtain accurate predictions of the phase of the dipole oscillator created at recombination [65], and hence of the emitted harmonic photon. The phase is given by the integral of the classical action [9]. From [64] we have

$$\phi = \frac{S\left(t_0, t_1\right)}{\hbar} + q\omega t_1, \tag{2.7}$$

where ϕ is the phase of the emitted photon and

$$S\left(t_0, t_1\right) = \int_{t_0}^{t_1} \left(\frac{m_e v(t)^2}{2} + I_p\right) \mathrm{d}t. \tag{2.8}$$

The first term in equation (2.7) comes from the phase advance of the electron between emission and recombination. The angular frequency ω of the electron is given by $\omega = \frac{\mathcal{E}}{\hbar}$ where $\mathcal{E}$ is the total energy of the photon. The phase advance is then given by the integral of ω over time. The second term comes from the phase advance of the fundamental from time $t = 0$ to the emission time t_1. This equation has been shown to be valid by the qunatum mechanical models of Lewenstein *et al.* [9, 65].

Given equation (2.7) and the electron energies and times calculated above, it is possible to produce plots of harmonic phase as a function of tunnelling time (figure 2.4(a)) and return energy (figure 2.4(b)). The result of this dependence of phase on photon energy — via the return time — and on momentum, is that the phase of the emitted photon is dependent on both the harmonic energy and the driving laser intensity.

The dependence of electron phase on energy and driving intensity is transferred to the emitted photon, and so each harmonic generated by the laser has a different radial phase profile induced by radial variation of driving intensity. These intensity profiles are discussed in more detail in section 4.4.1. As seen in figure 2.5, the phases are approximately linear with intensity, but more importantly, the short trajectory has a much weaker intensity dependence than the long trajectory. This means

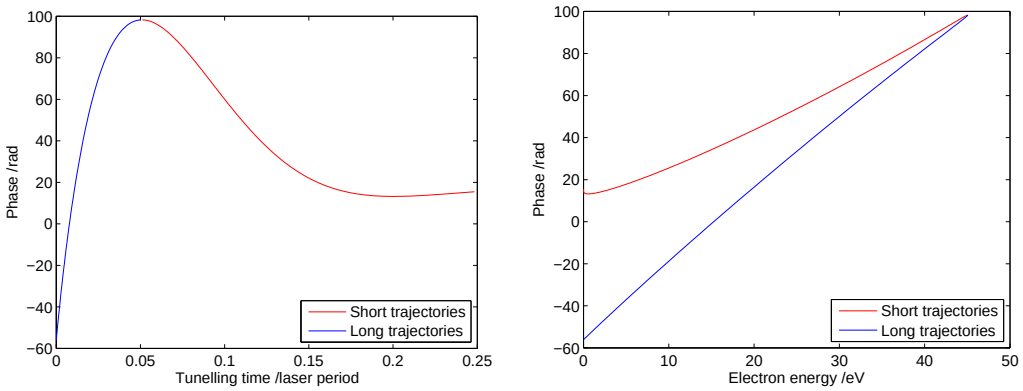

(a) (b)

Figure 2.4: *Phase of the emitted photon as a function of (a) time and (b) electron return energy. These are calculated for a laser intensity of* 2.5×10^{14} W cm^{-2}.

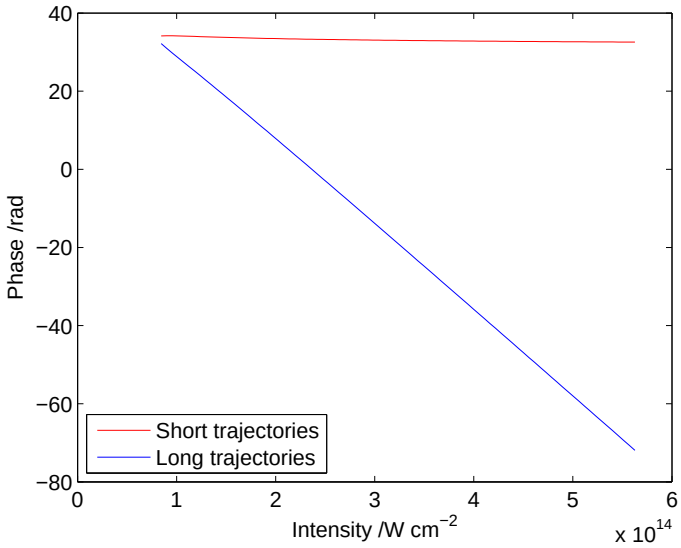

Figure 2.5: *Phase acquired by the electron, during motion, as a function of driving laser intensity. This is calculated for generation of the 19th harmonic in argon.*

that the variation of phase with radius will be smaller for the short trajectories. Therefore, the XUV radiation generated by the short trajectories will have flatter phase fronts and a lower divergence than that generated by the long trajectories.

2.2 Ionisation theory

As described in section 2.1, HHG can only occur when an atom of the generation medium is ionised. Also, ionisation of the medium changes the refractive index and so affects the propagation characteristics of electromagnetic fields in the medium. Therefore, to understand the HHG process, it is necessary to be able to calculate the ionisation of the medium at a given time during irradiation by a laser pulse.

There are three regimes of ionisation for an atom (or ion) in a strong field: multiphoton ionisation (MPI), where the absorption of multiple photons causes ejection of an electron; tunnelling ionisation, in which the potential barrier of the atom is distorted by the applied electric field so that quantum mechanical tunnelling is possible; and barrier suppression ionisation (BSI), in which the potential barrier is so distorted that the electron can simply pass over the top of it (causing ionisation within about one optical cycle [66]).

2.2.1 Tunnelling ionisation

The theoretical study of ionisation of atoms in a high intensity, oscillating electromagnetic field has been underway for many years, and is covered exhaustively in the literature. The work starts with that of Keldysh [67], and a comprehensive review of the development is given by Popov [68]. Here, the equations used are taken from [68] as they are relatively simple to apply to the experiment described. Much of the other work in this area uses the 'ADK' ionisation theory [69], but there are some doubts as to the accuracy of this method (see Appendix 13.3 of [68]). In actual fact, the two calculations give similar results (figure 2.6), so the choice is not particularly significant.

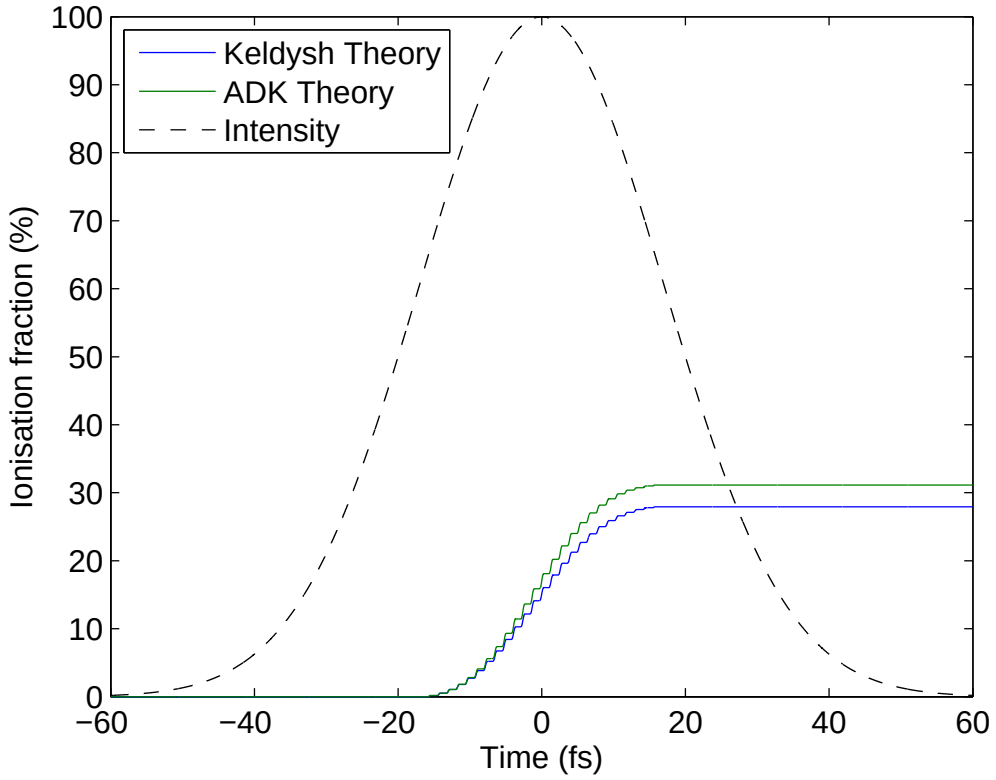

Figure 2.6: *Comparison of ionisation fraction as calculated using ADK theory [69] and Keldysh theory [68] for a* 40 fs *pulse with a peak electric field of* 4.1×10^{10} V m^{-1} *and peak intensity of* 2.2×10^{14} W cm^{-2}. *These parameters are in the tunnelling regime, but below the threshold for BSI. The black dotted line shows the normalised intensity of the pulse. The results of the two calculations are similar, particularly in the* 1–10 % *region where HHG is phasematched.*

In order to determine whether the dominant regime is that of tunnelling ionisation or MPI, it is necessary to consider the value of the Keldysh parameter γ, given by [70]:

$$\gamma = \frac{\omega\sqrt{2m_e I_p}}{eE}, \tag{2.9}$$

where ω and E are the angular frequency and field strength of the driving laser respectively; m_e and e are the electron mass and charge; and I_p is the ionisation potential of the atom in question. The Keldysh parameter is the ratio of the optical frequency to the tunnelling frequency. If the optical frequency is high and the field is weak ($\gamma \gg 1$), the electron oscillations in the potential well must be considered and MPI is a more appropriate description of the ionisation process. If the frequency is low compared to the field strength ($\gamma \ll 1$), then the electron can be treated as a particle in a quasi-static field and tunnelling ionisation is the more appropriate description.

For argon, $\gamma = 1$ at an electric field strength of 3.2×10^{10} V m^{-1}, which is lower than the peak field of the experimental pulses. Therefore, in the experimental regime used in the project, the dominant ionisation effect is that of tunnelling ionisation with $\gamma \ll 1$. The contribution to the ionisation rate from MPI is negligible and so is not modelled. As shown experimentally in, for example, [71], the ionisation rates in the MPI regime are at least an order of magnitude lower than those in the tunnelling regime.

From [68] we have the rate of tunnelling ionisation:

$$w(F,\omega) = \kappa^2 C_{\kappa l}^2 \sqrt{\frac{3}{\pi}}\,(2l+1)\,\frac{(l+m)!}{2^m m!\,(l-m)!}\times 2^{2n^*-m} F^{m+1.5-2n^*} \exp\left[-\frac{2}{3F}\left(1-\frac{1}{10}\gamma^2\right)\right] \tag{2.10}$$

where:

- Z is the charge of the ion *after* ionisation,
- $\kappa = \sqrt{I_p/I_H}$,

- $F = E/\kappa^3 E_a$ is the reduced field,
- l and m are the angular momentum and magnetic quantum numbers of the atom respectively,
- $n^* = Z/\kappa$ is the effective principal quantum number,
- and $C_{\kappa l}$, which is of order unity, is the dimensionless asymptotic coefficient of the atom wavefunction away from the nucleus. This modifies of the ionisation rate based on the shape of the bound electron wavefunction at large distances from the nucleus. (This can be taken from a handbook [72], or from the table for common atoms and ions given in [68].)

The constants in the above equations are: $I_H = 13.6$ eV, the ionisation potential of the hydrogen atom and $E_a = 5.14 \times 10^9$ V m^{-1}, the atomic unit of field strength. The ionisation rate is given in the atomic unit of frequency, 4.13×10^{16} s^{-1}. As stated above, this is the equation for tunnelling ionisation, and so is valid only in the regime $\gamma \ll 1$.

2.2.2 Barrier suppression ionisation

The intensity threshold for barrier suppression ionisation (BSI) is given, in W cm^{-2}, by [73]

$$I_c = 4 \times 10^9 \left(\frac{I_p^4}{Z^2} \right) \tag{2.11}$$

where Z is the residual charge on the ion after ionisation, and I_p is the ionisation potential in eV. This equation can be derived by finding the combined potential of the laser and the atom, assuming that the attraction between the electron and residual ion is purely Coulombic. This potential has a barrier which is equated to the ionisation potential of the atom. When the laser intensity is greater than I_c, the potential barrier falls below the ionisation potential.

This effect is included in the ionisation calculations by setting the ionisation fraction to 1 when an intensity greater than I_c is reached. For argon, this intensity is 2.5×10^{14} W cm^{-2}, and so is reached by the experimental pulse. However, regions

of space and time where BSI has occurred do not contribute to XUV generation.[2]

2.2.3 Applicability of Keldysh theory to molecules

Keldysh theory as described above has been derived for atoms, and so is not generally applicable to molecules. Tong *et al.* [74] have proposed a method for extending Keldysh theory to molecules. However, for the experiments presented here, the two molecules of interest are nitrogen (N_2) and nitrous oxide (N_2O). The theory proposed in [74] is applicable only to diatomic molecules, and so does not apply for nitrous oxide. When Tong *et al.* compare the predictions of their theory to the experiments of Guo *et al.* [75], they find that the agreement is poor for nitrogen. From examination of the data presented in [74] it is seen that, for pulse lengths of ~ 30 fs, as used here, a better approximation is made by assuming that the ionisation rate of nitrogen is the same as that of argon. Therefore, the ionisation properties of nitrogen in the Keldysh model will be assumed to be the same as argon, with the exception of the well known [76] ionisation potential.

For nitrous oxide, the situation is complicated by the fact that no suitable theory has been found. Here it is assumed the Keldysh theory can be applied to nitrous oxide, with the appropriate ionisation potential. This is not ideal, and will introduce errors into the calculations for nitrous oxide, but it is hoped that useful information about the phasematching in more easily ionised gases will still be obtained.

2.3 Modes of a hollow capillary

To generate high harmonics in our experiments, the nonlinear medium used is a gas-filled capillary waveguide. The details of the capillary are discussed in sections 2.4 and 2.5. Use of the capillary gives an extended interaction length between the laser and the gas at high intensity, and adds an extra means to control the generation process. In order to understand the propagation of the laser in the capillary, it is

[2] If BSI is reached, the plasma fraction becomes large, so that phasematching is not possible. See section 3.3 for details.

necessary to know the properties of the modes of the capillary in which the laser travels.

The eigenmodes of a hollow capillary waveguide were first reported by Marcatili and Schmeltzer [77]. In this work, our interest is in the electric field profiles and (complex) propagation constants of those modes which are excited in the experimental arrangement. Since the laser used here is linearly polarised, only linearly polarised capillary modes will be excited [78, 79]. Marcatili divides the modes into three categories: transverse circular electric (TE_{0m}), those with radial and axial components of electric field equal to zero; transverse circular magnetic (TM_{0m}), those with radial and axial magnetic field components equal to zero; and hybrid modes (EH_{nm}) with all field components non-zero. Linearly polarised modes must have both radial and azimuthal components. Therefore, neither the TE nor the TM modes can be linearly polarised.

For the EH_{nm} modes, [77] gives

$$E_{\theta,nm} = J_{n-1}\left(u_{nm}\frac{r}{a}\right)\cos\left(n\theta+\phi\right) \tag{2.12a}$$

$$E_{r,nm} = J_{n-1}\left(u_{nm}\frac{r}{a}\right)\sin\left(n\theta+\phi\right), \tag{2.12b}$$

where $E_{\theta,nm}$ and $E_{r,nm}$ are the electric field components in the azimuthal and radial directions respectively, J_p is the pth order Bessel function of the first kind, u_{nm} is the mth root of the equation $J_{n-1}(u_{nm}) = 0$, ϕ is an arbitrary constant, and a is the capillary radius. Converting into Cartesian coordinates

$$E_{y,nm} = J_{n-1}\left(u_{nm}\frac{r}{a}\right)\cos\left(\left[n-1\right]\theta+\phi\right) \tag{2.13a}$$

$$E_{x,nm} = J_{n-1}\left(u_{nm}\frac{r}{a}\right)\sin\left(\left[n-1\right]\theta+\phi\right). \tag{2.13b}$$

For the case of $n = 1$ these are seen to give a linearly polarised mode. However, the mode is not linearly polarised for any single mode EH_{nm} for $n \neq 1$. If ϕ is chosen to be zero, the modes a polarised in the y direction ($E_{x,1m} = 0$). However, since

any choice of ϕ is valid, the polarisation direction of the modes will be set by the polarisation of the input beam.

The boundary conditions necessary to derive equations (2.12) and (2.13) are the that the mode be finite in the centre of the capillary and $E(r) \to 0$ as $r \to \infty$, together with the condition that the tangential components of the electric and magnetic fields must be continuous at the waveguide boundaries. Two simplifying assumptions have also been made:

$$\frac{2\pi\lambda}{a} \ll \nu u_{nm} \tag{2.14a}$$

$$\left|\frac{\gamma}{k} - 1\right| \ll 1 \tag{2.14b}$$

where ν is the refractive index of the guide, λ is the wavelength of the guided light, $k = 2\pi/\lambda$ is the vacuum wavenumber and γ is the complex propagation constant of the guided mode. Inequality (2.14a) restricts the wavelength of the light to be much smaller than the capillary radius. Inequality (2.14b) restricts the analysis to low-loss modes: those where the propagation constant is nearly equal to that of free space.

In this work the only capillary modes of interest are the hybrid EH_{1m} modes.[3] For these modes the electric field profile is given by

$$E_{y,1m} = J_0\left(u_{1m}\frac{r}{a}\right) \tag{2.15a}$$

$$E_{x,1m} = 0. \tag{2.15b}$$

The intensity profiles of the first four of these modes are shown in figure 2.7.

For the EH_{nm} capillary modes in a non-absorbing dielectric waveguide with refractive index ν, the complex propagation constant $\gamma_{nm} = \beta_{nm} + i\alpha_{nm}$ is given

[3]There also exist combinations of degenerate modes that are linearly polarised, these are discussed in section 2.3.1.

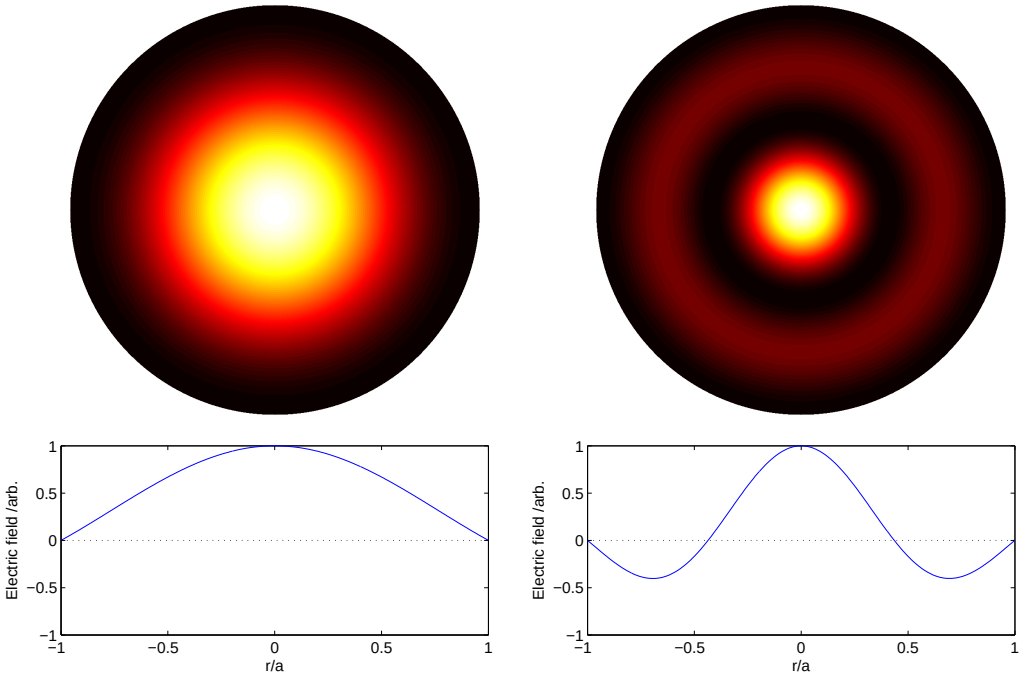

(a) EH_{11} (b) EH_{12}

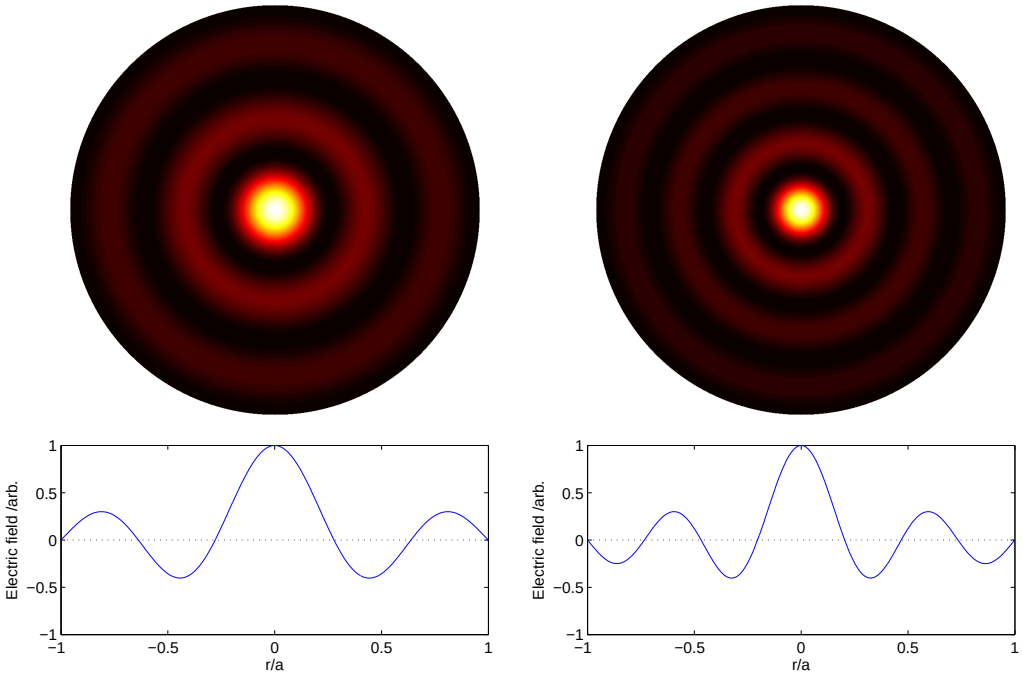

(c) EH_{13} (d) EH_{14}

Figure 2.7: *Intensity distributions (images) and electric field profiles (lines) for the EH_{1m} modes of a capillary.*

by [77]:

$$\beta_{nm} = \Re\left(\gamma\right) = k_0 \left[1 - \frac{1}{2}\left(\frac{u_{nm}\lambda}{2\pi a}\right)^2\right] \tag{2.16a}$$

$$\alpha_{nm} = \Im\left(\gamma\right) = \left(\frac{u_{nm}}{2\pi}\right)^2 \frac{\lambda^2}{a^3}\left(\frac{\frac{1}{2}\left(\nu^2+1\right)}{\sqrt{\nu^2-1}}\right). \tag{2.16b}$$

The propagation constants β_{nm}, attenuation constants α_{nm} and transmission through a typical capillary length are shown in figure 2.8. We see that β_{nm} is slightly less than k_0, and thus each mode of the capillary propagates with a phase velocity slightly greater than that in vacuum, with this difference increasing with the value of m. The guiding process in the capillary is a series of grazing incidence reflections from the capillary walls, and so, since reflection from a surface with higher reftracive index is not perfect, the modes are lossy. From equation (2.16b) it is seen that α is proportional to u_{nm}^2 , so the propagation loss also increases with mode order. The lowest loss, linearly polarised mode of a hollow capillary waveguide is therefore the EH_{11} mode. In fact, for materials with refractive index $\nu < 2.02$, the EH_{11} mode has the lowest loss of all — arbitrarily polarised — capillary modes [77].

2.3.1 Degenerate combinations of modes

From the definition of the propagation constants in equations 2.16, it is found that the only dependence of γ_{nm} on n and m is through the factor u_{nm}. From [80] we have the identity

$$J_{-n}(x) = (-1)^n J_n(x). \tag{2.17}$$

Therefore, J_n and J_{-n} must have the same roots. As u_{nm} is the mth root of the equation $J_{n-1}(u_{nm}) = 0$, it follows that that $u_{-|n|,m} = u_{|n|+2,m}$. Therefore, the modes $\mathrm{EH}_{-|n|,m}$ and $\mathrm{EH}_{|n|+2,m}$ are degenerate, and can be combined to produce composite modes. If the field components for these modes are added with equal amplitude and

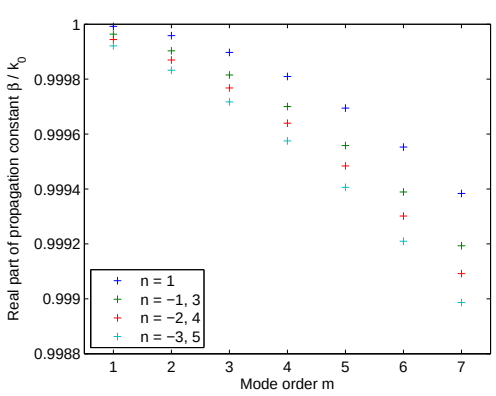

(a) Real part of the propagation constant β_{nm}.

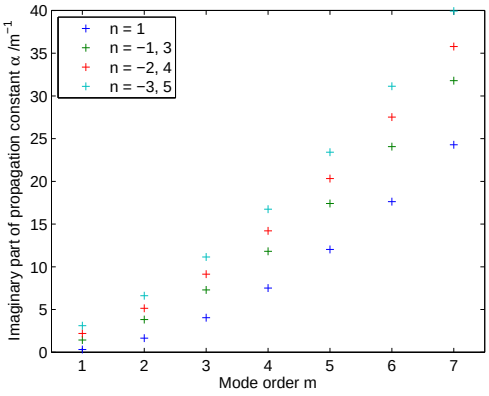

(b) Imaginary part of the propagation constant α_{nm}.

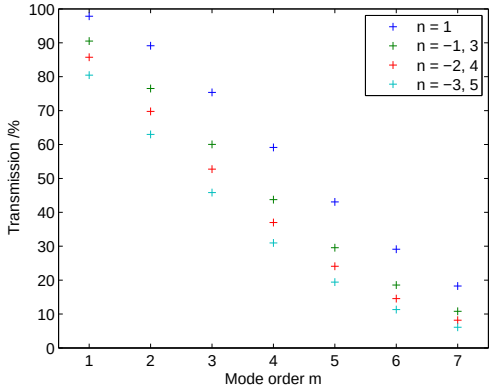

(c) Transmission through a 7 cm length of capillary.

Figure 2.8: *Mode propagation constants and transmissions of the EH_{nm} modes though a* 7 cm *length of* 75 µm *radius glass capillary. In each plot, the radial order m is represented on the x axis, and the azimuthal order n is represented by the line colour. The wavelength of the light is* 780 nm.

zero phase, then we obtain, after conversion into Cartesian coordinates,

$$E_{y,|n|+2,m} = 2J_{n+1}\left(u_{n+2,m}\frac{r}{a}\right)\cos\left(\left[n+1\right]\theta\right) \tag{2.18a}$$

$$E_{x,|n|+2,m} = 0. \tag{2.18b}$$

These modes are linearly polarised (as $E_{x,|n|+2,m} = 0$) and so are of interest here, but the intensity profiles of these composite modes — as opposed to those of the non-composite modes — are not radially symmetric. Sample intensity profiles for some of these modes are shown in figure 2.9. If the relative amplitude of the two modes is varied, then the composite mode is no longer linearly polarised. If the phase of the two modes is changed, then a phase shift of nπ rad for odd integer n causes a rotation of the field profiles by 45° relative to the polarisation of the field. Any phase shift that is not a multiple of π rad causes the composite mode to lose its linear polarisation. The propagation constants for composite modes are, by definition, identical to those for their constituent modes.

These composite modes together with the TE_{0m}, TM_{0m} and EH_{nm} modes form a complete set [77,81]. Here we are interested only in the subset of these modes that are linearly polarised: the composite modes and the EH_{1m} modes.

2.4 Experimental arrangement

Figure 2.10 shows a schematic of the HHG experimental arrangement used in the experiments described in this thesis. As the work reported here is theoretical, the experimental arrangement will not be covered in great detail, but a summary is given below.[4] Additional detailed aspects of the experimental arrangement will be discussed as they become relevant.

The output of a titanium sapphire chirped pulse amplifier (CPA) system is focused with a long focal length ($\sim$ 50 cm) lens through a thin fused silica window into a vacuum chamber held at low pressure (less than 10^{-3} mbar). The laser system is

[4]Further details of the experimental arrangement can be found in refs. [57, 82, 83].

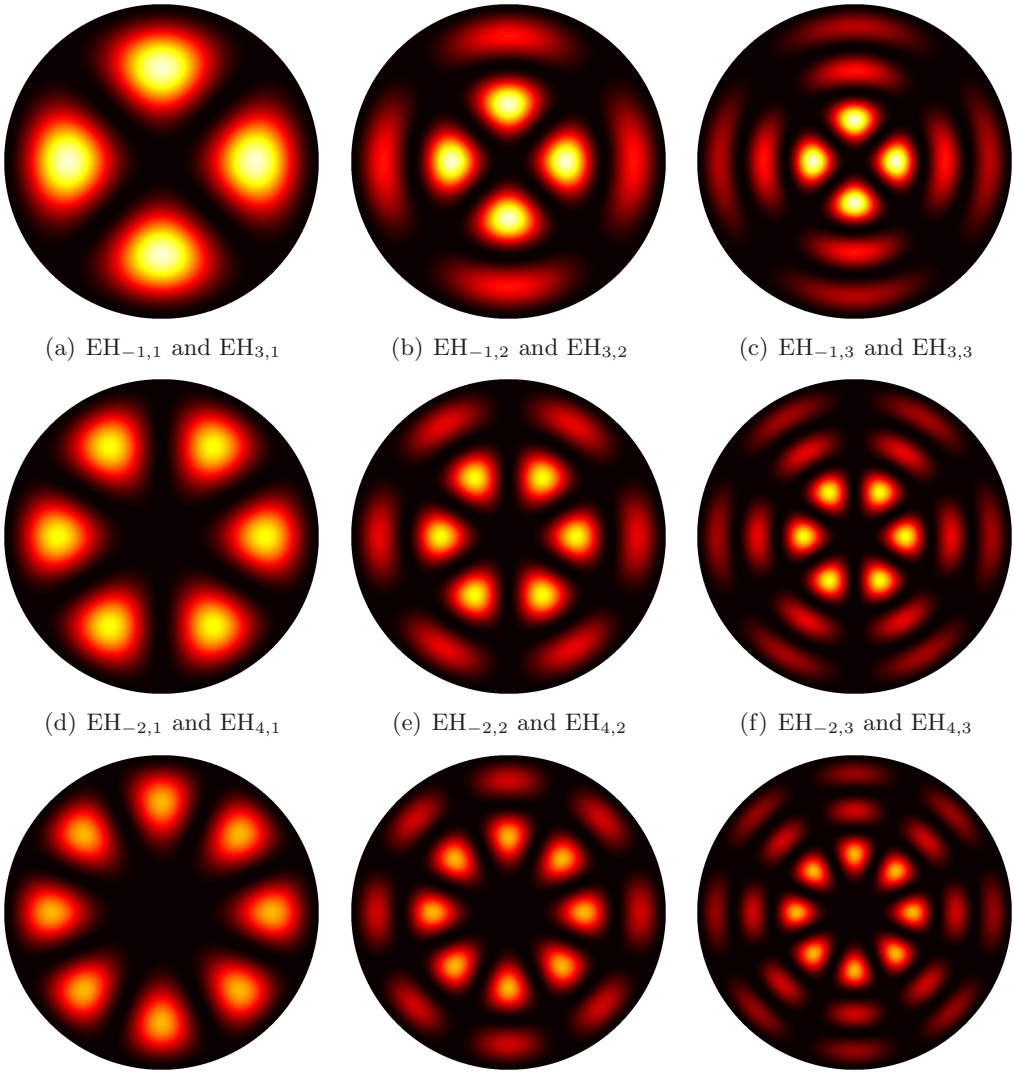

(a) $EH_{-1,1}$ and $EH_{3,1}$ (b) $EH_{-1,2}$ and $EH_{3,2}$ (c) $EH_{-1,3}$ and $EH_{3,3}$

(d) $EH_{-2,1}$ and $EH_{4,1}$ (e) $EH_{-2,2}$ and $EH_{4,2}$ (f) $EH_{-2,3}$ and $EH_{4,3}$

(g) $EH_{-3,1}$ and $EH_{5,1}$ (h) $EH_{-3,2}$ and $EH_{5,2}$ (i) $EH_{-3,3}$ and $EH_{5,3}$

Figure 2.9: *Intensity distributions for composite capillary modes composed of $EH_{-|n|,m}$ and $EH_{|n|+2,m}$ modes.*

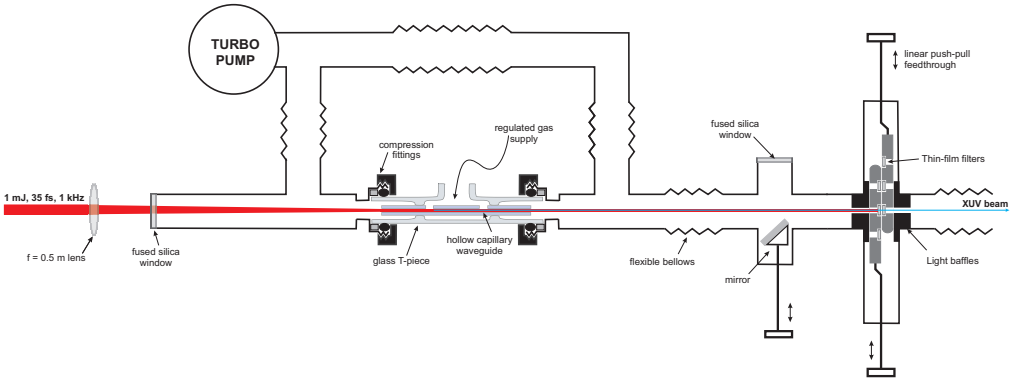

Figure 2.10: *Schematic of a typical experimental arrangement. Figure adapted from [57].*

currently[5] capable of producing a 3 mJ pulse at a 1 kHz repetition rate with a pulse length of 35–40 fs. In the experiments reported here, pulses with an energy of no more than 1 mJ were used. The M^2 parameter of the beam from the CPA system was measured to be ~ 1.8.

A capillary waveguide is placed at the focus of the laser. This capillary is filled with gas as detailed in section 2.5. In the capillary, the laser interacts with the gas and generates high harmonics, and these harmonics are separated from the driving laser with a 200 nm aluminium foil. This foil reflects the fundamental laser while allowing approximately 10 % of the harmonics to pass through. The beam can then propagate to either an Andor CCD camera to record the spatial profile, or an XUV spectrometer to record the spectrum. Alternatively, the fundamental beam can be directed out of the capillary using a turning mirror, for measurement of its properties after propagation through the capillary. This arrangement is discussed further in section 4.1.

2.5 Pressure profile in a gas-filled capillary

The modelling of the gas flow described in this section was performed within this group by Matthew Praeger. Here I describe the results, and

[5]The laser system was upgraded during the course of the project from a 1 mJ to a 3 mJ output.

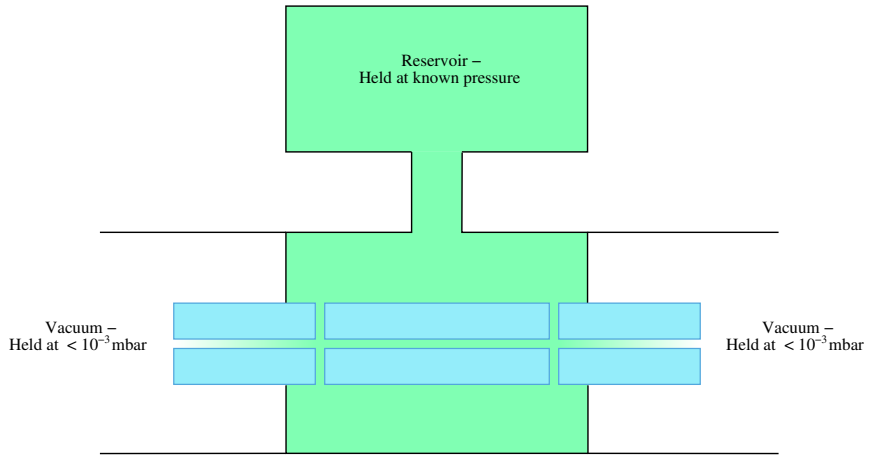

Figure 2.11: *Schematic of the capillary, showing the gas filling method.*

their application to the models I have developed.

The waveguides used in the harmonic generation experiments in this group are thick-walled, fused silica capillaries. These capillaries have holes drilled in the sides, through which gas flows in, and both ends of the capillary are held at a pressure less than 10^{-3} mbar (figure 2.11). Typically the capillaries used have a internal diameter of 150 μm and external diameter of 1.5 mm. The holes in the side vary from $300 - 500$ μm depending upon the method used to drill them. A typical capillary has a length of 7 cm with two holes, 3 cm apart and 2 cm from each end. Capillaries with different lengths and/or with only a single inlet hole have also been investigated.

To model the processes occurring in the capillary, it is necessary to know the pressure profile as a function of position. As shown in figure 2.11 there is a reservoir of gas held at a known pressure on the outside of the holes. In our group, Matthew Praeger created a computational fluid dynamic model of the capillary given the

conditions described. A sample output is shown in figure 2.12. The general features of this model are a constant pressure region in the centre of the capillary at the pressure of the reservoir, a very sharp change in pressure over the width of the holes and then a linear pressure gradient falling to the background pressure at the ends of the capillary. Here the sharp change over the 500 μm hole diameter is modelled as a step change. This approximation will not have a large effect on any of the models presented in this thesis, as the phasematching model is valid only for the constant pressure region and the propagation model is sensitive only to the pressure at a given point, and not the rate of change of pressure. The error in the pressure values over the hole regions will be negligible. Given this information, the entire pressure profile can be calculated for any two-hole capillary for which the dimensions are known, with only the knowledge of a single parameter, the size of the step change in pressure at the holes. If the size of this step is plotted as a function of nominal pressure, it is seen that the relationship is linear with a gradient of 0.205. It is then possible to calculate the pressure profile for any given two-hole capillary for a known reservoir pressure.

2.6 Calculation of gas refractive indices

In the previous section, the pressure in the capillary was determined as a function of position. In order to determine how the presence of that gas affects the propagation of light in the capillary, it is necessary to know the refractive index of all the gases that are present in the capillary during any experiment. In the case of high harmonic generation, there are two very widely spaced wavelength regimes in which the refractive index must be determined: the near infrared, at around 800 nm; and the XUV at 10 - 40 nm. These two regions must be treated separately, so we will consider each in turn.

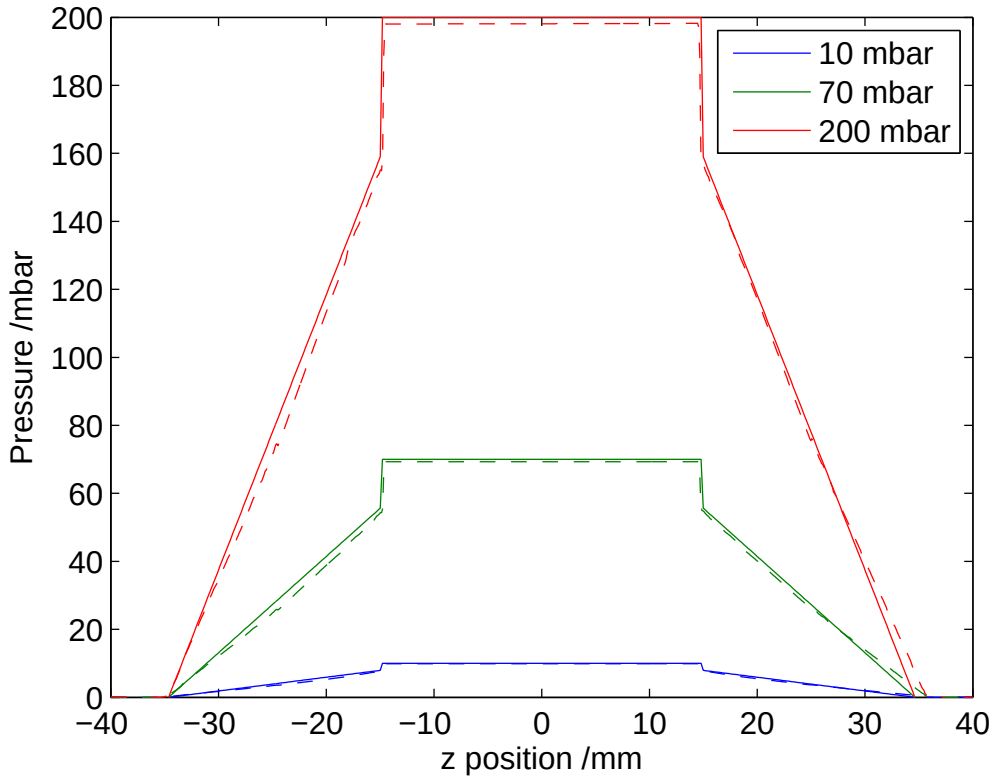

Figure 2.12: *Pressure as a function of position in a typical two-hole capillary for a reservoir pressure of* 10 , 70 *and* 200 mbar. *Dotted line: output of CFD model. Solid line: fits used to determine pressure profiles for use in modelling of processes within the capillary.*

Gas	Reference	Model	Constants
Helium	[84]	Eqn 2.19	$A = 6.9270 \times 10^{-05}$, $B = 224000$ $C = 5.9400 \times 10^{10}$, $D = 1.7200 \times 10^{16}$ $E = 0$, $F = 0$
Neon			$A = 1.3350 \times 10^{-04}$, $B = 224000$ $C = 8.0900 \times 10^{10}$, $D = 3.5600 \times 10^{16}$ $E = 0$, $F = 0$
Argon			$A = 5.5470 \times 10^{-04}$, $B = 515000$ $C = 4.1900 \times 10^{11}$, $D = 4.0900 \times 10^{17}$ $E = 4.3200 \times 10^{23}$, $F = 0$
Nitrogen	[85]	Eqn 2.20	$A = 5109702.9$, $B = 183.69459$, $C = 212.949$, $D = 7.74396$
Nitrous Oxide	[86]	Eqn 2.21	$A = 5.6685 \times 10^{27}$, $B = 11416 \times 10^{27}$
Carbon Dioxide	[87]	Eqn 2.23	$A = 154.489$, $B = 0.0584738$ $C = 8309192.7$, $D = 210.92417$ $E = 287641.90$, $F = 60.122959$

Table 2.1: *Sources and parameters used to calculate the refractive index of various gases in the near infrared spectral region.*

2.6.1 Refractive indices in the near infrared

The refractive indices of various gases have been measured in the visible and near infrared regions and various models are presented in the literature. Table 2.1 shows a summary of the models used, and the source of data, for each of the gases used in the experiment. All these models are semi-empirical fits to experimental data. As such, each of the references quoted use slightly different equations that the authors see as best fitting their data. These data give only the real part of the refractive index. For the purposes of this work, the imaginary part of the refractive index — and therefore absorption of the laser by the gas — is assumed to be zero.

For noble gases, the refractive index model used is that of Dalgarno and Kingston [84],

$$n^2 = 1 + A\left(1 + \frac{B}{\lambda(\text{Å})^2} + \frac{C}{\lambda(\text{Å})^4} + \frac{D}{\lambda(\text{Å})^6} + \frac{E}{\lambda(\text{Å})^8} + \frac{F}{\lambda(\text{Å})^{10}}\right), \tag{2.19}$$

where $\lambda(\text{Å})$ is the wavelength in angstroms. The measurements were taken at room temperature and pressure (RTP), and so conversion to room temperature is not

necessary.

For nitrogen, the model of Peck and Khanna [85] is used,

$$n = 1 + 10^{-8}\left(\frac{A}{B-\sigma^2} + \frac{C}{D+\sigma^2}\right), \qquad \sigma = \frac{1}{\lambda(\mu\mathrm{m})}, \tag{2.20}$$

where $\lambda(\mu\mathrm{m})$ is the wavelength in microns. The measurements were taken at 288 K, and so must be converted to RTP as detailed below.

For nitrous oxide, the model was taken from Cuthbertson and Cuthbertson [86]

$$n = 1 + \frac{A}{B-f^2}, \qquad f = \frac{c}{\lambda}. \tag{2.21}$$

Here the refractive index is given at 273 K and 1 bar, but at the number density of hydrogen gas. Thus a correction factor of

$$\kappa = \frac{M_{\mathrm{N_2O}}}{M_{\mathrm{H_2}}}\frac{\rho_{\mathrm{H_2}}}{\rho_{\mathrm{N_2O}}} = \frac{44.02}{2.00} \times \frac{0.089489}{1.997} = 0.9903 \tag{2.22}$$

is required to give a real refractive index for nitrous oxide at 273 K and 1 bar. Subsequent modification for room temperature and experimental pressures is required.

For carbon dioxide, the model is taken from Ciddor [87]

$$n = 1 + 10^{-8}\left(\frac{A}{B-\sigma^2} + \frac{C}{D-\sigma^2} + \frac{E}{F-\sigma^2}\right), \qquad \sigma = \frac{1}{\lambda(\mu\mathrm{m})}. \tag{2.23}$$

As with Cuthbertson and Cuthbertson, these values are for a refractive index at 273 K and 1 bar.

Conversion of index values to required temperature and pressure

To convert refractive index from one temperature and pressure to another, two assumptions are made. The first is that all the gases used behave as ideal gases, which is a good approximation for the monatomic and small molecular gases at the low pressures used here [88]. The second is that $\delta = \Re(n) - 1$ and $\alpha = \Im(n)$ are proportional to the number density of atoms present [87]. These two assumptions

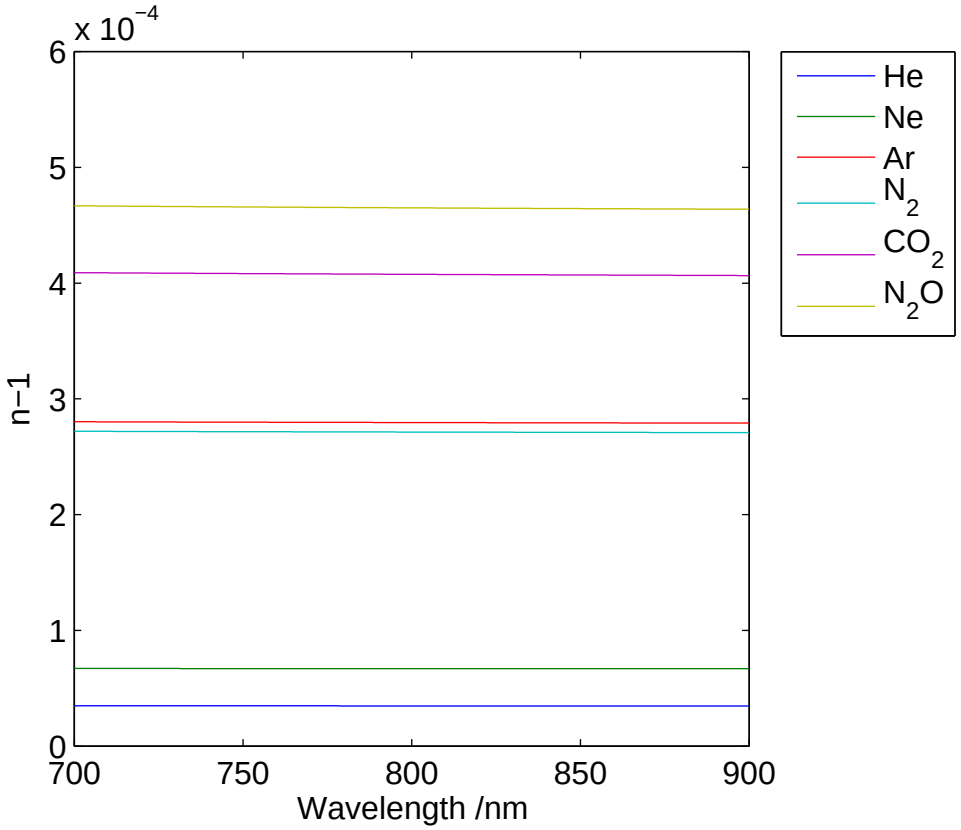

Figure 2.13: *Refractive index of various gases as a function of wavelength in the near infrared region.*

give the following expressions:

$$n = 1 + (n_0 - 1)\,\frac{T_0}{T} \tag{2.24a}$$

$$n = 1 + (n_0 - 1)\,\frac{P}{P_0}, \tag{2.24b}$$

where n is the refractive index at the required temperature T or pressure P and n_0 is the refractive index at some reference temperature T_0 or pressure P_0.

Figure 2.13 shows the refractive index of each of the gases used over a wavelength range of 700 - 900 nm at room temperature and pressure. For all the gases the change in refractive index over the range plotted is small. In all cases δ is small and positive, and generally increases with number of electrons in the atom or molecule.

2.6.2 Refractive indices in the XUV

In contrast to the situation for the infrared region described above, the refractive index of substances in the XUV region is far from well known. There are two tabulations [89,90] of the atomic scattering factors over wide energy ranges, but both suffer from large inaccuracies in the wavelength/energy range of interest (20 - 60 eV, 20 - 62 nm). Henke *et al.* [90] provide the atomic scattering factors, f_1 and f_2, from which the refractive index can be obtained, as calculated from experimentally measured photoabsorption data with interpolations over atomic number and energy where data is not available. The photoabsorption data allow direct calculation of f_2, while f_1 is calculated from modified Kramers-Kronig relations. In addition, although [90] provides values of f_2 from 10 - 30 000 eV, the values for f_1 are limited to energies above 40 eV. Chantler *et al.* [89], on the other hand, provide f_1 and f_2 obtained from theoretical calculations for energies down to 10 eV, but estimate uncertainties for energies below 200 eV of 50–100 %. The two data sets are compared below, after the method of converting atomic scattering factors to refractive index has been discussed

Conversion of atomic scattering factors to refractive index

Henke *et al.* [90] define the atomic scattering factor $f = f_1 + if_2$ as the factor by which one must multiply the amplitude scattered by a single free electron to yield the total amplitude coherently scattered by a particular atom. Thus,

$$E = -E_0 \frac{r_0}{r} P(\phi) f, \tag{2.25}$$

where E_0 is the incident electric field, r is the distance from the atom to the observation point, $r_0 = e^2/\left(4\pi\epsilon_0 m_e c^2\right)$ is the classical electron radius and $P(\phi)$ is the polarisation factor, which is unity for the case of forward scattering that is of interest here.

For wavelengths that are long compared with the atomic dimensions, atoms in

a material scatter electromagnetic radiation as dipoles, and the scattering can be described by the complex refractive index n. The refractive index is related to the atomic scattering factor by [89, 90]

$$n = 1 - \frac{r_0}{2\pi}\lambda^2 \sum_j n_j f_j, \tag{2.26}$$

where n_j is the number density of atoms of type j and f_j is the atomic scattering factor of the jth atom.

With relation 2.26 we can now investigate the differences between data sets [89] and [90]. Figures 2.14 and 2.15 show the real and imaginary parts of the refractive index, as calculated from each of the two references, for four sample gases. While the overall trends are generally the same, there are significant differences in the structure and scaling of the refractive index components. As neither data set is particularly more accurate than the other, the choice was made to use the data of Chantler *et al.* [89] because the data from Henke *et al.* [90] does not cover the whole region of experimental interest.

Uses of the XUV refractive index

The XUV refractive index data are used in the phasematching calculations described in chapter 3, and in calculating the absorption of generated harmonics in subsequent — non-generating — regions of the experimental arrangement. The same method can also be used to calculate the transmission of various metal filters that are used in the experiment to separate the harmonics from the fundamental light (see section 2.4. Figure 2.16 shows the absorption depths of various gases used for generation as a function of energy. It is seen that even for the most transmissive gases at the relatively low pressure of 50 mbar, the absorption depth is no greater than a few millimetres.

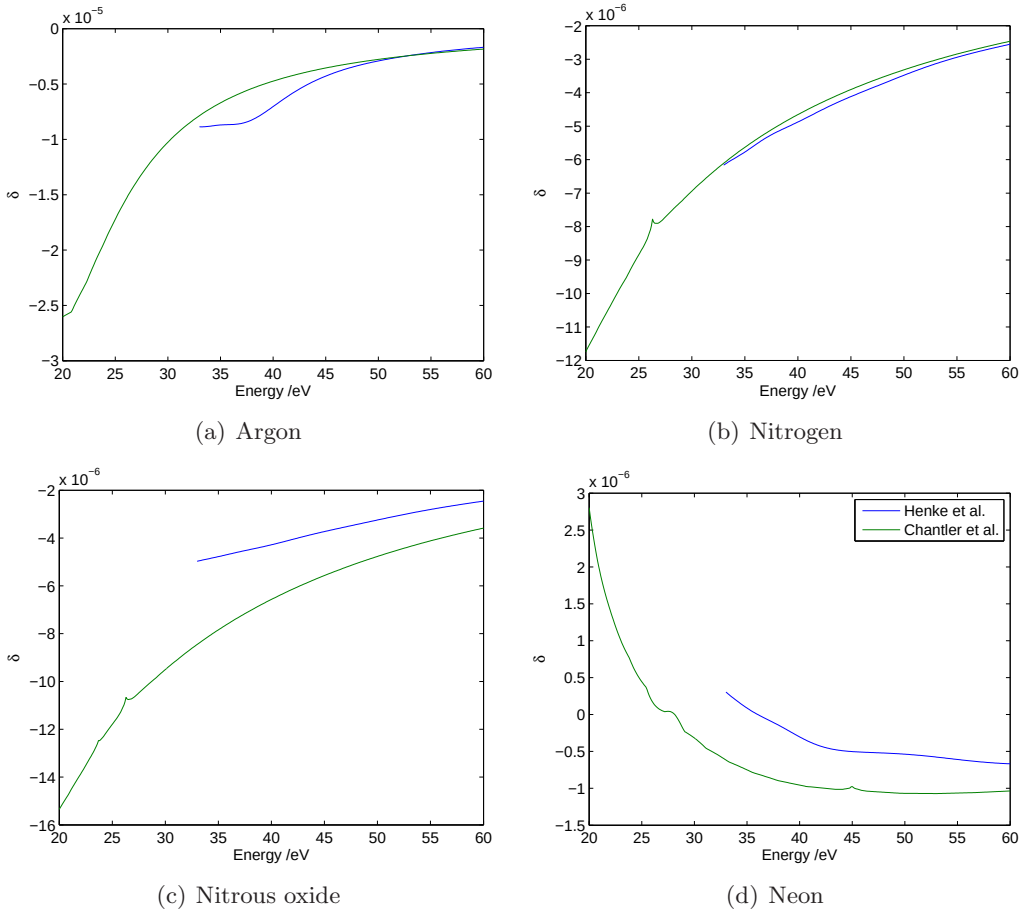

(a) Argon (b) Nitrogen

(c) Nitrous oxide (d) Neon

Figure 2.14: *Real part of the refractive index,* $\delta = \Re(n) - 1$*, as a function of photon energy at* 50 mbar *for (a) argon, (b) nitrogen, (c) nitrous oxide, (d) neon.*

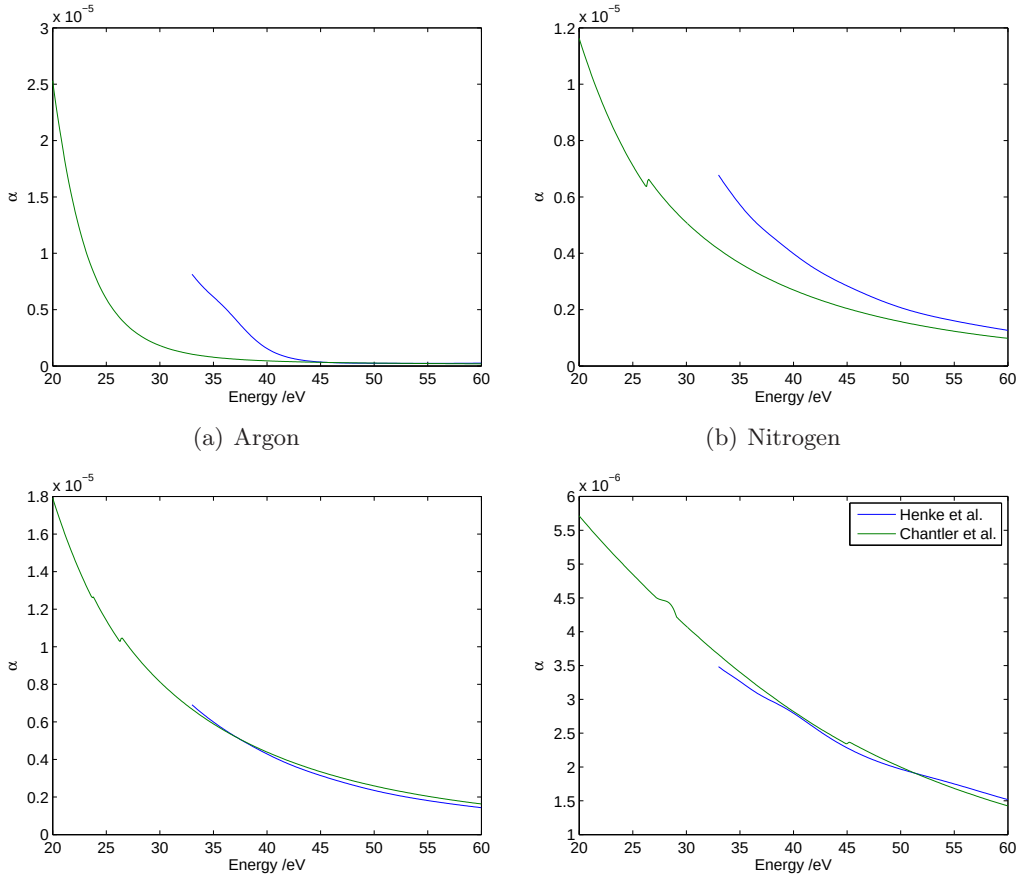

(a) Argon (b) Nitrogen

(c) Nitrous oxide (d) Neon

Figure 2.15: *Imaginary part of the refractive index, $\alpha = \Im(n)$, as a function of photon energy at* 50 mbar *for (a) argon, (b) nitrogen, (c) nitrous oxide, (d) neon.*

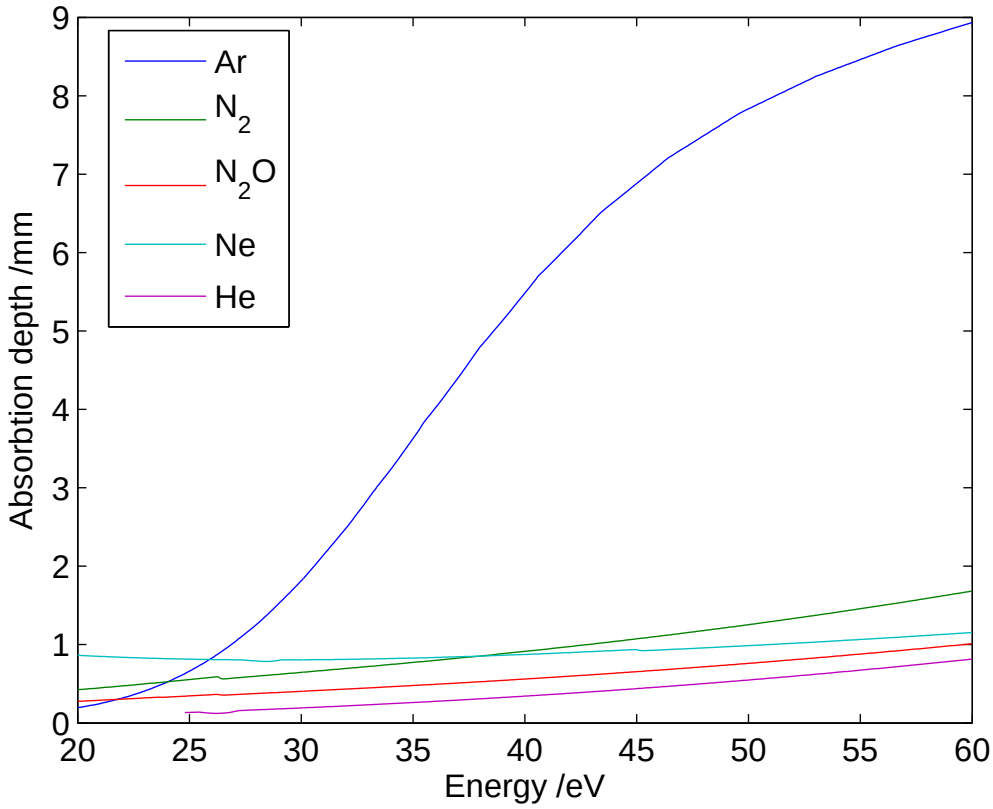

Figure 2.16: *Absorption depths of various gases at* 50 mbar *as a function of photon energy.*

2.7 Summary

A number of pieces of information are needed to develop the models presented in this thesis. This chapter has presented a discussion of the semi-classical model, along with the qualitative predictions of the emitted spectrum and phase that can be obtained from this model. A description is given of the model of ionisation to be used in subsequent chapters, including a discussion of the treatment of BSI and extension of ionisation theory to molecules.

The modes of a hollow capillary have been investigated, and set of linearly polarised modes found. The radial profiles and propagation constants of each mode have been determined. A brief outline of the experimental arrangement is given and a summary of previous work on the modelling, together with the methods used to include this profile in the subsequent models, is presented.

The final part of this chapter presents the equations used to determine refractive indices of gas in the infrared region, and discusses the published values of refractive index in the XUV. The data of Chantler *et al.* [89] is chosen for use here as it spans the experimentally interesting range of energies.

These various pieces of information will be used to develop the models in chapters 3, 4 and 5.

Chapter 3

Development of a spatio-temporal phasematching model

3.1 Phasematching in HHG

As in any optical nonlinear frequency conversion process, the efficiency of harmonic generation is dependent on the degree of phasematching achieved between the generating and generated light.

Consider the simple case (shown in figure 3.1) of second harmonic generation at two locations, P and Q, in a nonlinear medium. In the case of figure 3.1(a), second harmonic radiation generated at Q is in phase with that generated at P; in figure 3.1(b) the two generation events produce light that is π rad out of phase. For the second harmonic light to build up over the length of the medium, the generation from multiple events must interfere constructively. Therefore, in case (a) light will build up over the length of the generation medium, but in case (b) the subsequent events will interfere destructively and efficient build-up will not occur.

This can be expressed physically as an application of the principle of conservation

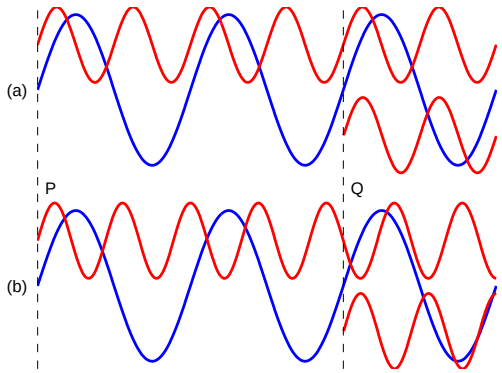

Figure 3.1: *Schematic showing the basic principles of phasematching; a fundamental field (blue line) generates a second harmonic component (red line). (a) Emission at P and Q is in phase; phasematching is achieved. (b) Emission at P and Q is out of phase.*

of momentum. If N photons of momenta $\mathbf{p_i}$ are converted to M photons with momenta $\mathbf{p_j}$, where $i = 1, \ldots, N$, $j = 1, \ldots, M$ then, by conservation of momentum,

$$\sum_{i=1}^{N} \mathbf{p_i} = \sum_{j=1}^{M} \mathbf{p_j} \tag{3.1}$$

and, as photon momentum is given by $\mathbf{p} = \hbar\mathbf{k}$,

$$\sum_{i=1}^{N} \mathbf{k_i} = \sum_{j=1}^{M} \mathbf{k_j}. \tag{3.2}$$

For the case of qth order harmonic generation, q fundamental photons ($N = q$) of wavevector $\mathbf{k_f} = \mathbf{k_i}$, are converted to 1 photon ($M = 1$) with wavevector $\mathbf{k_q} = \mathbf{k_j}$. Therefore the phasematching requirement for general qth order harmonic generation is

$$\mathbf{k_q} = q\mathbf{k_f}. \tag{3.3}$$

Since phasematching is generally non-perfect, it is useful to have a measure of how close to perfectly phasematched a particular system is. The measure normally used is the phase mismatch $\mathbf{\Delta k}$ defined as

$$\mathbf{\Delta k} = \mathbf{k_q} - q\mathbf{k_f}. \tag{3.4}$$

For a homogenous non-absorbing medium, the total intensity output from a non-linear medium of length L is proportional to $\mathrm{sinc}^2(\Delta kL/2)$ [93] where $\mathrm{sinc}(x) \equiv \sin(x)/x$.

For the special case of collinear harmonic generation, as considered here, the vector equation (3.4) can be reduced to the scalar form

$$\Delta k = k_q - qk_f. \tag{3.5}$$

This chapter presents a new model of capillary phasematching that extends previous work to take into account the full spatio-temporal nature of the HHG process. Section 3.2 is concerned with the motivation for the study of phasematching in capillary HHG, what it can tell us, and what its limitations are. This is followed by a discussion of the factors affecting HHG phasematching and its application to a static scenario (section 3.3). The development of a time- and space-dependent model of phasematching is then shown in section 3.4. The output from the model is presented in section 3.5, with discussion of interesting features in section 3.6. The conclusions to the chapter are given in section 3.7.

3.2 Motivation

Since the first recorded high harmonic generation experiments [94–97], much work has been done both on optimising the experimental conditions for generation, and on the development of theory for understanding the generation process. Although, as described in section 2.1, many aspects of harmonic generation can be understood using the semi-classical, three-step model, full quantum mechanical modelling of the electron in the laser field provides a more accurate model of the single atom emission process. The first models of this nature [98–106] were developed shortly after the first experiments, and used various methods to predict the harmonic emission from a single atom in a strong laser field. For example, the model of Kulander and Shore [98–100] used a numerical integration of the time-dependent Schrödinger equation

(TDSE) to determine the time-dependent dipole moment of a xenon atom exposed to a high intensity ($\sim 10^{13}$ W cm^{-2}) laser field. The model assumes a single active electron (SAE); that is, only one electron is significantly affected by the laser and all others remain in their ground states. This approximation is widely used in later models [12,107,108]. The envelope of the field used in this case is not the exact laser field, but a simplified profile that consists of a slow ramp (over 5 optical cycles) and a constant amplitude region of about 20 optical cycles. This model only allows for inclusion of very simple propagation effects, based on analytic approximations to the experimental conditions. Despite these approximations, this models, and other similar models, show good qualitative agreement with experimental results. The characteristic spectrum — a sharp drop in intensity over the first few orders, a plateau region and a sharp cutoff at high energy — is seen in the response of a single atom. TDSE models like this have been extended and developed both in atoms [109, 110] and ions [11].

Even these quantum models only account for the emission from a single atom, and to fully understand the response of a real system it is necessary to take into account the summation of these single atom emissions over an ensemble of atoms. The effect of phasematching has been widely studied in focused geometries [64,65,107,111,112]. These studies fall into two categories, those that study only the geometric phase of the laser and intrinsic phase of the harmonics [64,65,112], and those that include the effect of refractive index changes in the medium due to ionisation [12, 107]. Other theoretical work has focused on quasi-phasematching [109, 113–116], or other novel phasematching techniques. For example, it is proposed that subcycle changes in the electric field induced via ionisation could enhance the generation properties [117].

The situation in a guided HHG geometry is significantly different from that in a focused geometry. In a waveguide, the driving laser is confined such that the intensity is nominally constant over the length of the guide and the wavefronts of the laser are flat. This is in contrast to a focused regime where, even with the loose focusing normally employed, the intensity and wavefront curvature of the fundamental vary

with propagation distance. This gives rise to contributions to phasematching from the Gouy phase shift of the fundamental and variation of the intrinsic (single atom) phase with z. In a waveguide geometry, the Gouy phase shift is not present in the generation region. Also, the phase shift between the fundamental and harmonic fields induced by the single atom emission ϕ, is determined by intensity. Therefore, if the intensity of the fundamental is assumed to be constant as a function of z over the generation region,[1] then ϕ, although a function of radius and time, is constant with respect to propagation distance. The collinear contribution to the phase mismatch is given by $\frac{\mathrm{d}\phi}{\mathrm{d}z}$ which here is identically zero.[2] Thus neither the Gouy phase shift nor the dipole phase affect the collinear phase mismatch Δk. In this regime the refractive index effects are the only contributing factors to phasematching and must be accounted for explicitly.

Previous studies of phasematching in capillaries have either included the radial variation of ionisation through radial averaging [118–120], allowing no variation of the phasematching conditions with radius, or have used numerical propagation codes to model the build-up of the harmonic field [109, 113]. Here, the approach of Durfee *et al.* [118] and Naumov *et al.* [120] is used, but the calculations are extended to include the full radial variation of ionisation.

3.3 Phasematching in a constant ionisation fraction

In the case of a capillary waveguide HHG experiment there are several factors affecting the propagation constant which must be balanced in order to achieve phasematching:

- neutral gas dispersion;
- plasma dispersion;
- waveguide dispersion; and
- non-linear refractive index.

[1] This assumption is justified in section 3.4.2.

[2] There is a non-collinear contribution given by $\frac{\mathrm{d}\phi}{\mathrm{d}r}$ which is discussed in section 3.4.2.

Here we follow the approach of [118], though major modifications are made to take into account the full spatio-temporal nature of the HHG process. The propagation constant of light with wavelength λ in the EH_{nm} mode of a capillary waveguide is given by [77]

$$\beta_{nm} = k_0 \left[1 - \frac{1}{2} \left(\frac{u_{nm}\lambda}{2\pi a} \right)^2 \right], \tag{3.6}$$

where $k_0 = \frac{2\pi}{\lambda}$ is the vacuum propagation constant and u_{nm} is the mth zero of the Bessel function J_{n-1}. If the waveguide is filled with a medium of refractive index $n \approx 1$, then the modes of the capillary are not significantly changed and the propagation constant k becomes

$$\begin{aligned} k &= n\beta_{nm} \\ k &= n\left(k_0 - \frac{u_{nm}^2\lambda}{4\pi a^2} \right) \\ k &= (1+\delta)\left(k_0 - \frac{u_{nm}^2\lambda}{4\pi a^2} \right) \\ k &= k_0 + \delta k_0 + \frac{u_{nm}^2\lambda}{4\pi a^2} + \delta\frac{u_{nm}^2\lambda}{4\pi a^2} \\ k &\approx (1+\delta)k_0 - \frac{u_{nm}^2\lambda}{4\pi a^2}, \end{aligned} \tag{3.7}$$

where $\delta = \Re(n) - 1$ and the cross term, $\delta\frac{u_{nm}^2\lambda}{4\pi a^2}$, has been neglected since it is small compared to the other terms.

The refractive index of a partially ionised gas is given by [118]

$$n = 1 + P\left\{ \delta(\lambda) - \frac{\eta N_{\mathrm{atm}} r_e \lambda^2}{2\pi} + n_2 I \right\}, \tag{3.8}$$

where P is the gas pressure in atmospheres, η is the ionisation fraction, N_{atm} is the number density at 1 atmosphere, r_e is the classical electron radius, n_2 is the non-linear refractive index and I is the pulse intensity.

Here the assumption is made that the (complex) refractive index of the ionised gas atoms is approximately the same as the index of the neutral atoms. Given

that the refractive index of gas ions in the XUV region is not well known, some approximate value must be used. In some previous work [118], the approximation that the refractive index of the ions is 1 is used. That is, as soon as an atom is ionised, the atom ceases to have an effect on the light in the capillary, and only the free electron has a contribution to the refractive index. Here the approach of Naumov *et al.* is used, in that ionisation is assumed not to affect the refractive index of the atom. This will introduce slight errors in the calculations as the refractive index of the atom is modified by ionisation. However, the modification will be small compared to the original value, and the refractive index component from the gas is smaller than the component from the free electrons, even at low ionisation fractions.

This gives the propagation constant

$$k \approx \frac{2\pi}{\lambda} + \frac{2\pi P\delta(\lambda)}{\lambda} + n_2 IP - P\eta N_{\text{atm}} r_e \lambda - \frac{u_{11}^2 \lambda}{4\pi a^2}, \tag{3.9}$$

where the terms correspond respectively to vacuum, neutral gas dispersion, nonlinear refractive index, plasma dispersion and waveguide dispersion. Equation 3.5 gives

$$\Delta k = k_q - q k_f \tag{3.10}$$

$$\Delta k = q k_0 \left\{ n(\lambda_q) - n(\lambda_0) \right\} \tag{3.11}$$

$$\Delta k \approx q \frac{u_{11}^2 \lambda_0}{4\pi a^2} + N_e r_e \left(q\lambda_0 - \lambda_q \right) - \frac{2\pi P}{\lambda_q} \left\{ \delta(\lambda_0) - \delta(\lambda_q) \right\}, \tag{3.12}$$

where $N_e = \eta P N_{\text{atm}}$ is the density of electrons. The first term in equation (3.12) corresponds to the guiding of the fundamental; the second term corresponds to the dispersion of the plasma present in the capillary; and the third term corresponds to the dispersion of the neutral and ionised gas atoms. Here the nonlinear refractive index of the gas is neglected, as it is small compared to the other contributions. Taking the nonlinear refractive index of argon as 9.8×10^{-24} m^2 W^{-1} bar^{-1} [121] and a typical intensity of 2×10^{14} W cm^{-2} gives the nonlinear contribution to re-

fractive index at 100 mbar as $\Delta n = 2.0 \times 10^{-6}$. This is just 7 % of the component from the neutral gas atoms δ.

The contribution of waveguiding to the refractive index of the XUV radiation is shown to be negligible in the following way. The equation for the phase mismatch from only the waveguide, including guiding of XUV where the XUV radiation can be in an arbitrary EH_{1m} mode, is

$$\Delta k_{\text{guide}} = q\frac{u_{11}^2\lambda_0}{4\pi a^2} - \frac{u_{1m}^2\lambda_q}{4\pi a^2} \tag{3.13}$$

$$\Delta k_{\text{guide}} = \frac{q\lambda_0}{4\pi a^2}\left(u_{11}^2 - \frac{u_{1m}^2}{q^2}\right). \tag{3.14}$$

For large m, $u_{1m} \approx m\pi$, and hence, the guiding of the XUV is only relevant for

$$m \gtrsim q\frac{u_{11}}{\pi} \tag{3.15}$$

$$m \gtrsim 0.76\,q. \tag{3.16}$$

If the XUV field (as calculated by this model, see section 3.5) for each harmonic is decomposed into capillary modes using the techniques described in section 5.3, it is found that only ~ 1 % of the power is propagating in modes with $m \geq 0.76\,q$.

3.3.1 Constant ionisation fraction results

The most common way of controlling the phasematching of HHG in capillaries is to control the pressure of the gaseous generation medium. This influences both the plasma and neutral gas dispersion terms, and can be used to balance these against the fixed waveguide dispersion. Another very important factor that can be indirectly controlled is the ionisation fraction of the gas. This is determined by the intensity of the fundamental laser pulse used to generate the harmonics.

Using equation (3.12) it is possible to produce plots of the variation of Δk with pressure and ionisation fraction for each harmonic (figure 3.2). From figure 3.2(a) it can be seen that for a given ionisation, the phasematched harmonic order can be

increased by increasing the pressure of the argon. Also, for a fixed pressure, higher ionisation fractions cause phasematching of lower harmonics.

3.4 Time-dependent phasematching

Having obtained an understanding of the relevant factors in static phasematching, this section describes the development of a phasematching model that takes into account the full spatio-temporal nature of the HHG process.

Consideration of the semi-classical model (section 2.1) shows that ionisation is a necessary step in the HHG process. This means that any HHG experiment will have a changing ionisation fraction with time as the driving laser ionises the generation medium. Figure 3.3 shows the typical form of the variation of ionisation fraction with time. Before the pulse arrives, the ionisation fraction is zero; as the intensity increases to the threshold for tunnelling ionisation, the gas starts to ionise, with rapid increases at the (positive and negative) peaks of the electric field and plateaux as the field passes through zero. As the pulse passes, the intensity drops below the ionisation threshold, and no further ionisation occurs. Here the rapidly oscillating carrier field is used for calculation of ionisation rate as has been shown to be appropriate by Uiberacker *et al.* [122].

As the intensity of a laser beam (either a Gaussian beam in a focused geometry or a waveguide mode in a guided geometry) varies with radius, the ionisation fraction is also spatially dependent. In section 3.3 it was found that the phase mismatch between the fundamental and XUV radiation is strongly dependent on ionisation fraction. Therefore, to model the full effect of phasematching in an HHG experiment, it is necessary to calculate the build-up of harmonic radiation as a function of space and time throughout the driving pulse.

This section presents the model I have developed to describe spatio-temporal phasematching in capillary HHG. Section 3.4.1 describes the equations used and section 3.4.2 describes the assumptions that are made in the calculation. The computational framework used to calculate the XUV output is described in section 3.4.3.

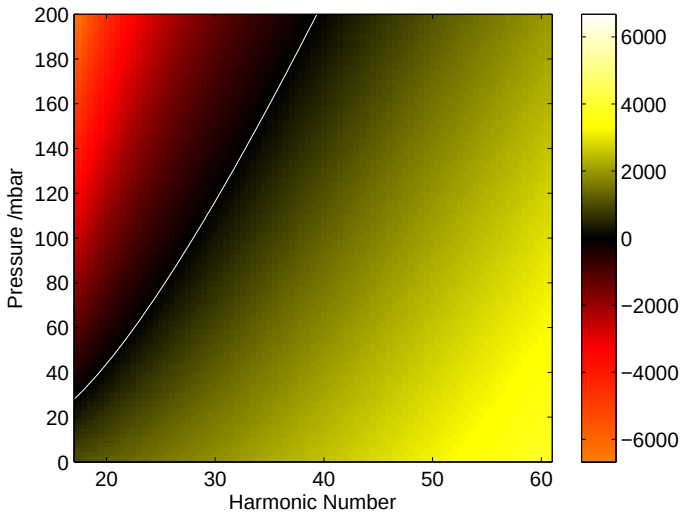

(a)

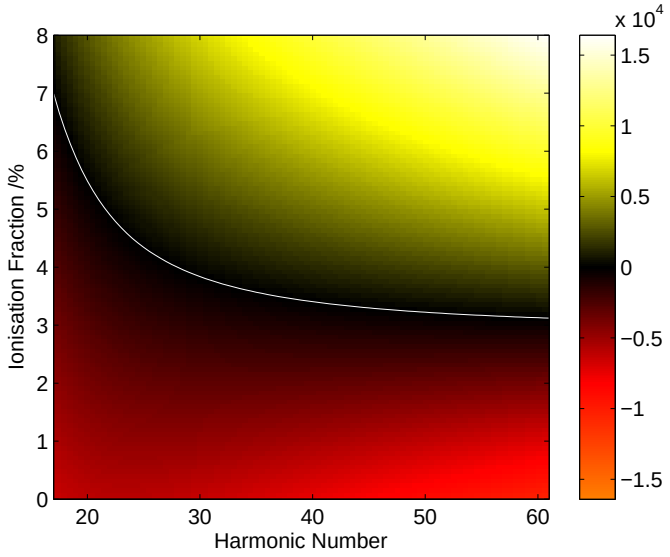

(b)

Figure 3.2: *Phase mismatch, Δk, for pure argon: (a) as a function of pressure and harmonic number for a constant ionisation fraction $\eta = 4\%$; (b) as a function of ionisation fraction and harmonic number at constant pressure $P = 80$ mbar. In both graphs the phasematching curve $\Delta k = 0$ is marked by the white line.*

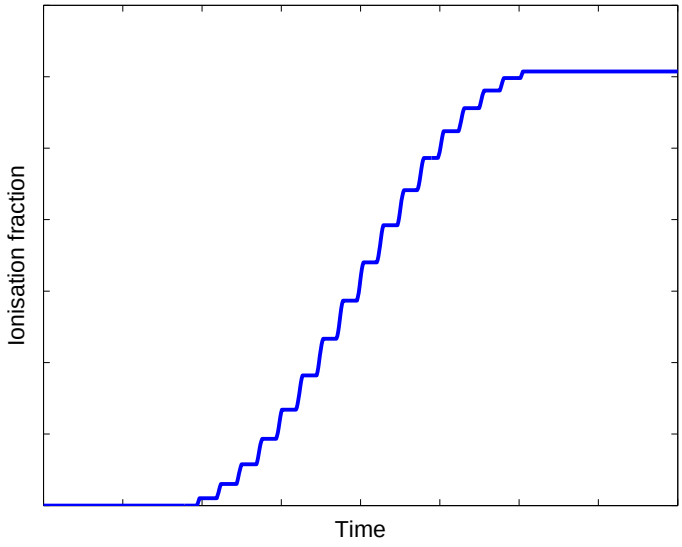

Figure 3.3: *Schematic of variation of ionisation fraction with time, for a given radial position in the capillary. This diagram assumes that tunnelling ionisation is the only significant ionisation mechanism. This implies that the ionisation rate is proportional to field strength rather than intensity, and so shows the characteristic steps in ionisation fraction at twice the optical frequency. The threshold for BSI is assumed not to be reached.*

This is followed by a description of the 3D ionisation calculations (section 3.4.4). Finally, the simple model of single atom response used in determining the build-up of XUV radiation is discussed in section 3.4.5.

3.4.1 Build-up equation

To derive the buildup equation for harmonic generation in an absorbing medium, consider a medium of length L with a generation event occurring at an arbitrary point a distance z from the input face of the medium, and z' from the exit face (figure 3.4). Assuming plane waves, the emitted field at the exit of the medium is from this single generation event is given by

$$E_q(z) \propto S\, e^{-iqk_0 z}\, e^{-i\phi}\, e^{-i(k_q z' - \alpha z')} \tag{3.17}$$

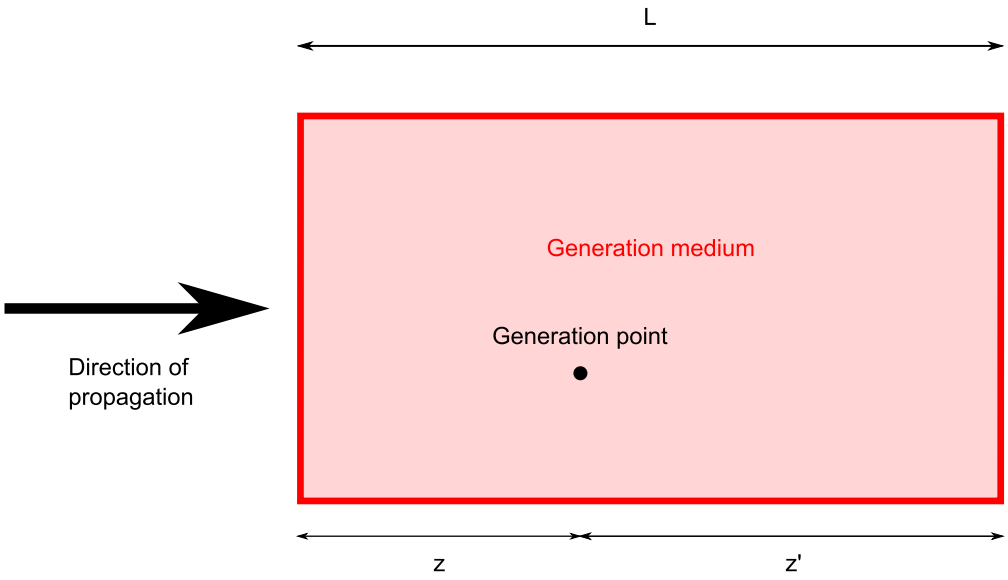

Figure 3.4: *Generation occurs at an arbitrary point in a generation medium. The point is a distance z from the input face of the medium and z' from the output face.*

Where the first exponential represents the phase shift from the propagating q photons of the fundamental (with wavenumber k_0) from the entrance to the generation point (the absorption of the fundamental is assumed to be zero); the second represents a arbitrary phaseshift ϕ resulting from the generation process; and the third represents the phaseshift and absorption from propagating the harmonic from the generation point to the exit of the medium with propagation constant k_q and field absorption coefficient $\alpha = \omega\Im(n)/c$. The factor S is the nonlinear source term. For conventional second harmonic generation this would be $\chi^{(2)}\,|E|^2$.

The factor $e^{-i\phi}$ is a constant and can be included in the proportionality. Since $z' = L - z$,

$$\begin{aligned} E_q(z) &\propto S\, e^{-iqk_0 z}\, e^{-i(k_q L - k_q z)}\, e^{\alpha L}\, e^{-\alpha z} \\ &\propto S\, e^{-i(qk_0 - k_q)z}\, e^{-ik_q L}\, e^{\alpha L}\, e^{-\alpha z}. \end{aligned} \tag{3.18}$$

Again the constant factor $e^{-ik_q L}$ can be dropped. Remembering the definition $\Delta k =$

$k_q - qk_0$ (equation (3.12))

$$E_q(z) \propto S\, e^{i\Delta k z}\, e^{-\alpha z}\, e^{\alpha L}. \tag{3.19}$$

To obtain the total output from the medium $E_q(z)$ must be integrated over the length of the medium.

$$\begin{aligned} E_{\text{out}} &= \int_0^L E_q(z)\,\mathrm{d}z \\ &\propto S\, e^{\alpha L} \int_0^L e^{i(\Delta k + i\alpha)z}\,\mathrm{d}z \\ &\propto \frac{S\, e^{\alpha L}}{i(\Delta k + i\alpha)} \left[e^{i(\Delta k + i\alpha)L} - 1\right] \\ E_{\text{out}} &\propto \frac{S}{i(\Delta k + i\alpha)} \left[\cos(\Delta k L) + i\sin(\Delta k L) - e^{-\alpha L}\right] \end{aligned} \tag{3.20}$$

We then convert from output field strength to intensity and find (as given in [118])

$$I = |E_{\text{out}}|^2 = E_{\text{out}} E_{\text{out}}^* \tag{3.21}$$

$$I \propto |S|^2 \left(\frac{1 + e^{-2\alpha L} - 2e^{-\alpha L}\cos(\Delta k\, L)}{\alpha^2 + \Delta k^2}\right) \tag{3.22}$$

The important physical result of this model is that the harmonic signal strength is dominated by the shorter of the coherence length ($1/\Delta k$) and the absorption length ($1/2\alpha$). This leads to the (physically reasonable) conclusion that in order to achieve good harmonic output, it is important to ensure that a) the harmonics are not strongly absorbed by the medium and b) the phasematching requirements are met in order to allow build-up of the harmonic signal over a significant length of the capillary. It can also be seen that if absorption is neglected, $\alpha = 0$, then equation 3.22 reduces to the familiar $\mathrm{sinc}^2(\Delta k \frac{L}{2})$ dependence.

The nonlinear source term used here is $\mathrm{d}N(r,t)$, the number of atoms ionised by the driving laser at a given time and radius. In conventional low order harmonic generation, the normal form of this term is I^p where p is the order of the harmonic

process. This is because the intensity of the harmonic produced is proportional to the pth power of the intensity of the input field. Here this relationship does not hold, as the harmonic generation process can no longer be treated as a perturbative process. Here, dN is used because the number of XUV photons produced is proportional to the number of atoms ionised, provided that the probability of recombination is constant for any energy, and that all photon energies are equally likely to be emitted at any given time. Although these assumptions are not necessarily true within a single optical cycle, these values average out over a whole cycle. Therefore, these approximations are valid if, as in the regime studied here, we have generation over multiple cycles of the driving pulse.

The intensity build-up, given a phase mismatch $\Delta k(r,t,q)$ and absorption in the generation medium, is therefore modelled by

$$I(r,t,q) \propto \mathrm{d}N(r,t)\left(\frac{1+e^{-2\alpha L}-2e^{-\alpha L}\cos\left(\Delta k\, L\right)}{\alpha^2+\Delta k^2}\right). \tag{3.23}$$

Equation 3.23 cannot be used to obtain quantitative predictions of XUV intensity; it can only be used to predict relative intensities. The most significant reason for this is that the dipole oscillator strength of each individual emitter is not calculated in this model. This strength can be found by solving the time-dependent Schrödinger equation for the atomic system in the laser field (as performed in, for example, [109, 110]), but this type of modelling is not undertaken here. Also, in the derivation of equation (3.23), several constant factors have been dropped because the equation is only valid to within a constant of proportionality.

The build-up equation (3.23) accounts for only the efficiency that a generated harmonic is emitted from the generation medium and neglects the electric field response from a single atom. It cannot, therefore, produce the harmonic structure seen in the experimental results presented below. This harmonic structure comes from the temporal modulation of emission from a single atom, and is therefore not included in this phasematching model. For this reason, the phasematching model only produces an envelope (spatial, spectral and temporal) under which the harmonic

structure should appear and consequently makes no distinction between even and odd harmonics.

3.4.2 Assumptions

As explained is section 3.4.1, the maximum length over which harmonic radiation can build up is the shorter of the coherence length and the absorption depth of the XUV radiation. In the case studied here, the absorption depth is at most of the order of a few millimetres, as shown in section 2.6. This short build-up length allows us to simplify considerably the calculation that needs to be done to model phasematching in a capillary. The short build-up length allows us to assume that the pulse does not change significantly in peak intensity or temporal profile over the build-up region. As discussed in chapter 5, any changes to the pulse profile due to propagation are small in the current experimental regime. If this is so, then the change over the build-up length of a few millimetres (which is much less than the capillary length) will be negligible.

To determine the refractive index of the fundamental and XUV beams, it is necessary to know the ionisation fraction in the capillary. Over a long length of capillary, this ionisation fraction must be averaged over the effective area of the capillary mode. However, as the build-up length is much shorter than the Rayleigh length, z_0, for the fundamental, the ionisation fraction used to determine the refractive index of the fundamental and XUV beams is an instantaneous, local ionisation fraction.

It is also assumed that the wavefronts of the generated XUV radiation are flat, i.e. there is no dependence of XUV phase on fundamental intensity. This is not strictly true, as the phase is known to have an intensity dependence, but this approximation is shown to be valid for the short trajectories (see section 2.1). For the long trajectories, the phase does vary significantly over the radius of the capillary, but because of this the XUV beam generated is highly divergent and so will be much less intense in any experimental measurement. Propagating the XUV beam into the

far field (see section 4.4 for details of these calculations), it is predicted that the XUV radiation generated from the long trajectories will be between 10 and 20 times less intense than that generated by the short trajectories. Also, a beam with highly curved wavefronts will not phasematch well with the fundamental, which, as it is in a capillary mode, has flat wavefronts by definition.

For this assumption to hold, it is necessary that the XUV beam does not diverge significantly over the build-up length. This can be justified by applying the angular spectrum method to the predicted intensities and phases (see section 4.4) which gives a "Rayleigh Range" — defined as the point where $W = \sqrt{2}\,W_0$ and W is twice the second moment beam width [123] — of 10 mm, which is longer than the build-up lengths considered here.

Since the single atom response is not considered in this model, the relative contributions of the two trajectories are not included in this model. It is simply assumed that the long trajectories do not contribute to generation.

The model presented here only takes account of collinear phasematching processes. This is reasonable since the only radial contribution to the harmonic wavevector comes from the radial component of the atomic phase gradient $\frac{\mathrm{d}\phi}{\mathrm{d}r}$. Using the calculations described in section 4.4, this can be calculated to be of the order of 1 % of the vacuum wavevector.

3.4.3 Computational approach

In order to apply the equations presented in section 3.4.1 to the experimental arrangement, the capillary is considered as a series of slices in the axial direction. If the fundamental pulse is assumed not to change in the build-up region (section 3.4.2), then each slice will have an identical response to the driving field. Thus it is only necessary to calculate the response from one slice, and then sum over the number of slices in the capillary. Since the build-up equation 3.23 is only correct to within a proportionality, the sum over identical slices can, in fact, be neglected.

3.4.4 Treatment of ionisation

The electric field profile of the EH_{11} mode of a hollow capillary waveguide of radius a is given by (section 2.3)

$$E(r) = E_0 J_0 \left(\frac{u_{11} r}{a}\right). \tag{3.24}$$

For a Gaussian pulse of intensity full-width at half-maximum (FWHM) τ, the time profile is given by

$$E(t) = E_0 \exp\left(-\frac{t^2}{2\tau_g}\right), \tag{3.25}$$

where $\tau_g = \frac{\tau}{2\sqrt{\ln 2}}$.

So the combined electric field for a Gaussian pulse in the EH_{11} mode at a frequency ω is given by

$$E(r,t) = E_0 \times \exp\left(-\frac{t^2}{2\tau_g}\right) \times J_0 \left(\frac{u_{11} r}{a}\right) \times \cos(\omega t). \tag{3.26}$$

The value of E_0 can be calculated as

$$E_0 = \sqrt{\frac{P_{avg}}{R} \times \frac{7.42}{\pi c \epsilon_0 a^2} \times \frac{1}{1.066\tau}}, \tag{3.27}$$

where P_{avg} is the average power of the laser beam and R is the repetition rate of the laser. Thus P_{avg}/R is the pulse energy.

So, from knowledge of the average power of the laser, which is easily measured, and the length of each pulse, which can be measured experimentally using frequency resolved optical gating (FROG) [124–126] or spectral interferometry for direct electric field reconstruction (SPIDER) [127], the entire electric field profile can be calculated for a capillary of known radius. The assumptions made here are that the pulse is Gaussian in time, and that the entire energy of the pulse is in the EH_{11} capillary mode. These assumptions are reasonable provided coupling is primarily into the EH_{11} mode, and that the pulse is not significantly changed by propagation in the capillary. Chapter 5 discusses the effect of propagation in more detail, but it is shown that at the powers and pressures used in these experiments, the assumption

of a Gaussian pulse primarily in the EH_{11} mode is reasonable. If the exact mode composition and temporal profile were known, perhaps as the output of detailed propagation modelling, these could be included in the calculation relatively easily.

In order to calculate the phase mismatch, and therefore the build-up, it is necessary to know the ionisation fraction in a slice at every radius and time. Using equations 2.10 and 3.26, the ionisation rate $w(r,t)$ can be calculated for all radii and times. The ionisation fraction $\eta(r,t)$ is then given by

$$\eta(r,t) = \int_{-\infty}^{t} w(r,t') \left[1 - \eta(r,t')\right] \mathrm{d}t'. \tag{3.28}$$

These rates and ionisation fractions can be calculated numerically over the whole capillary, though the rapid oscillations in time require a smaller step size than the smoothly varying radial distribution. Output from a sample calculation is shown in figure 3.5.

As described previously (section 3.4) the ionisation fraction at a given radius (in this case the centre of the capillary) starts at zero, and increases with time (figure 3.5(c)). At $t \approx -10$ fs, the intensity becomes high enough to allow tunnelling ionisation and the fraction starts to increase, with the rate of increase high at the (positive and negative) peaks of the electric field and flattening as the field strength passes through zero. For $t \gtrsim 10$ fs the intensity drops below the tunnelling ionisation threshold and no further ionisation occurs. Figure 3.5(b) shows the variation of ionisation fraction with radius for a fixed time $t = 0$ fs. The ionisation fraction is high at the centre of the capillary, where the intensity is high, and drops off smoothly towards the edges. No ionisation occurs for $r \gtrsim 25$ μm as the intensity here is never high enough to cause ionisation. If these two effects are combined, a complete map of ionisation for all radii and times is built up as shown in figure 3.5(a).

The ionisation fraction $\eta(r,t)$ can then be used to calculate the phase mismatch $\Delta k(r,t,q)$ (equation (3.12)) which in turn is used to calculate the harmonic intensity build-up $I(r,t,q)$ from equation (3.23).

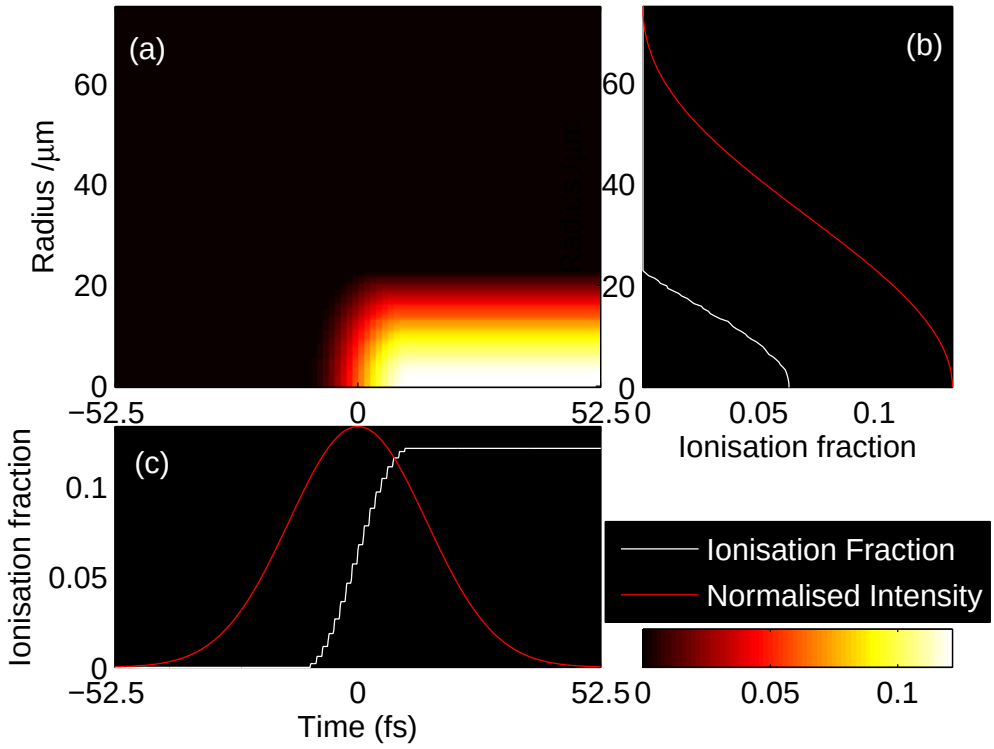

Figure 3.5: *Ionisation fractions for a* 339 mW *average power,* 1 kHz *repetition rate,* 35 fs *laser pulse, with centre wavelength* 780 nm*. These inputs give a peak intensity of* 1.91×10^{14} W cm^{-2} *and a peak electric field of* 3.79×10^{10} V m^{-1}*. The gas is pure argon at* 50 mbar*. a) Ionisation fraction as a function of radius and time. Colour represents the fraction of ionisation in the capillary as indicated by the colour bar. b) Ionisation fraction as a function of radius for time* $t = 0$*, the peak of the pulse. c) Ionisation fraction as a function of time for* $r = 0$*, the centre of the capillary*

3.4.5 Single atom response and the semi-classical cutoff

Equations (3.23) and (3.12) allow, in principle, any harmonic to be phasematched and contribute to the output XUV field. Clearly this is not physical as the driving laser can only transfer a finite amount of energy to the free space electron, and therefore to each generated XUV photon. Here we use the simple cutoff equation

$$E_c = I_p + 3.17\,U_p, \tag{3.29}$$

where E_c is the greatest XUV photon energy that can be generated, I_p is the ionisation potential of the atom and U_p is the pondermotive potential.

This can be derived from the semi-classical model (section 2.1) but has also been shown to be valid in the quantum picture [9, 12]. To include this physical effect in the model, the cutoff energy E_c is calculated for each radius and time, and any emission at that radius and time with a harmonic energy $E_q > E_c$ is set to zero.

This cutoff is the only inclusion of single atom effects in this model. Here the single atom emission is considered to be constant for any energy up to E_c, and zero for any energy greater than E_c (figure 3.6). Single atom predictions (for example, [9, 11, 128]) have shown that this is a good approximation, though obviously it neglects some of the more complex single atom effects.

3.5 Model output

Phasematching surfaces

If we take equation (3.12) and apply it to the ionisation profile calculated from equation (3.28) we obtain a map of the phase mismatch as a function of radius, time and harmonic number. We are interested in the region in which $\Delta k \approx 0\ \mathrm{m}^{-1}$, as this is where the harmonic emission will build up efficiently. It is also interesting to examine how rapidly Δk varies around the zero point to understand the size of the space-time region over which significant build-up can occur. Equation 3.23 implies

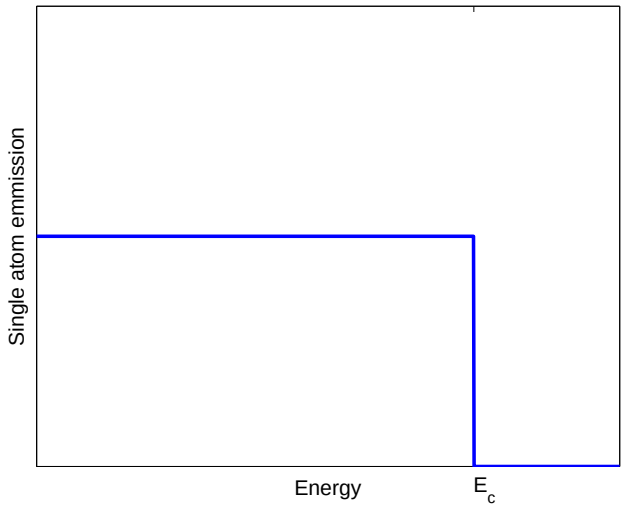

Figure 3.6: *Single atom emission strength as a function of energy, as used in the phasematching model.*

that the length over which XUV generation can build up efficiently is limited to the coherence length $1/\Delta k$. Thus if $\Delta k = 1000$ m^{-1}, then the build-up length is limited to 1 mm.

In figure 3.7 the surfaces in space, time and harmonic for which $\Delta k = 0$, -1000 and 1000 m^{-1} are shown. This shows the overall shape and trends of the evolution of the phasematching conditions. Figure 3.8 shows various slices through these surfaces to allow numerical values to be more easily extracted. At times earlier than -6 fs, no harmonic is phasematched at any radius, as the ionisation fraction is too low. At about -6 fs sufficient ionisation has occurred to phasematch the higher harmonics at the centre of the capillary.[3] As time progresses, phasematching at the centre of the capillary then shifts quickly (less than 10 fs) to low harmonics and then the ionisation fraction becomes too high to phasematch any harmonic and the centre of the capillary ceases to generate efficiently. At the same time, the ionisation fraction increase in the centre pushes the radius at which each harmonic is phasematched towards the edge of the capillary. At times later than 10 fs the pulse intensity

[3]The higher harmonics will not necessarily be generated, as described in section 3.4.5.

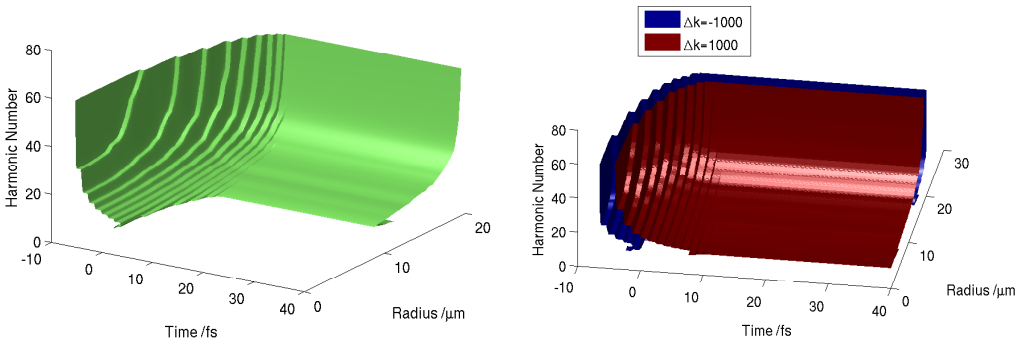

(a) (b)

Figure 3.7: *Phasematching surfaces for the same conditions as figure 3.5. (a) Surface for which* $\Delta k = 0$ m^{-1}*. (b) Region in which* $|\Delta k| < 1000$ m^{-1} *i.e. the coherence length is greater than* 1 mm*.*

has dropped sufficiently that no further ionisation occurs, and the phasematching conditions stop evolving.

Figure 3.7(b), together with the colour scales in figure 3.8, show that the gradient of the phase mismatch is high as it passes through 0 m^{-1}. On axis, at $r = 0$, the time over which the coherence length is greater than 1 mm is only about 5 fs, or about 2 optical cycles. This affects the number of XUV pulses in the pulse train, and therefore the bandwidth of the emitted harmonics. This effect is discussed further in section 4.5.4.

One further point to note is that if figure 3.8(b) is compared to figure 3.5, it can be seen that each line of constant Δk, for a particular harmonic, is a line of constant ionisation fraction. This can be deduced from equation (3.12) as the only dependence of Δk on r and t comes from the spatio-temporally varying ionisation fraction $\eta(r, t)$.

Complete 3-dimensional output

Using the phase mismatch, as calculated above, and equation (3.23), the XUV intensity is calculated as a function of space, time and harmonic number (shown in figure 3.9). Comparing figures 3.7(a) and 3.9 we see that, as expected, intensity is

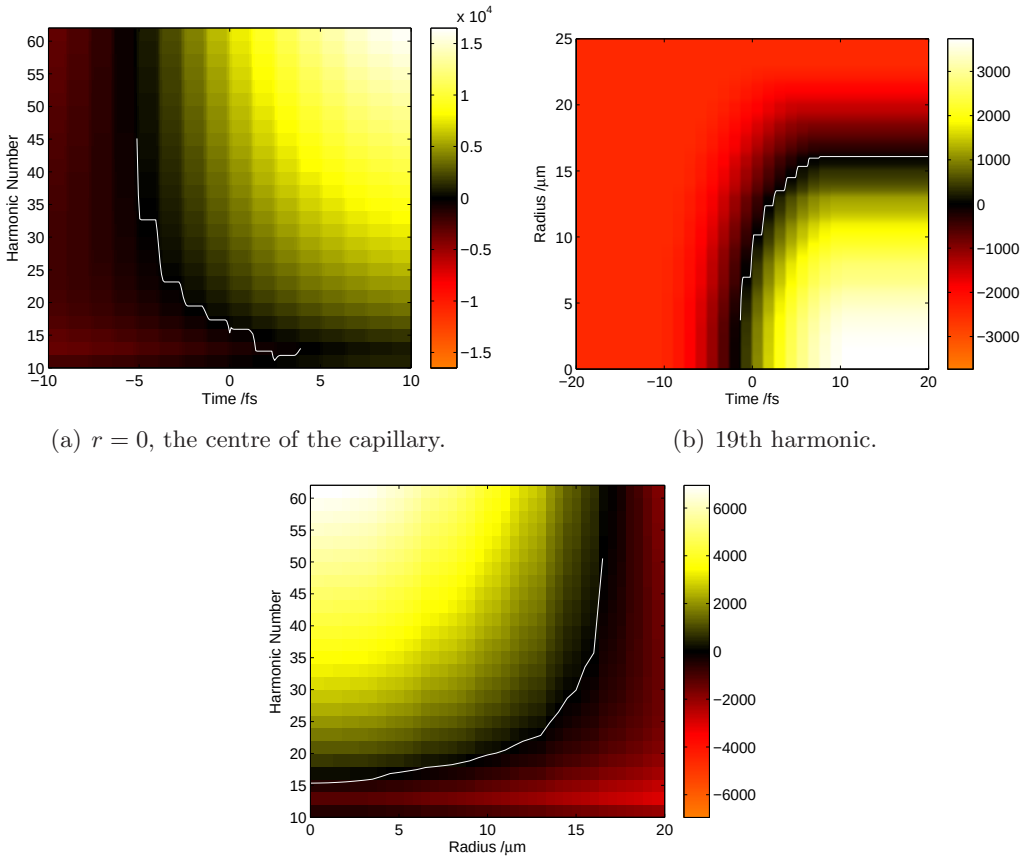

(a) $r = 0$, the centre of the capillary.

(b) 19th harmonic.

(c) $t = 0$, the peak of the pulse.

Figure 3.8: *Phase mismatch Δk for three slices through the pulse. Colour shows the value of Δk in m^{-1}, the white line shows the points for which $\Delta k = 0\ \mathrm{m}^{-1}$. Conditions are the same as figure 3.5.*

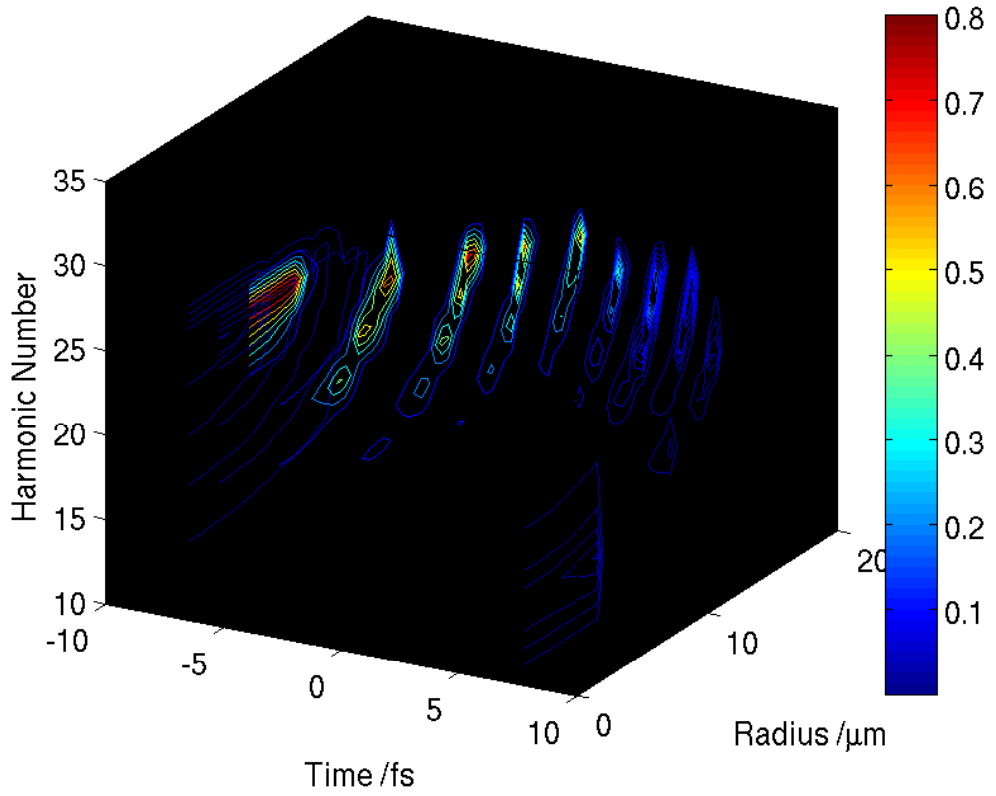

Figure 3.9: *XUV intensity build-up through the beam for the same conditions as figure 3.5. These are contour slices, taken at* 1.30 fs *intervals. Lines are contours of constant XUV intensity, with level of intensity (in arbitrary units) given by colour as indicated in the colour bar. Generation moves to larger radii and lower harmonics as time progresses.*

centred around the $\Delta k = 0\ \mathrm{m}^{-1}$ plane, though build-up does not occur at every point at which good phasematching occurs. Phasematching is necessary for build-up, but not sufficient. It is also required that the intensity of the fundamental is both high enough to cause ionisation, and high enough to generate a particular energy of XUV photon. To gain a more detailed understanding of processes at work in figure 3.9, it is useful to integrate the plots over one or more of the dimensions (time, space, harmonic number) and study the resulting figures.

Integration over one dimension

Figure 3.10 shows the result of integrating the 3D output in figure 3.9 over each of the three dimensions individually. Each plot shows a different aspect of the spatio-temporal effects of HHG. Figure 3.10(a) shows intensity integrated over harmonic number, to give a total intensity generated at each radius and time. As is expected from figure 3.8(b), harmonics are generated first at the centre of the capillary, then as ionisation increases, generation is pushed towards the edge of the capillary. At this point the generation begins to differ from the phasematching surface as, although the harmonics remain phasematched — in figure 3.7(a) the $\Delta k = 0\ \mathrm{m}^{-1}$ surface extends to $t = \infty$ — the fundamental intensity drops below the values necessary for generation. At these low intensities, the semi-classical cutoff drops below the harmonics considered here and ionisation also stops occurring; both of these factors cause generation to stop.

The notable feature of figure 3.10(a) is the pulsed nature of the XUV radiation that is generated. This is expected from a simple consideration of the semi-classical model of HHG (see section 2.1) and is included in this model by the dependence of intensity on the term $\mathrm{d}N$, the number of atoms ionised at a given position and time. This ionisation is strongly dependent on the instantaneous electric field strength of the fundamental, and so occurs once every half optical cycle at the (positive and negative) peaks of the field.

Figure 3.10(b) shows XUV intensity integrated over radius to show at what time

a particular harmonic in generated. In general, there is not much change in harmonic distribution with time, although a steady, but slight shift to lower energies is seen as time increases. This is due to lower harmonics being better phasematched at higher ionisation fractions, as seen in 3.2(b). As the ionisation fraction is increasing monotonically for every radius, phasematching should cause lower harmonics to be generated more efficiently at later times.

Figure 3.10(c) shows XUV intensity integrated over time to show the radial profile of each of the generated harmonics. The radial profiles do not change much with harmonic number, expect at the highest energies, where the sharp cutoff (section 3.4.5) limits the radii at which the intensity is sufficient to generate a particular harmonic. Thus the lower energy harmonics have smoother profiles, with the higher energies tending more towards "top-hat" profiles.

Integration over two dimensions

Although integration of intensity over one dimension is sufficient to gain an understanding of the output of the model, the available experimental results are not resolved over more than one dimension. The measurements that can be taken with the experimental arrangement available are restricted to the spatial profile of the harmonics (at some distance from the source) measured with an x-ray CCD camera, and the spectrum of the harmonics.

Figure 3.11 shows the sample output in figure 3.9 integrated over each combination of 2 dimensions to give temporal and radial profiles and a harmonic spectrum. These profiles will be compared with experimental data in chapter 4, but here we will look at the interesting features of the simulated data.

Figure 3.11(a) shows how the integrated XUV intensity varies with time. We see the expected sharp rise at the leading edge of the pulse as the ionisation fraction reaches the required values for phasematching, followed by a smoother trailing edge as the ionisation fraction stabilises. However, the driving intensity gradually decreases, causing a reduction in generation. The time profile is modulated at twice

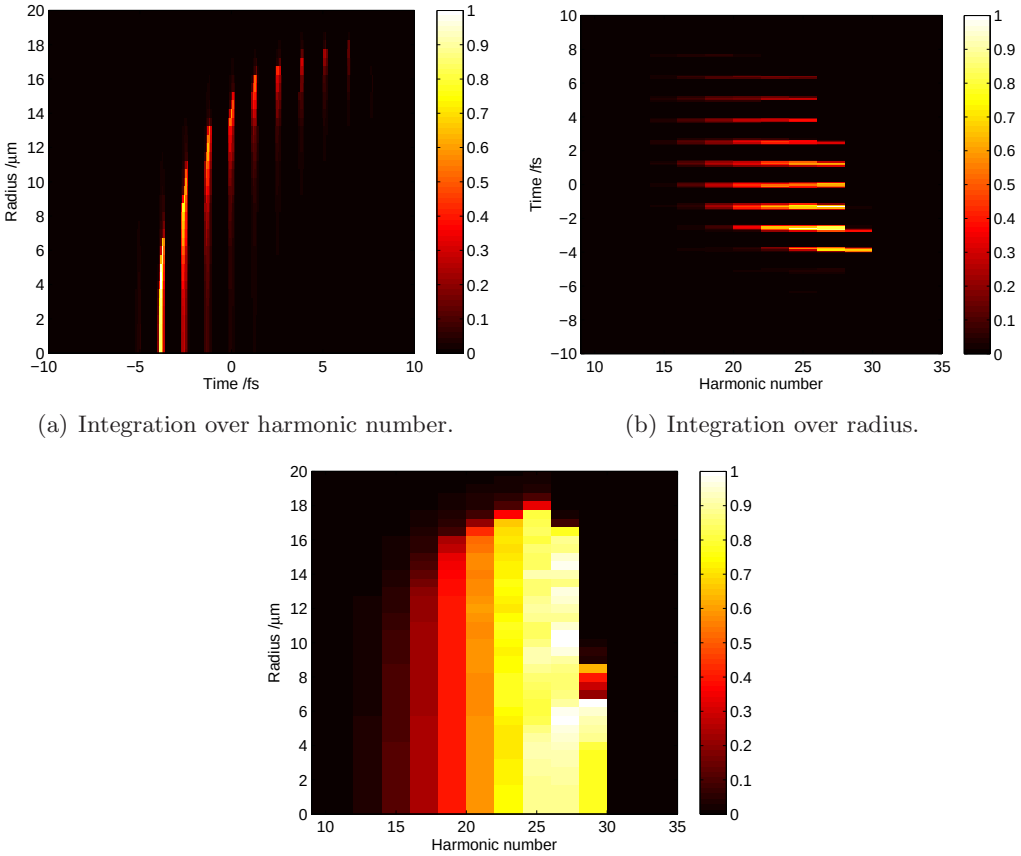

(a) Integration over harmonic number.

(b) Integration over radius.

(c) Integration over time.

Figure 3.10: *Generated XUV intensity the beam integrated over 1 dimension for the same conditions as figure 3.5. Colour is intensity in arbitrary units.*

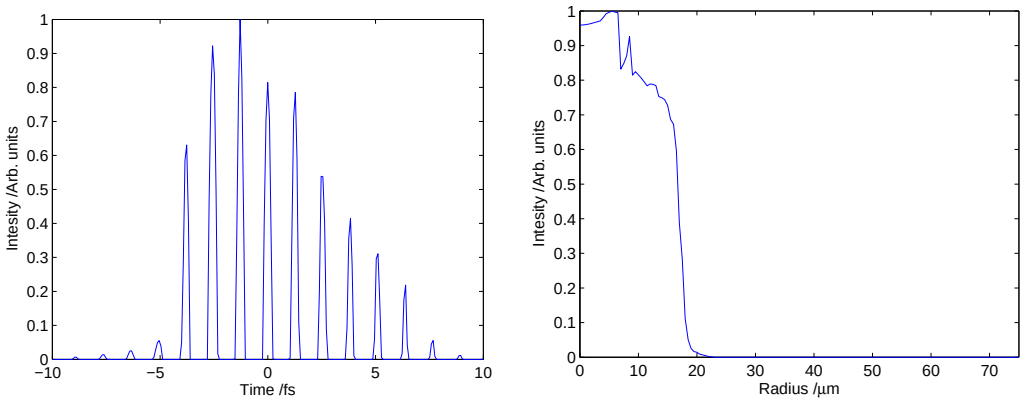

(a) Integration over radius and harmonic number.

(b) Integration over time and harmonic number.

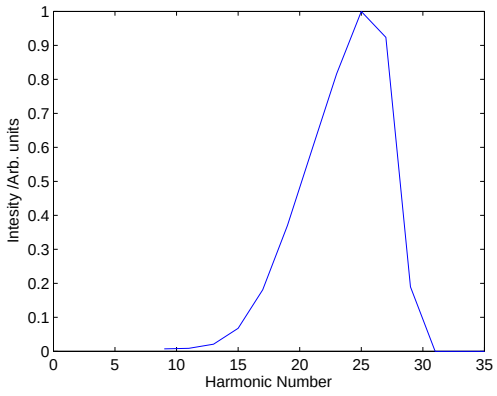

(c) Integration over radius and time.

Figure 3.11: *Generated XUV intensity through the beam integrated over 2 dimensions for the same conditions as figure 3.5.*

the fundamental frequency by the spike of generation occurring every half cycle of the laser. The number of spikes contributing to generation should affect the width of the harmonics in the observed spectrum. This effect could be the subject of further work and is discussed in detail in section 4.5.4.

Figure 3.11(b) shows the total emitted intensity as a function of radius. The profile is approaching a top hat structure, with the sharp edges caused by the highly nonlinear response. The flat top is caused by the phasematching in the centre causing a "saturation" effect where, although generation is very efficient at early times due to the large number of ions and high intensity, the process is self limiting because large numbers of ions reduce the efficiency of generation at later times.

Figure 3.11(c) shows the XUV intensity integrated over space and time. This gives a spectrum that is compared to experimental data in chapter 4. Here the spectrum is plotted against harmonic number, but as the harmonic energies and wavelengths are well known, it is simple to convert this plot to either a wavelength or energy scale.

3.6 Effect of increasing the intensity of the fundamental laser

It is shown above that phasematching causes HHG to become a self-limiting process; as any one region of the pulse generates efficiently, it also ionises, making generation at that radius at later times much less efficient. For this reason, trying to increase the efficiency by driving with a higher intensity laser is very unlikely to work. Equivalently, trying to extend the cutoff energy using a higher energy driving pulse will also fail. For the parameters used above, the highest harmonic generated is at the theoretical cutoff at the peak of the pulse, which is the 29th harmonic. If the energy of the driving pulse is increased by 50 %, the theoretical cutoff moves to the 39th harmonic, but the maximum generated harmonic is only the 31st. If the pulse is shortened by 33 % to give the same peak intensity and cutoff, the maximum

Pulse energy /μJ	339	509	339
Pulse length /fs	35	35	23.3
Peak intensity /W cm^{-2}	1.91×10^{14}	2.86×10^{14}	2.86×10^{14}
Cutoff harmonic at peak of pulse	29	39	39
Maximum harmonic generated	29	31	33

Table 3.1: *Semi-classical cutoff, as calculated at the peak of the pulse, and maximum observed harmonics for a variety of input laser parameters. In all cases the generating gas is argon at* 50 mbar *and the input wavelength is* 780 nm.

generated harmonic is the 33rd. These results are summarised in table 3.1. Thus, the maximum observed harmonic is not determined by the semi-classical cutoff calculated at the peak of the pulse, but is reduced by phasematching effects. Using higher intensity pulses, therefore, does not necessarily give access to higher energy harmonics, although the improvements to be made from shortening the pulse are greater than those gained by increasing the pulse energy.

3.7 Conclusions

The sample results presented above highlight some interesting insights into the generation process given by the phasematching model. One of these is that the variation of ionisation fraction with radius, as well as time, allows a large phase space in which phasematching can occur. Provided the pressure and intensity are such that $\Delta k = 0$ m^{-1} for a particular harmonic at some point in the capillary, then phasematching occurs at some radius at all later times. Examination of figure 3.10(a) at $r = 0$ μm shows that if this were not the case, then only one or two optical cycles would contribute to generation, and that phasematching could be used, with suitable tuning, to generate near-single attosecond pulses from multi-cycle driving pulses. Indeed, this technique may still be possible if a mechanism can be found to separate the spatial components of the XUV beam. If the driving laser could be filtered out, such spatial separation could be achieved with a ~ 5 μm pinhole. However, this would need to be done before propagation effects distort the space-time profile of the XUV pulse and in this region the fundamental laser is sufficiently

intense that filtering with any optical element is problematic.

Another interesting effect caused by the rapidly changing ionisation fraction is that the generation is self limiting. At an intensity that is sufficient to generate, the ionisation fraction is rapidly increasing and so poor phasematching prevents subsequent efficient generation. This means that, to first order, any radial region that generates at all, generates at roughly the same efficiency, leading to the predicted roughly top hat radial profiles. It is shown that, for the same reason, attempts to increase the XUV flux or cutoff energy by increasing the intensity of the driving laser will only have a very limited effect.

Having described the model used for predicting phasematching, the next step is to test it by comparison to experimental data. This comparison is undertaken in chapter 4.

Chapter 4

Comparison of phasematching modelling to experiment

The experimental parameter measurements and spectra described in this chapter were taken by other members of the group, primarily Chris Froud, Richard Chapman, Matthew Praeger, Sarah Stebbings and Ana de Paula. The theoretical work and discussion is my own.

Having presented the development of the spatio-temporal phasematching model in chapter 3, the model is compared to experimental results in this chapter. This allows validation of the model and reveals its uses as a tool for developing more efficient and controllable HHG sources.

The first part of this chapter (section 4.1) deals with the determination of the necessary input parameters for the model from experimental measurements. Having determined these, the theoretically predicted spectra are compared to experiment for a selection of gases in section 4.2. Section 4.3 then extends the comparison to mixtures of gases. In section 4.4, the spatial and phase profiles predicted by the model are used to investigate how the XUV beam propagates after leaving the capillary. The divergence of the generated XUV beam is predicted. Section 4.5 discusses possible extensions and developments of the phasematching model. A

development is proposed that would allow the model to take account of the real pressure profile in the capillary. Additionally, a proposal is made for further use of the model in estimating the number of XUV pulses in the attosecond pulse chain generated by the HHG source.

4.1 Determination of experimental parameters

In order to predict XUV generation using the model presented here, it is necessary to know the wavelength, pulse energy and pulse length of the driving laser and the pressure of the gas.

As discussed in section 3.4.2, the length over which the XUV radiation builds up is small — no longer than the absorption depth in the medium. Since the absorption depth is no greater than a few millimetres,[1] any XUV photons generated towards the entrance of the capillary will have been absorbed before they leave the capillary. For this reason, the generation region is not only short, but also located at the end of the capillary, in the last absorption depth. Therefore, the relevant values of the experimental parameters are those at the output of the capillary rather than the input. The following sections (4.1.1–4.1.4) discuss the experimental measurements and fitting techniques used to determine these parameters for input to the model.

4.1.1 Pulse energy

The output pulse energy was determined by measuring the output average power from the capillary, and dividing by the repetition rate of the laser. The output energy is less than the input pulse energy due to imperfect coupling into the capillary, transmission losses in the capillary and ionisation losses in the gas. These factors are discussed in more detail in chapter 5.

Figure 4.1 shows the measured output power from the capillary as a function of pressure for four different gases. These gases are the ones that have been used in our experimental setup, and so the ones of interest here. In order to calculate the

[1] See section 2.6 for details.

output average power at an arbitrary pressure, the pressure response of each gas is fitted to an empirical curve of the form

$$P_{\text{avg}} = ae^{bp} + c, \tag{4.1}$$

with a, b and c the parameters of the fits, P_{avg} the measured output power and p the pressure in bar. The form of this equation was chosen as it fits the experimental data well, but it is not suprising that such a form provides a good fit. The pressure dependent loss processes in the capillary are caused by ionisation, which is in turn related to the energy of the pulse at a particular location (equation (4.1)). As the pulse energy is reduced the ionisation losses will be reduced, leading to a saturating loss term (the exponential term in equation (4.1)). Once the energy drops below some certain threshold (dependent on the gas), then ionisation will cease, and no more losses will occur. This leads to the constant term c in equation (4.1).

Fits to equation (4.1) are shown in figure 4.1 as solid lines. These parameters are then stored for each gas, and can be retrieved and used to calculate the output power for a given gas and pressure for input to the phasematching model. The parameters for each gas are shown in table 4.1. The fits are approximations due to the somewhat arbitrary choice of fit equation and possible experimental error. This leads to the values of output power for different gases not converging at zero pressure. This is not physical, but the errors introduced by this will be small, as generation is not possible at zero pressure and is weak at very low pressures. The fits could be forced to converge at zero pressure, but only at the expense of worse fits at higher, more experimentally interesting, pressures.

For each gas we see that the pressure dependent losses scale with the probability of ionisation. For the same input laser pulse, most ionisation is expected for nitrous oxide, followed by argon and nitrogen at roughly similar levels. The lowest levels of ionisation are expected in neon. A simple consideration of the loss mechanisms present — energy loss through ionisation and loss through nonlinear coupling to

Gas	a	b	c
Argon	0.142	-14.7	0.213
Nitrogen	0.188	-7.23	0.175
Neon	0.0102	-366	0.370
Nitrous oxide	0.292	-7.57	0.0868

Table 4.1: *Best fit parameters of equation 4.1 for each of the four gases used experimentally.*

Parameter	m	C
a	3.34×10^{-4}	-0.125
b	-0.0368	14.7
c	1.50×10^{-4}	0.0931

Table 4.2: *Best fit parameters for linear fits $y = mx + C$ to the plots in figure 4.3.*

higher order modes[2] — shows that greater loss is expected for greater levels of ionisation. For any particular gas, the power losses "saturate" at a particular level; this is the energy at which the intensity of the laser has dropped sufficiently to reduce any further ionisation to negligible levels.

While this is the only procedure necessary for nitrogen, neon and nitrous oxide, for argon the situation is complicated by the fact that we have also investigated the dependence of XUV emission on input power. To incorporate this input power variation into the model, the output power was measured as a function of pressure for various input powers (crosses, figure 4.2), and equation (4.1) fitted (dotted lines, figure 4.2). To interpolate this across various input powers, the parameters a, b and c are plotted against input power (figure 4.3). As the points lie approximately on a straight line, a straight line is fitted to each fit parameter as a function of input power. These straight line fits can be used to determine the exponential fit parameters a, b and c for a given input power which can then be used with equation (4.1) to determine the output power at a given pressure. The parameters of the linear fits are given in table 4.2. The values of a, b and c calculated from the linear fits are used to produce the solid lines in figure 4.2.

The final factor to take into account is that the measured powers are those after

[2]Higher order modes have higher losses per unit length. See section 2.3 for more details.

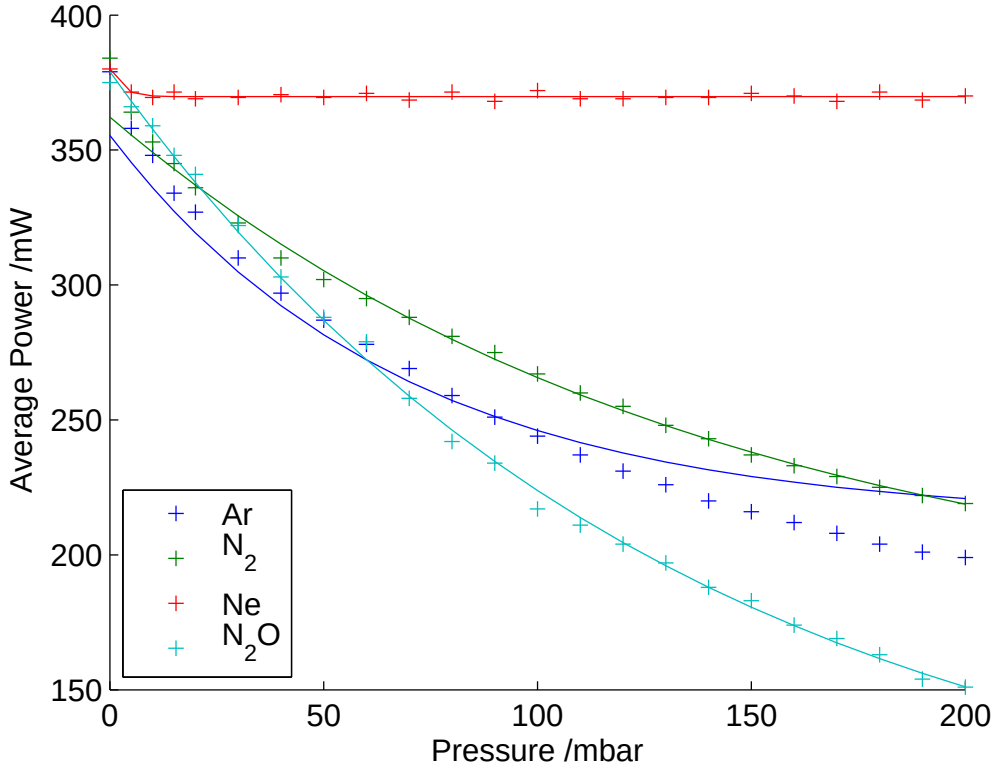

Figure 4.1: *Output average power from the capillary as a function of gas pressure for argon, nitrogen, neon and nitrous oxide. Crosses are experimentally measured values. Solid lines are exponential fits.*

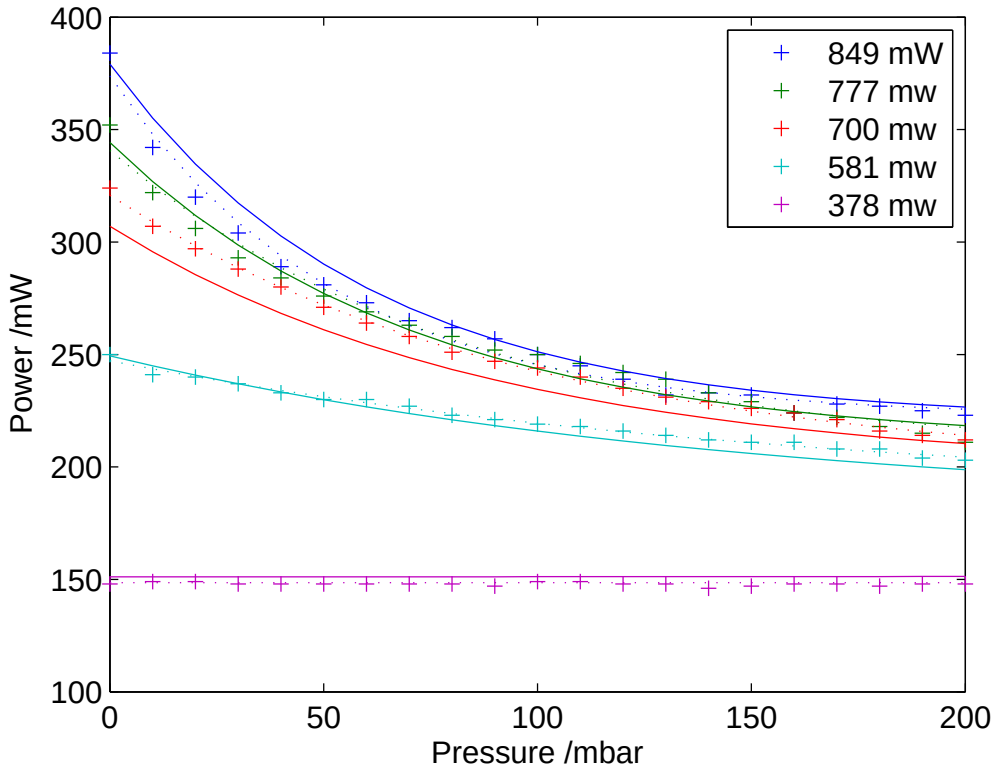

Figure 4.2: *Output average power from the capillary as a function of gas pressure for argon at various input powers. Crosses are experimentally measured values. Dotted lines are exponential fits. Solid lines are generalised fits (see text).*

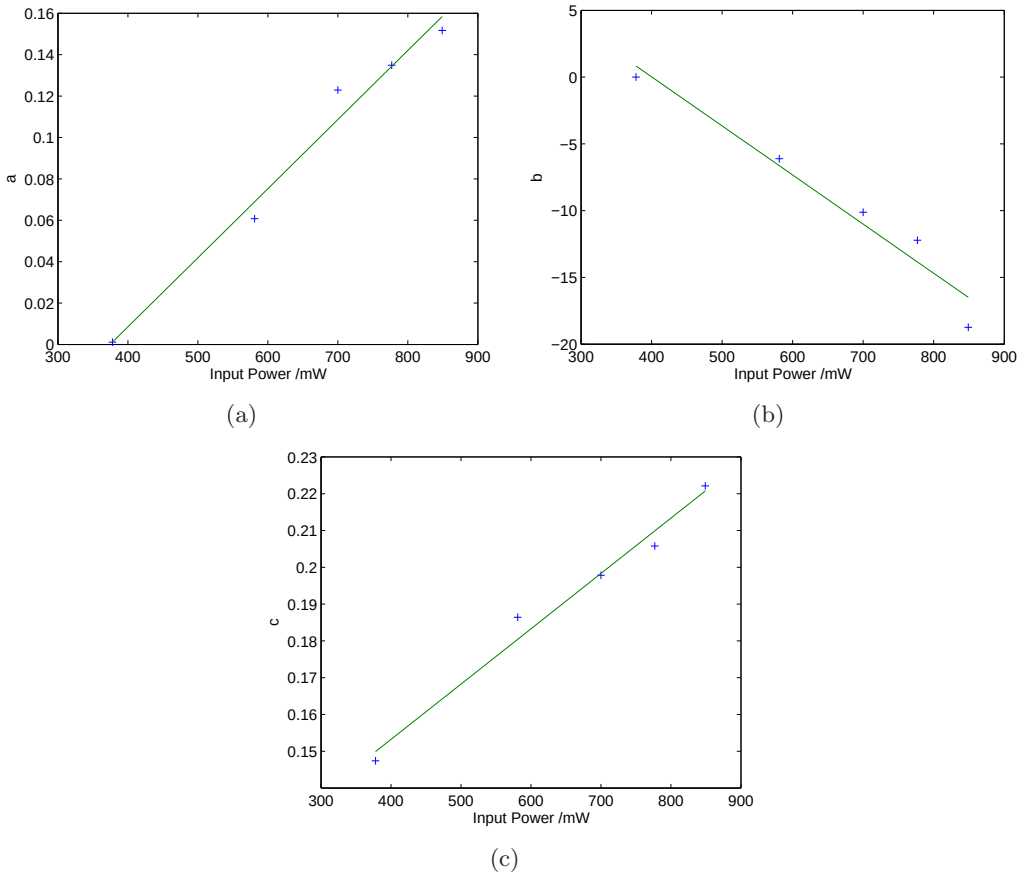

Figure 4.3: *Straight line fits (solid lines) to calculated values of the a, b and c parameters (crosses) in equation (4.1) as a function of input power.*

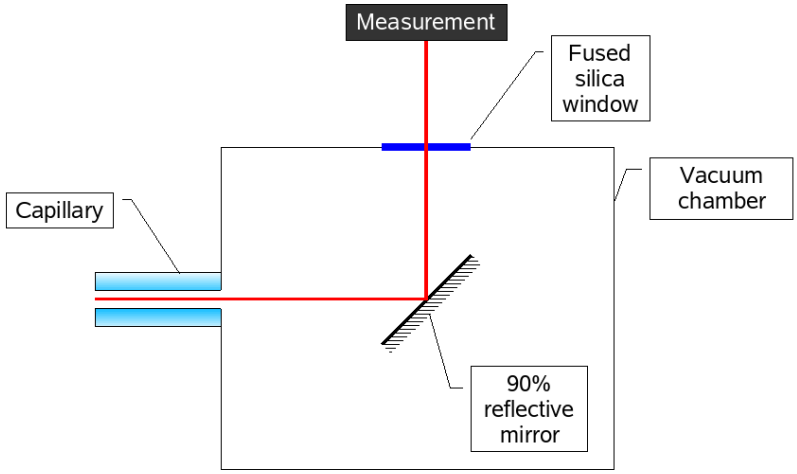

Figure 4.4: *Experimental arrangement used for measuring the laser properties after propagation through the capillary. The mirror is silvered, so has a large reflective bandwidth. The exit window is not anti-reflection coated, so loses 4 % of power at each surface. The following instruments can be placed at the 'Measurement' location: spectrometer, power meter, FROG or CCD camera. These measure pulse energy, pulse spectrum, pulse time profile and spatial profile respectively.*

reflection off one turning mirror with a 90% reflectivity and propagation through a non-anti-reflection coated, fused silica window (figure 4.4). The power at the capillary exit P_{cap} is therefore given by

$$P_{\text{cap}} = P_{\text{avg}} \times 0.9 \times 0.96^2. \tag{4.2}$$

4.1.2 Wavelength

The central wavelength of the fundamental pulse is also seen to shift with propagation in the capillary. This effect has previously been observed in other experiments [82, 129, 130] and is caused by propagation in an ionising gas.[3] The measured

[3] Chapter 5 discusses this in more detail.

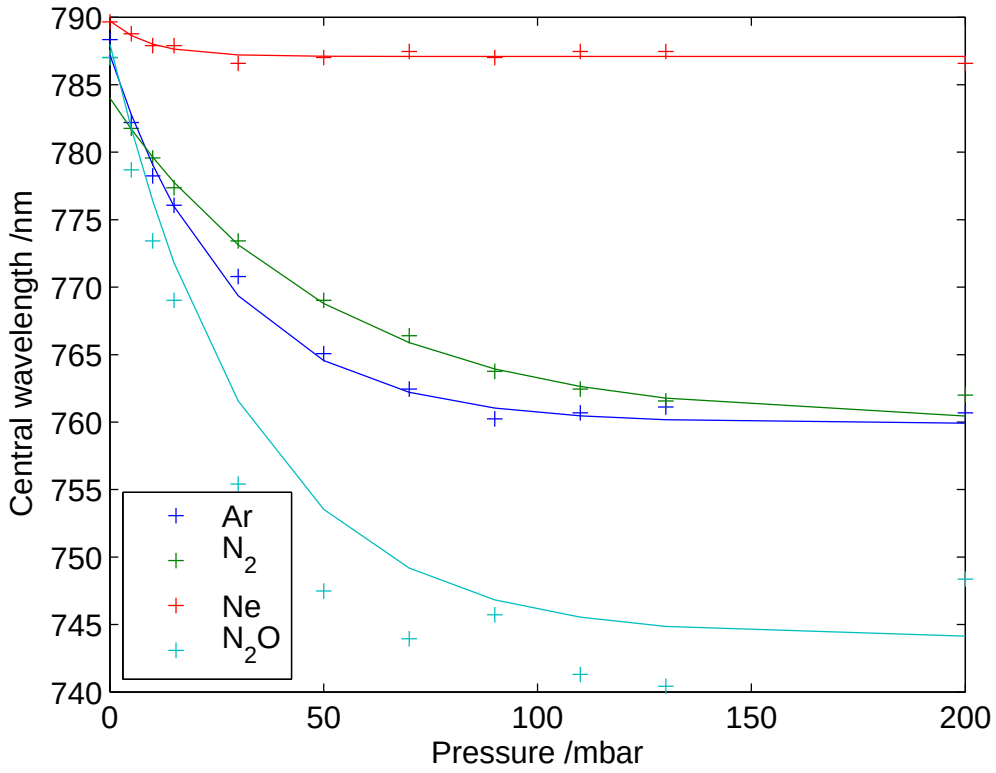

Figure 4.5: *Output central wavelength from the capillary as a function of gas pressure for argon, nitrogen, neon and nitrous oxide. Crosses are experimentally measured values. Solid lines are exponential fits.*

central wavelength (defined as the median point in the output spectrum) of the pulse in plotted (crosses) in figure 4.5. The shape of the curves are seen to be similar to those in figure 4.1. Hence the same empirical curve is used

$$\lambda_0 = ae^{bp} + c \tag{4.3}$$

with a, b and c the parameters of the fits and λ_0 the measured central wavelength. The similarity of the curves is not unexpected, as both the loss and the shift are ionisation dependent effects. This means that if the power loss saturates at high pressure, when the intensity drops below that need to ionise the gas, the wavelength shift should also saturate. As before, these values of a, b and c are stored and used to calculate the expected central wavelength of the pulse for a given gas and pressure.

4.1.3 Pulse Length

The pulse length used in the calculations is taken to remain at the input value of 35 fs with no pressure dependence. This is consistent with results in the literature (see section 5.1 for a discussion of this), which show no significant temporal reshaping of the pulse as it propagates through the capillary at the experimental intensities and pressures used here. It is also consistent with experimental measurements taken after the output window in figure 4.4.

4.1.4 Gas Pressure

The gas pressure used in the phasematching calculation is that of the constant pressure region in the centre of the capillary. This is because the model described in chapter 3 is limited to a constant pressure. The effect of this, and the changes to the model necessary to relax this assumption, are discussed in section 4.5.1.

4.2 Effect of generating gases

Having determined the experimental parameters for input to the model, the following sections discuss the use of the model and its comparison with experimental results.

Figure 4.6 shows the experimental and theoretical spectra for various gases at a generation pressure of 50 mbar. The shapes of the experimental spectra and the highest observed energies are reproduced well by the calculations, as are the relative intensities of the harmonics. The details of the spectrum are determined by the absorption profile and differences in phasematching between harmonics. As the calculations do not give a quantitative value for XUV flux, the spectra are normalised such that the maximum value in each spectrum is 1. The method used here cannot reproduce the harmonic structure of the XUV radiation and so only gives an envelope under which the experimental harmonics should appear.

In figure 4.7 the predicted XUV generation is shown as a function of time and space for various gases, together with the driving laser intensity. The region of

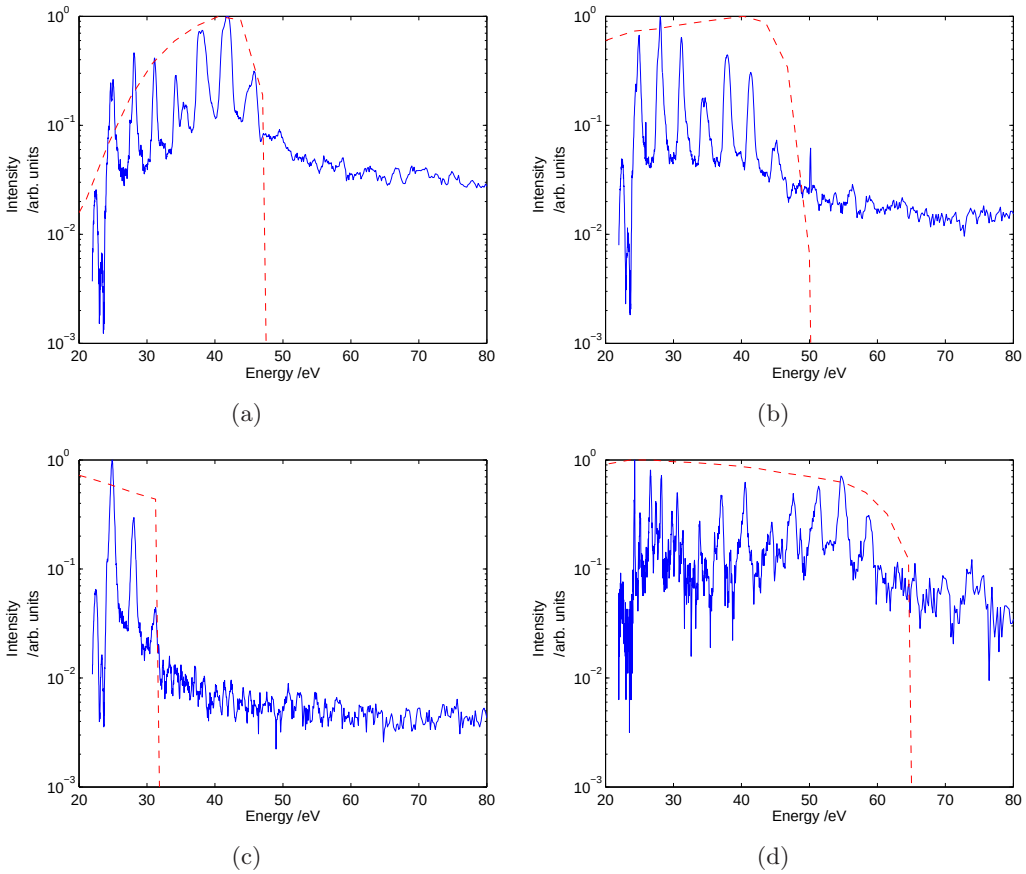

Figure 4.6: *Experimental (solid) and theoretical (dashed) spectra for (a) argon, (b) nitrogen, (c) nitrous oxide and (d) neon at* 50 mbar. *The calculations reproduce well the relative intensities of the harmonics, the shape of the spectra and the high energy cutoff.*

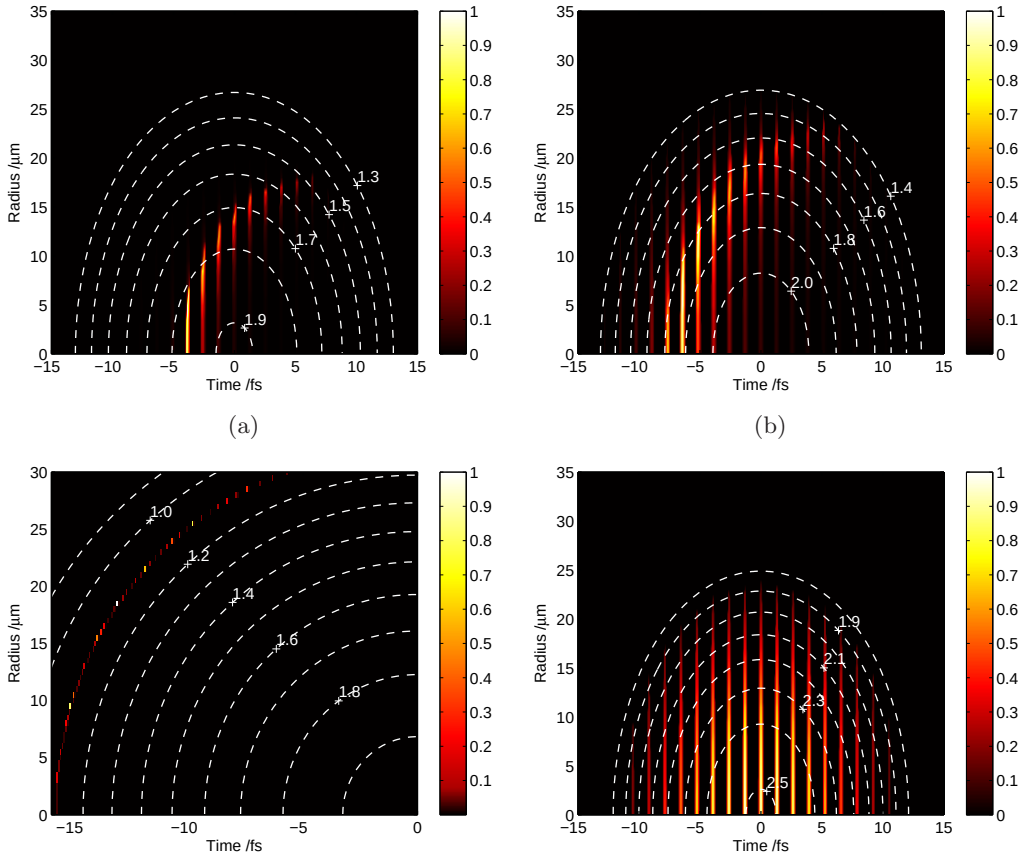

Figure 4.7: *Theoretical prediction of generation — summed over all harmonics — for (a) argon, (b) nitrogen, (c) nitrous oxide and (d) neon as a function of time and radial position in the capillary, relative to the peak of the pulse. The colour scale indicates harmonic intensity . The contours are lines of constant fundamental intensity with labels in* 10^{14} W cm^{-2}. *The* 1.1×10^{14} W cm^{-2} *contour has been omitted and the colour scale adjusted in (c) for clarity.*

space and time in which phasematching occurs is determined by the phasematching conditions, and therefore the ionisation fraction. The contours along which generation occurs are therefore regions of approximately constant ionisation fraction. Generation occurs first in the centre of the capillary and at the leading edge of the pulse as the ionisation passes through the value at which $\Delta k = 0$. As the intensity increases, the gas on axis continues to ionise, and the fraction becomes too high for efficient generation. The phasematched region then moves towards the edge of the capillary where the ionisation fraction is lower than at the centre. The region in which harmonics are generated directly affects the spectrum of the XUV radiation produced, as harmonics produced in lower intensity regions have a lower cutoff energy (equation (3.29)).

Figures 4.7(a) and (b) for argon and nitrogen show that generation occurs primarily in a region of intensity $1.7 - 1.9 \times 10^{14}$ W cm^{-2}. For an intensity of 1.8×10^{14} W cm^{-2}, the theoretical cutoff is at 48 eV. Figures 4.6(a) and (b) show that this cutoff is seen in both the experimental and theoretical data. In figure 4.7(c) the generation region is shown for nitrous oxide. Here almost all generation occurs at 1.1×10^{14} W cm^{-2}, which gives a theoretical cutoff at 38 eV, again this is reproduced in figure 4.6(c). Figure 4.7(d) shows that for neon, generation occurs at around 2.5×10^{14} W cm^{-2}, with a cutoff of 61 eV, again seen in the corresponding spectra in figure 4.6(d). The peak intensity of the fundamental is higher in neon as lower levels of ionisation lead to lower ionisation losses in the capillary.

This analysis clearly demonstrates that phasematching conditions are limiting the energy of the harmonics that are produced, not just by directly phasematching particular wavelengths preferentially, but also by limiting the laser intensity that can be used to generate them efficiently. This reduced intensity limits the maximum energy of the harmonics that can be generated, and this relationship is well described by the semi-classical three-step model.

4.3 Gas mixtures

Using the methods given above, it is possible to calculate the phasematching properties for any single gas at any pressure. The gas properties necessary to perform this calculation are the (complex) refractive index and the ionisation properties.[4]

To extend the phasematching calculation to mixtures of gases is, therefore, relatively simple, given that all the above properties are known for both gases. The ionisation fraction of each gas can be calculated independently, and the refractive index calculated for the combination of gases. If $n_{\text{atm}} = 1 + \delta_{\text{atm}} + i\beta_{\text{atm}}$, then for one gas $\delta_{\text{gas}} = 1 + (P\delta_{\text{atm}})$ and $\beta_{\text{gas}} = P\beta_{\text{atm}}$. If the molar fraction of gas m is given by f_m then the refractive index of a gas mixture is given by:

$$n_{\text{mixture}} = 1 + \sum_m \left[f_m \delta_m + i f_m \beta_m \right]. \tag{4.4}$$

When examining the output from the phasematching calculation (sections 3.5, 4.2), it was seen that the ionisation is limiting the intensity used to generate harmonics. This limitation means that the experimentally observed cutoff is less than that predicted by the peak intensity of the pulse, and is, in fact, that calculated using the intensity at which the pulse reaches the correct ionisation fraction to generate. A potential solution to this problem is to add a non-ionising buffer gas to the capillary. This gas would contribute to the neutral gas refractive index without affecting the number of electrons, and therefore the refractive index contribution of the plasma. At the experimental intensities used here, helium is not significantly ionised by the laser, and so is a suitable buffer gas.

As expected, figure 4.8 shows that the phasematching points for mixtures of argon and helium move to higher ionisation fractions as the partial pressure of helium increases. This should increase both the efficiency of generation and the highest energy generated. However, these increases will be somewhat offset by the extra absorption introduced by the relatively large pressure of helium. Looking at

[4] See section 2.2 for full details of ionisation parameters.

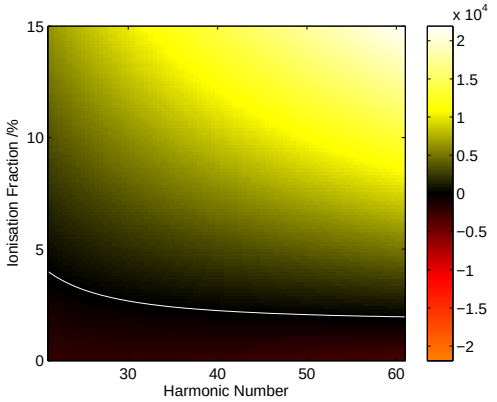

(a) Partial pressure of helium: 0 mbar

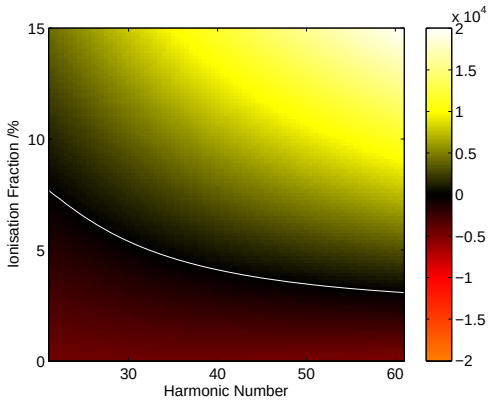

(b) Partial pressure of helium: 50 mbar

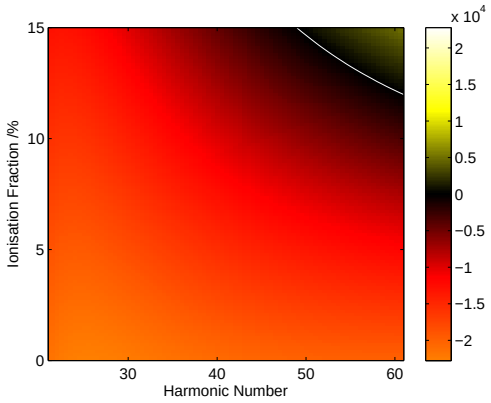

(c) Partial pressure of helium: 450 mbar

Figure 4.8: *Δk for mixtures of argon and helium as a function of ionisation fraction and harmonic number. In all three figures, the partial pressure of argon is* 50 mbar*. Colour represents $\Delta k/\mathrm{m}^{-1}$ and the white line shows the points where $\Delta k = 0\ \mathrm{m}^{-1}$.*

figure 2.16, we see that helium is even more absorbing in the relevant energy range than argon, and this will reduce the overall efficiency considerably. However, helium, like most of the gases in figure 2.16, becomes more transparent at higher energies. This means that the higher cutoff effect should not be reduced by the absorption of the helium. A mixture of argon and helium should, from this static analysis, produce higher energy harmonics, but at lower efficiency than the same number of argon atoms with no helium present. Below, I investigate whether 3D modelling confirms this conclusion, and compare the 3D model to experimental results to test it.

Comparison of theory and experiment for gas mixtures

Figure 4.9 shows the experimental and theoretical spectra of argon-helium mixtures. with approximately the same partial pressure of argon and varying partial pressures of helium. Unfortunately, no experimental data exists for which it is possible to produce these plots with exactly the same partial pressure of argon. As expected from the static analysis, the cutoff in the theory plots increases with increasing helium pressure. The increase is not as large as might be expected from the static analysis, but there are a number of other effects (for example, absorption and single atom cutoff) that could be the cause. The experimental data also show a slight increase in cutoff, though not as large in magnitude as the predicted change. The reason for this discrepancy is unclear, but it could be due to slight inaccuracies in the relative ionisation rates, or absorption depths of helium and argon, neither of which are known precisely (as discussed in sections 2.2 and 2.6.)

4.4 Properties of emitted XUV beam

One output from the phasematching model presented in chapter 3 is the radial intensity profile of the emitted XUV radiation.[5] This information, together with the phase information from the semi-classical model, can be used to predict the

[5]See figure 3.10(c) for examples of this.

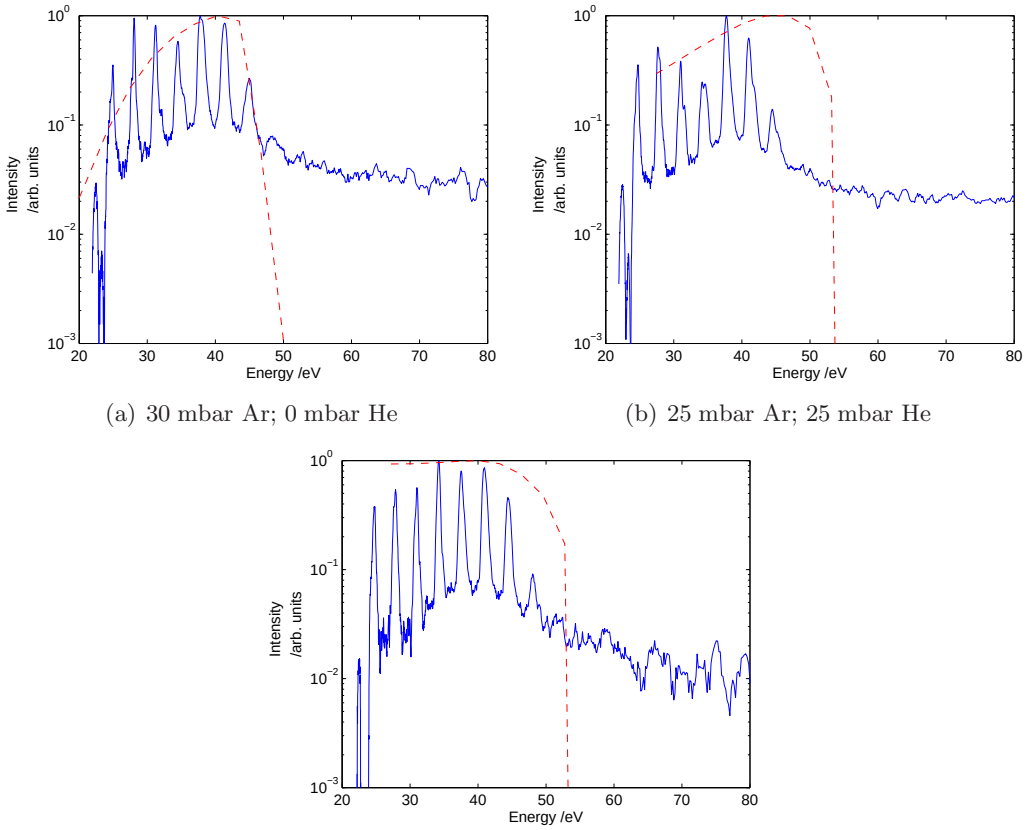

(a) 30 mbar Ar; 0 mbar He

(b) 25 mbar Ar; 25 mbar He

(c) 20 mbar Ar; 180 mbar He

Figure 4.9: *Predicted and observed spectra for approximately constant partial pressure of argon and varying partial pressures of helium. The exact values of argon pressure were determined by the available experimental data. As the helium pressure increases, both the theory and the experiment show an increase in the cutoff energy, although agreement is not as good in the mixtures as in the pure gas.*

x-ray propagation from the exit of the capillary. Here a combination of the angular spectrum method [131] (ASM) and far-field, Fraunhofer, diffraction [41] can be used to determine the spatial electric field profile at any propagation distance. These propagation calculations can be used to give quantitative predictions of the XUV beam quality parameters such as the divergence and M^2 parameter.

This section presents the calculations that have been performed, their results and comparisons with initial experimental measurements.

4.4.1 Phase profile across capillary

Assuming that the harmonics have been generated by electrons following the short semi-classical trajectories, as discussed in section 3.4.2, the phase of the XUV beam is found as a function of radius using the semi-classical calculations of phase (section 2.1) for the known intensity profile of the fundamental in the capillary. Figure 4.10 shows the phase profile for the short trajectories corresponding to the 19th harmonic. The phase is seen to be approximately spherical and converging, with a radius of curvature of 137 mm.[6]

Figure 4.11 shows how the phase profile varies with harmonic number. The most significant feature of this figure occurs at the 17th harmonic, where the phase profile of the emitted beam is approximately flat. For harmonics above 17, the shape of the profile is the same as that of the 19th harmonic, a converging beam with an approximately spherical curvature. The curvature increases with increasing harmonic number. For harmonics below the 17th, the phase profile is no longer spherical and more importantly it is no longer converging. Again, the curvature increases as you move further from the 17th harmonic.

This curvature causes an effective focus in the higher harmonics, as can be seen in figure 4.17. The position of this focus can be controlled to some extent by varying the peak intensity of the pulse. However, changing the peak intensity also affect the spatial profile of the generated beam (as discussed in section 4.4.2) and so will

[6]The sign convention used here for radii of curvature is that a positive radius corresponds to a converging beam, and a negative radius to a diverging beam.

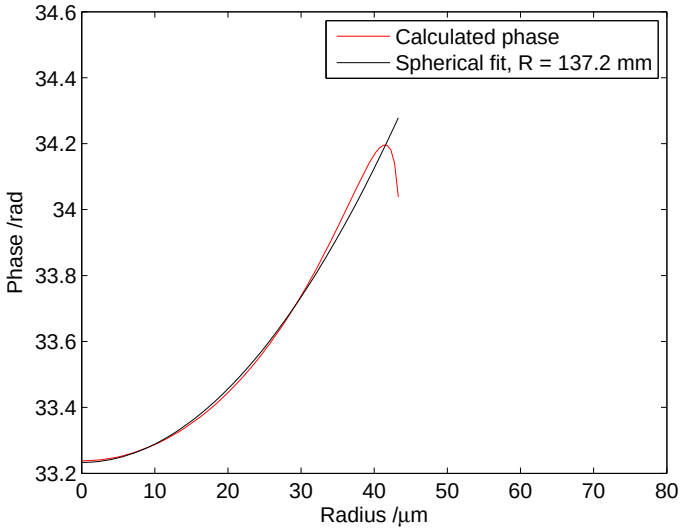

Figure 4.10: *Phase of the 19th harmonic as a function of position within the capillary together with a quadratic fit. The peak intensity is* 2.5×10^{14} W cm^{-2} *and the capillary radius is* 75 μm*. Beyond* 43.8 μm *the intensity is too low to generate the 19th harmonic.*

affect the propagation in complex ways. Potentially, the phase profiles could also be controlled by spatial shaping of the fundamental intensity profile, but this would also affect the intensity profiles of the generated radiation. Also, as the generation is taking place in a waveguide, spatial shaping of the beam has to take into account the modal nature of the capillary propagation. In principle, any intensity profile can be generated from combinations of modes, but the profile at a particular z position in the capillary is not necessarily the same as the at the start, due to beating between the capillary modes (discussed in section 5.6) and propagation loss of the modes. For this reason, spatial shaping of the fundamental pulse in the waveguide, although possible, is complicated.

Although the phase does not fit well to a spherical profile for all harmonics, it is still instructive to examine radius of curvature of the best spherical fit R as a function of harmonic number, as this gives a measure of the divergence of the beam. As the scaling of the radius of curvature makes it difficult to examine, figure 4.12 shows a plot of $1/R$ against harmonic number. Figure 4.12 shows that $1/R$ varies smoothly with harmonic number, passing through 0 m^{-1} at $q = 17$ as expected from

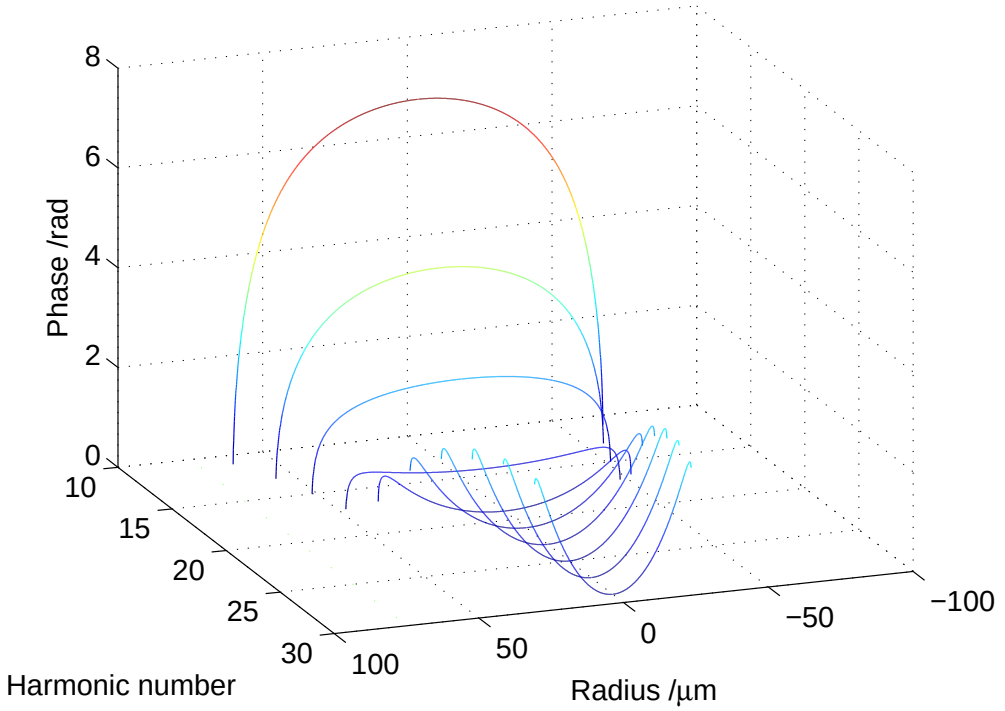

Figure 4.11: *Phase profiles as a function of harmonic number and radius. The blank regions are those where the relevant harmonic cannot be generated at a particular radius. Parameters are the same as those in figure 4.10.*

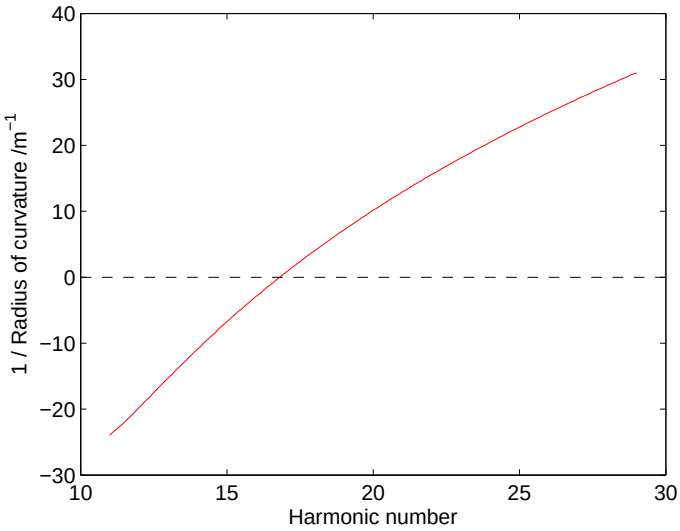

Figure 4.12: *Curvature $(1/R)$ of the best spherical fit to the phase profile as a function of harmonic number. Parameters are the same as those in figure 4.10.*

figure 4.11. The largest value of $1/|R|$ in the range of harmonics relevant here is 31 m^{-1}, corresponding to a radius of curvature of 32 mm which is long on the scale of the generation length of the harmonics.

For comparison, the phase profiles of the long trajectories are plotted in figure 4.13 and the curvature in figure 4.14. The extremely large phase shifts across the beam in figure 4.13 and the high values of curvature in figure 4.14 can both be explained by the much stronger dependence of semi-classical phase on intensity for the long trajectories, as described in section 2.1.3.

The high values of curvature seen suggest that the XUV radiation generated by the long trajectories will be much more divergent than that generated by the short trajectories.

4.4.2 Intensity profiles across the capillary

The predicted intensity profiles of the harmonics have been discussed briefly in section 3.5; here the profiles are investigated from the perspective of their propagation properties. Figure 3.10(c) is reproduced here on a larger scale in figure 4.15. As before, it is seen that the lower harmonics have a smoother structure, while the higher

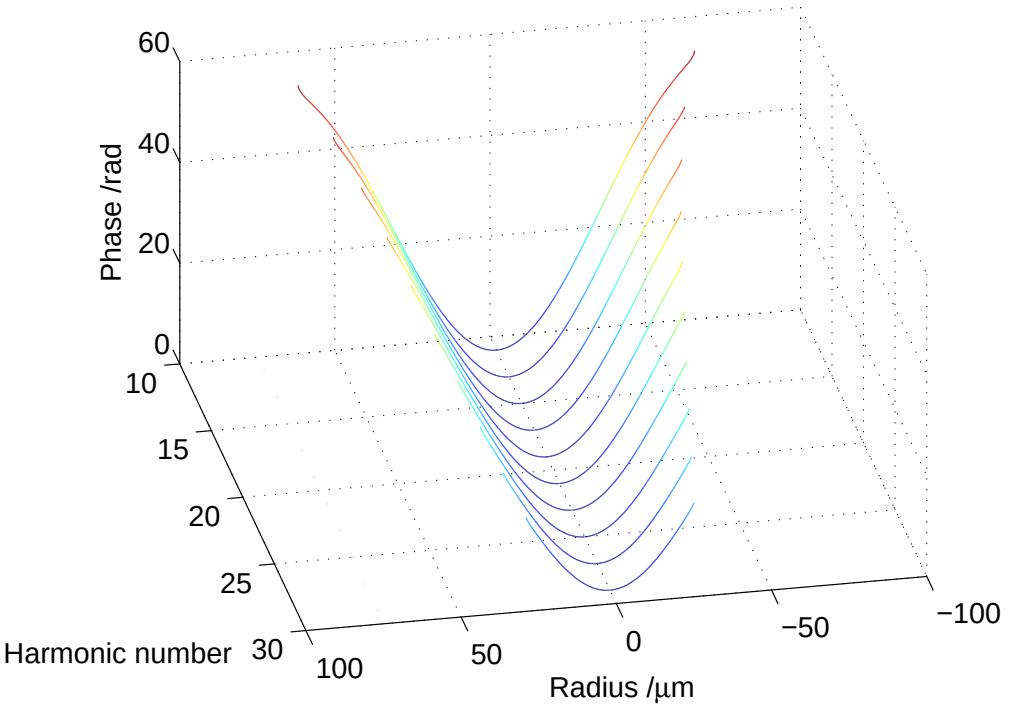

Figure 4.13: *Phase profiles of the long trajectories as a function of harmonic number and radius. The blank regions are those where the relevant harmonic cannot be generated at a particular radius. Note the very different phase scale compared to the short trajectories (figure 4.11). Parameters are the same as those in figure 4.10.*

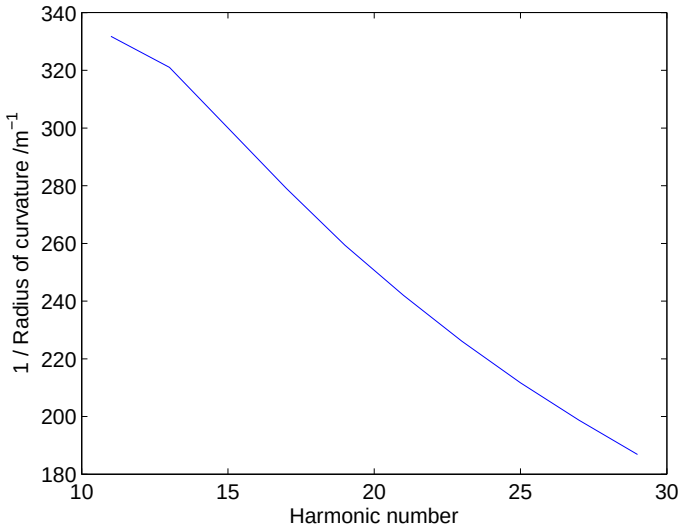

Figure 4.14: *Curvature $(1/R)$ of best spherical fit to the phase profile of the long trajectories as a function of harmonic number. Parameters are the same as those in figure 4.10.*

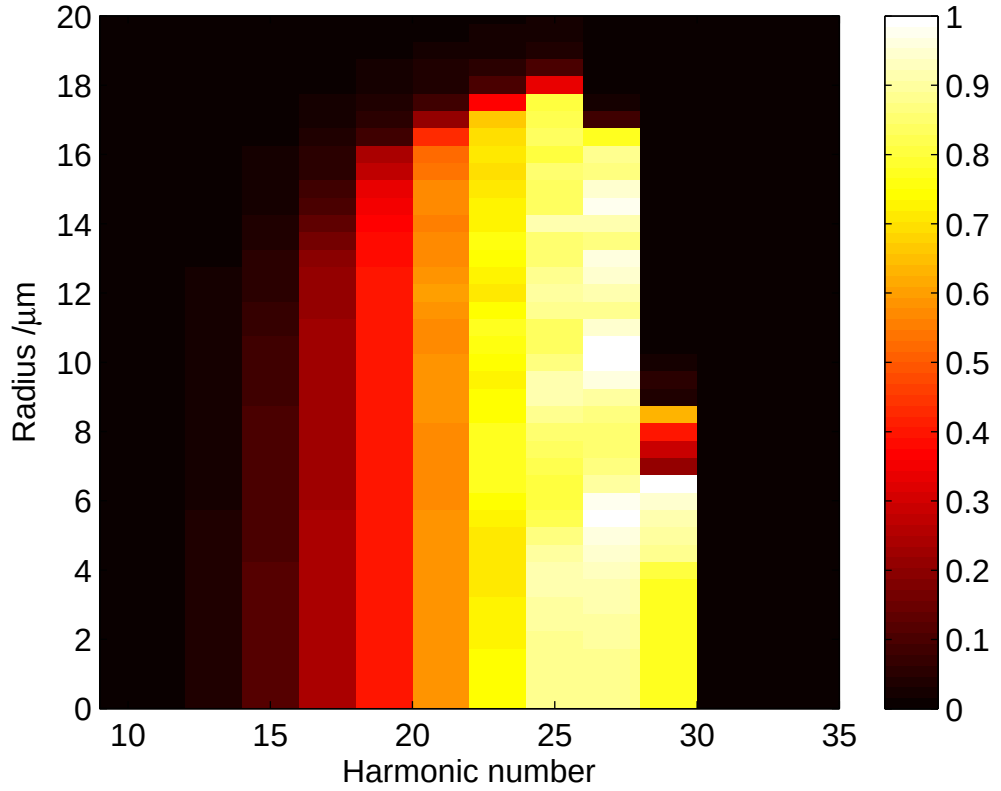

Figure 4.15: *Predicted radial intensity profiles for each harmonic for the same conditions as figure 3.5. Colour is intensity in arbitrary units.*

harmonics have sharper edges in the region where the semi-classical cutoff occurs and greater fine structure in the centre. Figure 4.16 shows the intensity profiles from figure 4.15 in a more intuitive manner, showing the beam profiles of each harmonic from the 13th to the 29th. A simple analysis of these profiles indicates that the lower harmonics will diverge less than the higher ones, due to the intensity profile alone, even ignoring the phase profile and the difference in wavelength between harmonics.

4.4.3 Propagation of the XUV fields

Given the phase and intensity profiles above, it is possible to derive a full electric field profile. This field profile can then be propagated numerically using well understood techniques. In this case, the angular spectrum method [131] is used in the near field

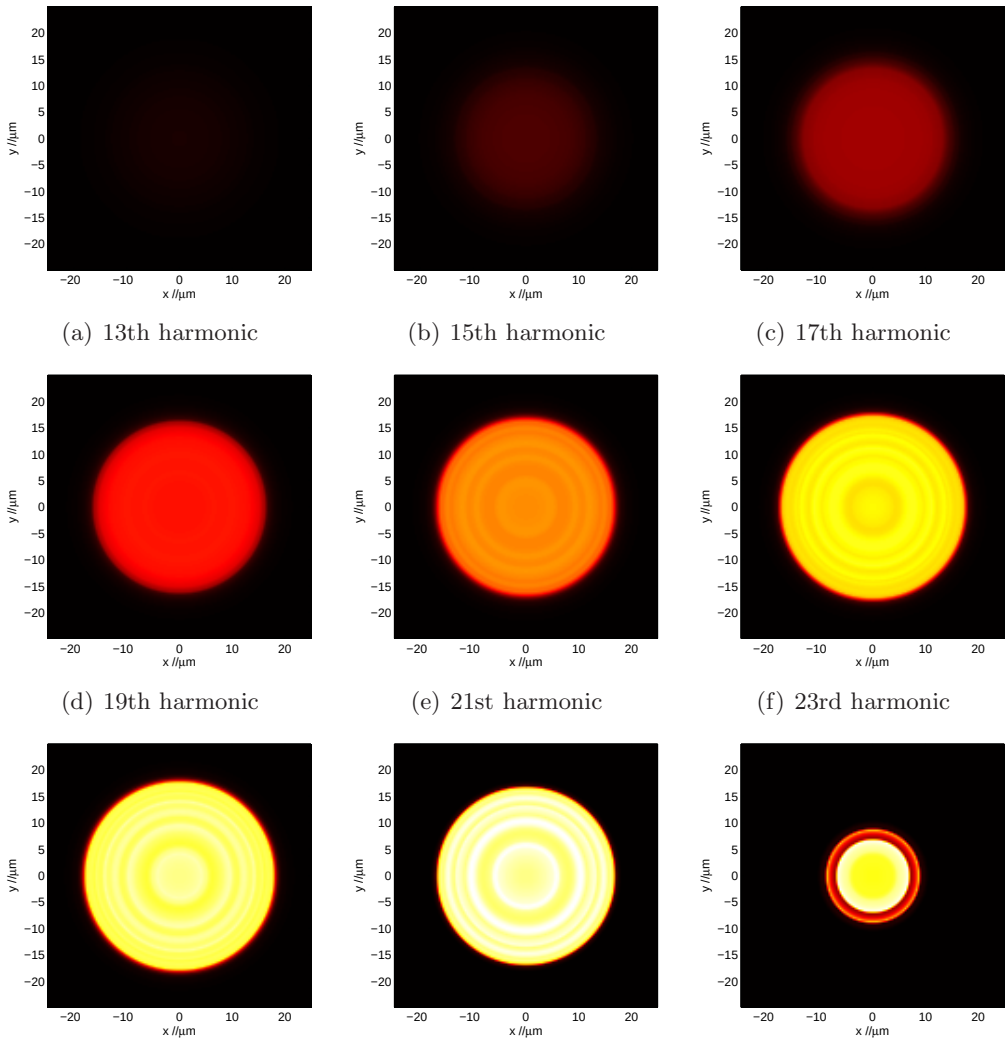

(a) 13th harmonic (b) 15th harmonic (c) 17th harmonic

(d) 19th harmonic (e) 21st harmonic (f) 23rd harmonic

(g) 25th harmonic (h) 27th harmonic (i) 29th harmonic

Figure 4.16: *Intensity profiles of the harmonics at the exit of the capillary. The colour scale shows intensity with the same scale across all the images. Parameters are the same as those in figure 4.10.*

region and Fraunhofer diffraction theory [41] is used in the far field region. Each of these methods is briefly described below, followed by a description of the way in which they are employed here and a discussion of the propagation properties of the XUV beams.

Angular spectrum method

The angular spectrum method is based on the decomposition of an electric field profile into plane waves, each propagating at a known angle to the optical axis of the beam. In 1D or 2D Cartesian coordinates this decomposition is achieved using Fourier transforms:

$$\tilde{E}(k_x, k_y) = \mathcal{F}\{E(x, y)\}, \tag{4.5}$$

where $\tilde{E}$ is the angular spectrum of the field profile $E(x, y)$ and $\mathcal{F}$ is the Fourier transform operator. This angular spectrum can then be propagated as a set of plane waves. The phase advance of a plane wave over a distance z is given by $\exp(ik_z z)$ where $k_z = \sqrt{(k^2 - (k_x^2 + k_y^2)}$ is the component of the wavevector $k = 2\pi/\lambda$ in the z direction. Thus for propagation in linear, homogeneous media, the propagation of a field profile $E(0, x, y)$ to an arbitrary position z may be carried out as a single step

$$E(z, x, y) = \mathcal{F}^{-1}\left\{\mathcal{F}\{E(0, x, y)\} \times \exp\left(iz\sqrt{k^2 - \left(k_x^2 + k_y^2\right)}\right)\right\}, \tag{4.6}$$

where $\mathcal{F}^{-1}$ is the inverse Fourier transform operator.

This method is applicable to any monochromatic field profile, without restriction to specific ranges of z, angle or initial field profile, provided that the Fourier transform of the profile can be calculated at both the initial plane and the required z plane. For realistic beams, these Fourier transforms must be performed numerically, and the computational resources required to sample a sufficiently large plane can quickly become restrictive. For a discrete Fourier transform to be fully accurate, it is required that:

1. the spacing between points in the x and y grids (Δx, Δy) must be less than

half the wavelength of the light being modelled; and

2. the space enclosed by the grid must be such that negligible amounts of field are propagated to regions outside the modelled area, as these fields will be artificially reflected from the boundaries, and cause interference with the propagated waves.

For the simple, single-step implementation described above, it is also necessary that the modelled input and output planes are the same physical size. These restrictions limit the numerical application of this single-step process to systems where the field profiles are of similar sizes in the two planes, and the physical size of the beam is small. Here the beam width is defined as $W = 2\sigma$, where σ is the intensity second moment beam width [123]. For a Gaussian beam, W corresponds to the standard measure of half width at $1/e^2$ intensity. For this method to work, it is required that

$$6W \lesssim N\frac{\lambda}{2}, \tag{4.7}$$

where N is the number of data points used in each dimension of the simulation. This requirement means that for a 2-dimensional (x and y) model, the memory requirements rapidly become larger than are available on a typical desktop computer.[7] To reduce the computational resources required, the radial symmetry of the problem can be exploited. For a field profile of the form $E(r)$, a Hankel transform is used to obtain the angular spectrum $\tilde{E}(k_r) = \mathcal{H}\{E(r)\}$, where $\mathcal{H}$ is the Hankel transform operator [132]. The Hankel transform is defined as

$$\tilde{f}(k_r) = \mathcal{H}\big\{f(r)\big\} = 2\pi \int f(r) \times J_0(2\pi r k_r)\, r \,\mathrm{d}r. \tag{4.8}$$

The method of Guizar-Sicairos and Gutiérrez-Vega [133] is used here, with an implementation by Wyatt [134]. This allows propagation of the beam using ASM in

[7] In Matlab 7.4, a complex number requires 16 bytes of storage. For a beam with $\lambda = 780$ nm and $w = 1$ mm, 15 385 data points are required in each dimension. This requires ~ 3.8 GB of memory.

a manner analogous to the 2D Cartesian case:

$$E(z,r) = \mathcal{H}^{-1}\Big\{\mathcal{H}\big\{E\,(0,r)\,\big\} \times \exp\left(iz\sqrt{k^2-k_r^2}\right)\Big\}. \tag{4.9}$$

This operation, as it is 1-dimensional, is far more efficient in both memory and processing time than the 2D version. However, for propagation over long distances in z, even more efficiency can be achieved using Fraunhofer diffraction theory as described below.

Fraunhofer diffraction

Fraunhofer diffraction theory [41] states that for any initial field profile $E(x,y)$, after propagation over a sufficiently long distance z, the observed intensity pattern ceases to vary except for a scaling with propagation distance. This diffraction pattern is given (in 2D) by the Fourier transform of the field profile at $z = 0$:

$$E(z,x',y') = \mathcal{F}\{E(0,x,y)\}, \tag{4.10}$$

where x' and y' are the coordinates in the observation plane. Again, for a radially symmetric system, the Fourier transform may be replaced by a Hankel transform:

$$E(z,r') = \mathcal{H}\{E(0,r)\}, \tag{4.11}$$

where r' is calculated from the radial component of the wavevector k_r by

$$r' = z\tan(\theta) \qquad \text{and} \qquad \cos(\theta) = \frac{\sqrt{k^2-k_r^2}}{k}. \tag{4.12}$$

The values of z for which the Fraunhofer diffraction regime is valid is commonly defined in terms of the Fresnel number F. For an aperture of radius a illuminated by light of wavelength λ, this is defined as

$$F = \frac{a^2}{\lambda z}, \tag{4.13}$$

with Fraunhofer diffraction being a valid approximation in the regime where $F \ll 1$. In the case of a beam in free space, there is no aperture, so the characteristic size used is W, the beam radius as defined above. By comparison of the predictions of Fraunhofer diffraction with those of the ASM above, it is found that Fraunhofer diffraction becomes a good approximation for $F < 0.1$. That is, the Fraunhofer diffraction approximation is valid for

$$z > \frac{w^2}{F\lambda} \qquad \text{where} \quad F = 0.1. \tag{4.14}$$

Beam propagation results

To investigate the properties of the XUV beam, the predicted beam is propagated in free space and the divergence measured. Since each harmonic beam has a different wavelength, each beam is propagated individually using the ASM method with the theoretically predicted field profiles and phases. The input phase profile is taken from the semi-classical model, as described in section 4.4.1, and the amplitude is taken from the phasematching calculations (section 4.4.2) assuming that the phasematching applies no phase structure to the beam. This field is sampled onto a discrete grid in radius with 6000 points extending from 0 to 1500 μm. This large r grid is needed to get both fine enough sampling to adequately model the structure in the beam and to prevent numerical reflections from the grid boundary during propagation. The beam is then propagated directly to 101 points $0 \leq z \leq 20$ mm. Since the propagation is linear, numerical propagation does not have to be done in a series of steps.

These separate harmonic beams are then incoherently summed to produce a total intensity profile. For visualisation purposes, the intensity profile is in interpolated onto a 400 point grid in z; the radial grid is unchanged. This intensity profile is plotted in figure 4.17. The beam shows considerable structure in the first 10 mm from the capillary exit, before the beam settles down to a steadily diverging beam. The converging phase profile of harmonics above the 17th produces an effective focus

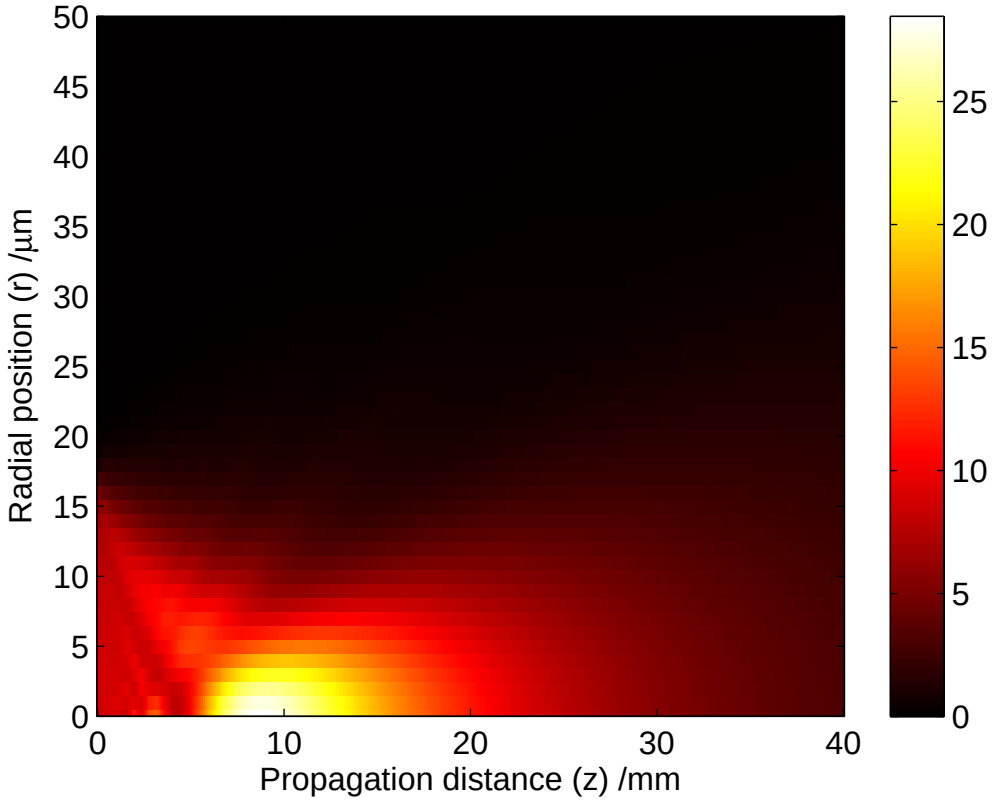

Figure 4.17: *Intensity of the combined harmonic beam as a function of radius and propagation distance from the capillary exit. Colour is intensity in arbitrary units.*

around 8 mm from the capillary exit.

One use of this beam propagation modelling is in predicting the spatial quality of the beam emitted from the capillary. A simple way of doing this is to investigate the evolution of the beam width W as a function of propagation distance. For a monochromatic beam of any intensity profile, the second moment width has been rigorously shown to propagate as [123]

$$W^2 = W_0^2 + M^4 \left(\frac{\lambda}{\pi W_0}\right)^2 (z - z_0), \tag{4.15}$$

where W_0 is the beam width at the waist position z_0 and $M \geq 1$ is a numerical factor that describes how close the beam is to a perfect TEM_{00} Gaussian beam. Figure 4.18 shows the width of the combined beam as a function of z in the two

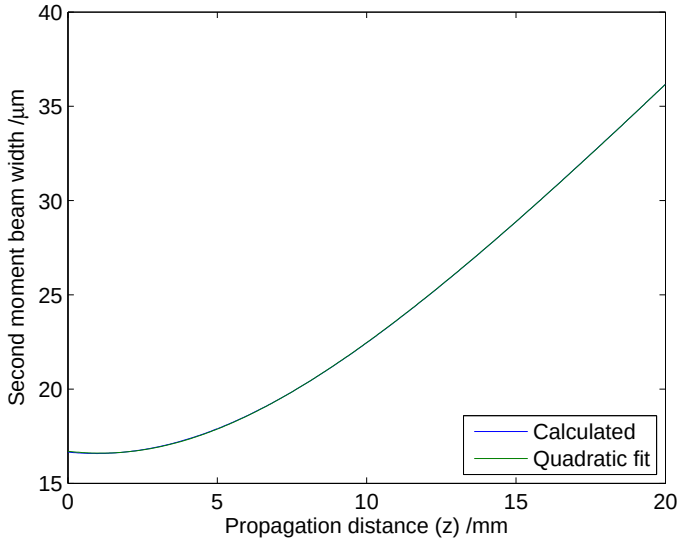

(a)

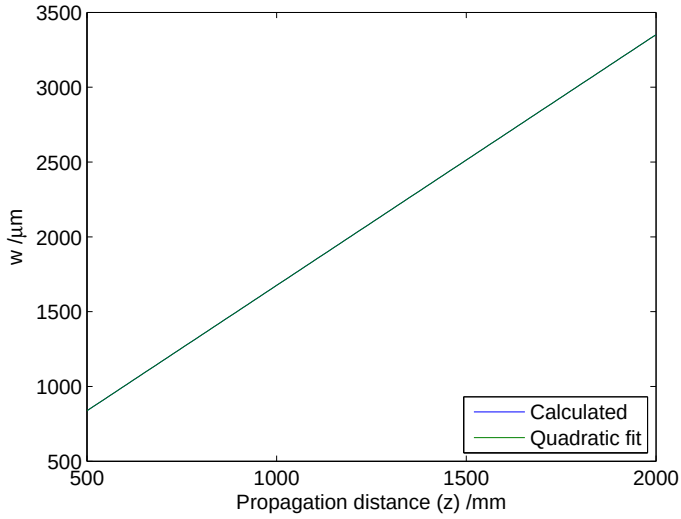

(b)

Figure 4.18: *Beam width W of the combined harmonic beam as a function of z (blue line) and a fit of the form of equation (4.16) (green line) (a) in the near field region using the ASM for propagation and (b) in the far field using Fraunhofer diffraction.*

propagation regimes, ASM in the near field, and Fraunhofer diffraction in the far field. In both cases an excellent fit is found to an equation of the form

$$W^2 = W_0^2 + \Upsilon(z - z_0). \tag{4.16}$$

However, in this case, Υ cannot be interpreted as $M^4 \left(\lambda/\pi W_0\right)^2$, as would be the case for a monochromatic beam, because here the beam is highly polychromatic, and so λ cannot be well defined. However, the fitting to equation (4.16) does allow a prediction of the XUV beam divergence. The divergence half-angle Θ is given by

$$\Theta = \tan^{-1}\left(\sqrt{\Upsilon}\right). \tag{4.17}$$

This gives a divergence half-angle of 1.70 mrad from the fit to the near field predictions and 1.68 mrad from the fit to the far field data. The consistency of these values is an indicator of low numerical errors in the propagation procedures.

While no well characterised experimental measurements of the XUV spatial profile as a function of distance have yet been taken, the values above agree with the estimated values taken from preliminary measurements. To compare this to experiment, measurements of the beam profile as a function of z need to be taken. In the far field regime, as necessary to measure the divergence of the beam, these are relatively straightforward. However, it is difficult to take measurements in the near field of the capillary due to the very high intensity fundamental that is propagating collinearly with the XUV. In order to separate these beams, a 200 nm aluminium foil is used, but this cannot be placed too close to the capillary as the fundamental beam can burn a hole in it. By the time the fundamental has diverged sufficiently to be filtered by the foil, the XUV beam has reached the far field.

An experiment has been done to refocus the XUV beam using an off-axis, spherical, multilayer mirror. In principle this optical system can be modelled using the above techniques: Fraunhofer diffraction from the capillary to the mirror and ASM from the mirror to the focus. The problem with this method is that the off-axis

mirror imposes a non-radially-symmetric phase profile on the beam, so the ASM must be done in two dimensions. A 2D grid that covers the whole beam (~ 3 mm radius) at the mirror has poor resolution at the focus: for an array with 4096 points in each dimension, the spatial resolution is only 1.5 μm. This also leads to poor resolution in angular space; the ratio of Δx to $\lambda/2$, which should be less than 1 for accurate modelling, is ~ 93. This leads to large inaccuracies in any propagation code for beams containing high spatial frequencies. Further work is needed to determine if the process can be made computationally tractable, and exactly what resolutions are required for acceptable errors.

4.5 Further work

This section considers various extensions to the phasematching model to improve its accuracy and range of validity.

4.5.1 Pressure gradients

The model presented in chapter 3 assumes a constant pressure when calculating the harmonic build-up; in the derivation of equation (3.23) it was assumed that that k_f, k_q and α_q are constant. To remove this assumption, the build-up equation must be derived with k_f, k_q and α_q as functions of propagation distance z. This gives, in the most general form

$$I(r,t,q) \propto \left\{ \int_0^L \sqrt{\mathrm{d}N(r,t,z)}\, \exp\left[-i \left(\int_0^z q k_f\left(z'\right) \mathrm{d}z' + \int_z^L k_q\left(z'\right) \mathrm{d}z' \right) \right] \right. \\ \left. \times \exp\left[- \int_z^L \alpha_q\left(z'\right) \mathrm{d}z' \right] \mathrm{d}z \right\}^2 . \quad (4.18)$$

This equation is valid for any form of pressure profile and can be calculated numerically. However, it quickly becomes computationally time consuming as it requires a double integral over z for each value of r, t and q. For the experiments considered here, the pressure profiles, as discussed in section 2.5, are confined to

linear gradients in z. For the case of a linear gradient, the inner integrals may be solved exactly using the trapezium rule, giving the formula

$$I(r,t,q) \propto \left\{ \int_0^L \sqrt{\mathrm{d}N(r,t,z)} \times \exp\left[-i \left(\left(\frac{k_f(0)+k_f(z)}{2} \right) z + \left(\frac{k_q(z)+k_q(L)}{2} \right) (L-z) \right) \right] \times \exp\left[-\left(\frac{\alpha_q(z)+\alpha_q(L)}{2} \right) (L-z) \right] \mathrm{d}z \right\}^2 . \quad (4.19)$$

This equation can be evaluated with a single integral over z, and so is numerically feasible. Implementing this calculation removes the assumption of constant pressure from the phasematching calculations. As the currently used capillaries have a pressure gradient over a length much greater than the build-up length (section 2.5), this assumption is probably the most significant error in the phasematching calculations. Therefore implementing this could provide a significantly more accurate prediction of the XUV generation from a real capillary.

4.5.2 Time dependence of emitted energy

In the calculations presented in chapter 3 it is assumed that every harmonic is equally likely to be emitted at any given point in time. However, in section 2.1 it was seen that an electron tunnelling at a given time has a well defined energy on its return to the ion, and will therefore emit a photon with a known energy. Therefore, one extension of the phasematching model would be to include this effect. Instead of a build-up of the form of equation (3.23)

$$I(r,t,q) \propto \mathrm{d}N(r,t) \times f\left(\Delta k, \alpha, L\right) \quad (4.20)$$

an equation of the form

$$I(r,t,q) \propto \delta_K\left(q, q_{\mathrm{sc}}(t)\right) \times \mathrm{d}N(r,t) \times f\left(\Delta k, \alpha, L\right) \quad (4.21)$$

would be used. Here δ_K is the Kronecker delta function and $q_{\mathrm{sc}}(t)$ is the harmonic number emitted at time t. This is calculated from the semi-classical model by evaluating the energy of a photon returning at time t, and converting this energy to a harmonic number. The relationship between tunnelling time and energy is plotted in figure 2.2(b).

This relaxes the assumption, made in deriving the original model, that all energies up to the cutoff energy are equally likely to be emitted at any given time. It is, however, unclear whether this effect is significant, and further work should be done to determine the magnitude of this effect before significant time is spent implementing this extension.

4.5.3 Energy dependent recombination probability

Another improvement that could be made is to relax the assumption that all energies are equally likely to be emitted. The cross section for recombination of the electron with its parent is, in fact, energy dependent [9, 12]. This can done by including an energy dependent recombination factor in the build-up equation, either separately from, or combined with the modification suggested in the previous section. The factor used could either be calculated from quantum mechanical simulations of the atom, or derived from published tables of factors, such as electron impact ionisation cross sections.

Compared to factors such as pressure gradients (section 4.5.1) however, this is probably a small effect and may well be negligible compared to the errors introduced to the model by inaccurate values of gas absorption (see section 2.6) or ionisation properties.

4.5.4 Use of XUV time profiles

One output from the phasematching calculation is the time profile of the XUV output as shown in figure 3.11(a), and reproduced in figure 4.19 for convenience. It is seen that there are a distinct number of optical cycles of the fundamental over

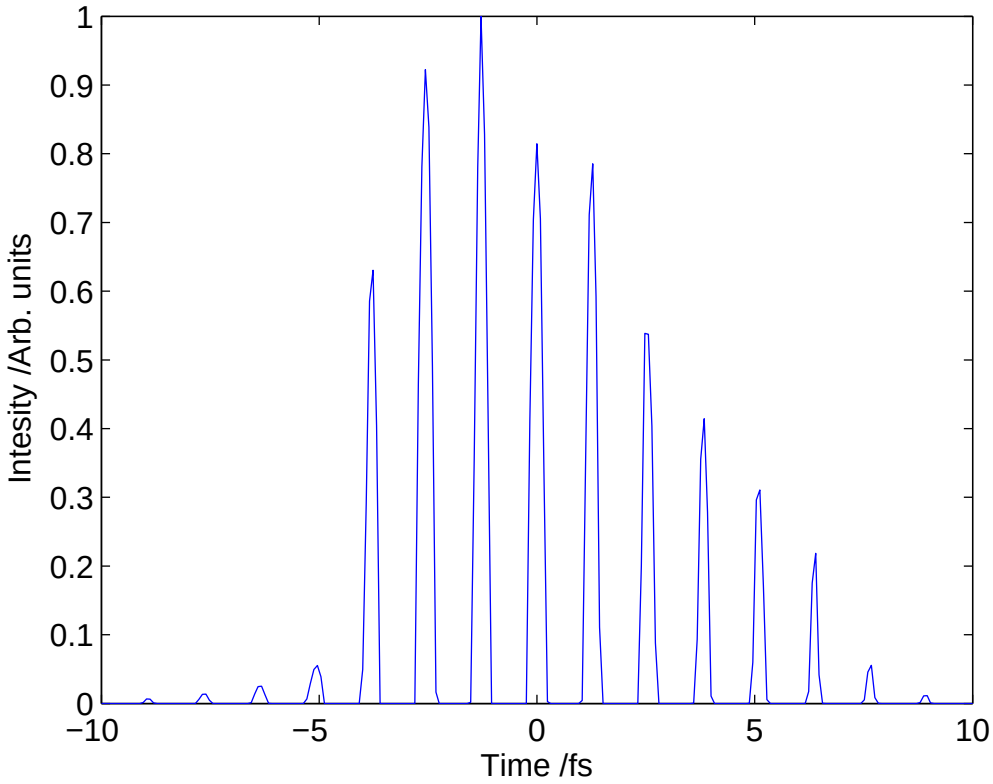

Figure 4.19: *XUV intensity as a function of time, as predicted by the phasematching model. Conditions are the same as figure 3.5.*

which the generation occurs. Since the harmonic structure of the beam is caused by interference between the XUV bursts generated at each half cycle of the laser, a change in the number of cycles used for generation should be visible as a change in the spectral width of the observed harmonics. From consideration of the Fourier transform relationship between the time profile and the spectrum, a reduction in the number of XUV bursts contributing to the spectrum should cause an increase in the bandwidth of each harmonic, and vice versa. In the limit that a single attosecond XUV pulse is generated, the harmonics merge into a continuum [30].

Investigation of the bandwidth of the generated XUV harmonics can therefore be used as a further validation of the phasematching model. If a quantitative relationship can be established between harmonic bandwidth and the number of attosecond bursts, then simple spectral measurements can be used to determine, to a reasonable accuracy, the number of bursts in an XUV attosecond pulse train. This would not fully determine the temporal shape of the XUV pulses, as the structure of each burst and the exact pulse train envelope would remain unknown. However, an estimate of the number of pulses in the attosecond train would still be useful in the design of experiments that use the XUV source to investigate matter, particularly those with a strong time dependence.

4.5.5 Non-Gaussian laser pulses

Another assumption used in this model is that the laser pulse is Gaussian in time. While this assumption may be appropriate for the powers and pressures used in these experiments, simulation has shown (see chapter 5 for details) that at only slightly higher pressures and intensities, the temporal profile of the pulse can be modified by propagation through the plasma. It is not yet known how large an effect modification of the temporal profile of the pulse has upon generation, but given that the time at which phasematching occurs is so strongly dependent on the ionisation caused at the leading edge of the pulse, and that the generation process is highly nonlinear, it is likely that the temporal shape of at least the leading edge

of the laser pulse is important.

The combination of a propagation model with this phasematching model could, therefore, provide a better understanding of the generation process and thus give greater control of the generated XUV pulses. Section 5.9.2 discusses the potential development of this compound model further.

4.6 Conclusions

The model of phasematching presented in chapter 3 has been compared to experiment and shows good agreement with the experimentally measured spectra for a range of gases. This implies that, as expected, phasematching effects are crucial in determining the spectrum of emission from a capillary HHG source, as good agreement can be achieved by considering only the simplest single atom response, that of a plateau with a hard cutoff at the semi-classical cutoff energy $E_{\max} = I_p + 3.17\,U_p$.

The model has also been compared with gas mixtures, where it shows qualitative agreement with experiment; the cutoff energy is increased by the introduction of a non-ionising buffer gas. However, the magnitude of the increase is not as great in experiment as predicted in the theory, which may be due to errors in the ionisation properties or refractive index properties of the gases used.

A further use of the propagation model in predicting the spatial properties of the output XUV beam, and therefore its propagation characteristics, has also been demonstrated. Experiments to test the propagation have been proposed, and the computational limitations of the method have been explored.

Finally, a number extensions to improve the accuracy and range of validity of the phasematching model have been discussed, together with a proposal to use the phasematching model to gain an understanding of the temporal profile of the emitted XUV beam. The most useful of these would be the extension of the phasematching model to pressure gradients, as that would allow a more realistic modelling of the experimental situation. The use of a non-Gaussian laser pulse for phasematching is also useful, and would be easy to implement, as the input laser pulse is already

treated numerically. The other suggestions, while sensible, would provide only slight increases in accuracy which may be swamped by other, neglected, effects such as the single atom response.

Chapter 5

Development of a modal propagation model

The use of a capillary waveguide for HHG provides an additional level of control over the generation process, as well as extending the interaction length over which harmonics may be generated. However, the relatively long length of capillary means that the fundamental laser pulse propagates for a significant distance in an ionising gas. Significant fractions of the gas are ionised by the passage of the pump laser, and the optical properties of the created plasma significantly affect the propagation of the laser pulse, leading to reshaping of the pulse in space, time and spectrum. In particular, as capillary waveguides are inherently multimode, spatially and temporally varying ionisation can create mode mixing. An understanding of these effects is necessary to understand the harmonic generation occurring in the capillary. It is also necessary to know the amount of ionisation at a given position in the capillary, as this affects the phasematching conditions and generation efficiency.

This chapter is structured as follows: section 5.1 discusses the published models of propagation in ionising gases and section 5.2 gives an overview of the modal propagation model, before detailed discussion in the following sections. Section 5.3 describes the input beam definition, the method of calculating the coupling and the determination of the modes to be propagated at the input face of the capillary.

It also discusses the effect of input beam misalignments on the coupling, and the level of radial asymmetry present for a given misalignment. Section 5.4 covers the propagation of this initial field in the capillary, the calculation of ionisation and the spatial reshaping of the beam. The beating of capillary modes is discussed in section 5.6. Section 5.7 presents a comparison of the model output with experimental data. Section 5.8 considers the uses and limitations of the model as presented and section 5.9 contains ideas for developments and future work. Section 5.10 concludes the chapter.

5.1 Prior work

While there have been a number of studies on the propagation of pulses in gas-filled waveguides (see, for example, [78, 135, 136]), these have generally been limited to intensities below the ionisation threshold. Other studies of pulses in ionising gases (for example [137–139]) allow the beams to propagate in free space, and do not include guiding effects. The work on waveguides filled with ionising gas is more limited. Rae and Burnett [140] describe a 1-dimensional model which produced some of the effects observed in experiments, but also showed that spatial effects could play a large role, and that higher dimensional models were needed. This conclusion was also shown by Babin *et al.* [141], in which a 1-dimensional model was used to successfully predict the observed spectral broadening. The broadening in [141] was suggested as a means of pulse compression, similar to that occurring via self phase modulation in gases below the ionising limit [121].

Tempea and Brabec [142] developed a 3-dimensional model of pulse propagation in ionising gases to investigate this broadening further, and Courtois *et al.* [79] further developed the model to include the properties of the plasma created by the laser. A similar model by Christov [109] has been used to investigate [130] pulse compression mechanisms in low-pressure, gas-filled waveguides, that do not require subsequent dispersion compensation. These mechanisms are inherently 3-dimensional and cannot be explained by 1-dimensional nonlinear effects [130]. The

models of Tempea and Brabec [142], Courtois *et al.* [79], Christov [109] and also Andreev *et al.* [143] are all essentially similar, and involve the solution of coupled differential equations for the time-dependent amplitudes of each of the capillary modes. They also calculate the ionisation fraction either using a quasi-static ADK type model (as in [79, 142, 143]), or via solution of the Schrödinger equation for the outer electron [109]. These simulations are very computer intensive and, as a consequence, are limited in the number of capillary modes that are simulated: 2 modes in the case of [142] and 3 modes in [79].

The models above are powerful in predicting the effects of propagation on the spectral and temporal profile of a laser pulse through a waveguide; however, they are computationally intensive and therefore take a long time to run and are limited in the number of modes that can be modelled. In the present experiment, we are interested in modelling the power losses and the fluorescence that is observed from the side of the capillary as a diagnostic for the HHG experiments. As HHG can only occur when the generating medium is ionised, it is desirable to know at exactly which points in the capillary ionisation occurs, to optimise the capillary design. For this purpose, the exact spectral and temporal profiles of the pulse are not of interest in the first instance, provided that the time profile is not significantly distorted. At experimental peak intensities of $\lesssim 3 \times 10^{14}$ W cm^{-2}, as used in these experiments,[1] the literature [140, 141] has shown ionisation to have a small effect on the temporal profile. For this reason, a simple modal model, assuming a constant temporal pulse profile, should be sufficient to predict power losses and local ionisation fractions within the capillary.

5.2 Outline of the model

This chapter presents a theoretical model of the effect of laser induced ionisation on a pulse propagating through a gas-filled capillary waveguide. This model takes

[1] Since this model was developed, the laser system has been upgraded, allowing access to higher intensities. For these intensities, the model described in section 5.9 may be more appropriate.

account of spatially dependent depletion of the laser field due to ionisation, leading to changes in modal distribution with propagation. A comparison with experimental results demonstrates that the model predicts correctly both the observed energy loss from propagation and the plasma fluorescence from the capillary. The model and experiment also both reproduce the mode beating patterns previously observed [60,61]. This model allows us to investigate the effect of wavefront tilt and curvature, such as that caused by experimental misalignment of the capillary relative to the input beam.

To model the capillary, the input is taken to be a linearly polarised Gaussian beam with arbitrary size, position and wavefront tilt. The coupling of the input beam to each capillary mode is then calculated to give the amplitude and phase of each excited capillary mode. These modes are individually propagated for a short distance in the axial direction and then recombined. The combined intensity profile is used to calculate the ionisation fraction at each capillary radius. The energy lost from the laser beam is then calculated as a function of radial position, the lost energy is subtracted from the pulse, and the electric field is recalculated. This field profile is then decomposed into capillary modes and the process repeated. This process is summarised in figure 5.1. Although it treats slightly different effects, this model is similar, in principle, to a split step beam propagation model [144] as the nonlinearity, instead of being a continuous process, is evaluated at the centre of each propagation step.

As described above, the effect of the ionisation on the spatial and temporal profiles at the experimental intensities is small. This implies that self phase modulation of the pulse due to the plasma is not a significant effect and as such, the phase changes induced by the plasma can be neglected in the current work. A more sophisticated model, including these phase effects is desirable (see section 5.9), but including temporal effects would mean that the model could not be used in the way that was intended (for investigating the effect of coupling on ionisation) without considerably increased computer resources.

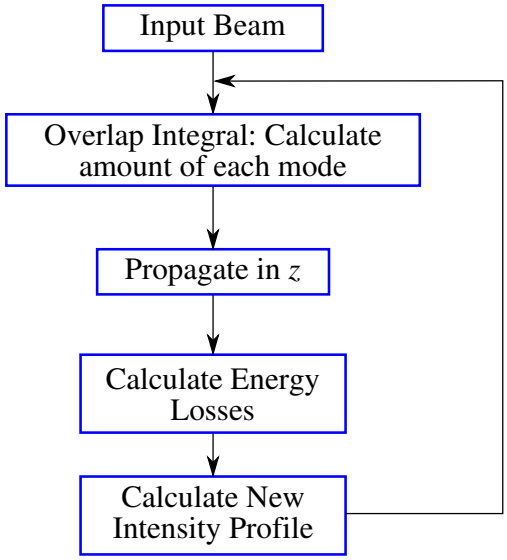

Figure 5.1: *Schematic of the algorithm used in the modal propagation model.*

5.3 Excitation of capillary modes

In section 2.3 the mode profiles and propagation constants for all linearly polarised capillary modes were determined. Using these, any arbitrary combination of modes may be propagated along a length of hollow capillary. However, it is first necessary to determine the (complex) coefficients of each mode as excited by some electric field profile incident on the capillary entrance.

The coupling coefficient of each capillary mode is determined by calculating the overlap integral of the laser profile and the relevant mode. This integral is evaluated by multiplying the laser profile by the (suitably normalised) mode profile and integrating over all space. For a linearly polarised laser, only linearly polarised modes will be excited, so the problem can be reduced to a scalar form. This assumes that the focusing is weak, such that the axial components of the electric field can be neglected.

The radially symmetric modes of the capillary are considered here, the EH_{1m}

modes, but the treatment of the composite modes is identical. The capillary mode profiles are, as defined in equation (2.15),

$$E_{1m} = J_0\left(u_{1m}\frac{r}{a}\right) \tag{5.1}$$

for the EH_{1m} modes. These modes are, by definition, orthogonal; that is

$$\int_S E_{1p} \times E_{1q}\,\mathrm{d}S \quad \begin{cases} = 0 & \text{if } p \neq q \\ \neq 0 & \text{if } p = q, \end{cases} \tag{5.2}$$

where $\int_S \ldots\ \mathrm{d}S$ is the integral over the plane of the capillary entrance. In polar coordinates, $\int_S \ldots\ \mathrm{d}S$ becomes $\int_0^\infty \int_0^{2\pi} \ldots\ r\,\mathrm{d}r\,\mathrm{d}\theta$.

If normalised modes E'_{1m} are defined as

$$E'_{1m} = \frac{E_{1m}}{\int_S |E_{1m}|^2\ \mathrm{d}S}, \tag{5.3}$$

then E'_{1m} form an orthonormal set and

$$\int_S E'_{1p} \times E'_{1q}\,\mathrm{d}S \quad \begin{cases} = 0 & \text{if } p \neq q \\ = 1 & \text{if } p = q. \end{cases} \tag{5.4}$$

The input laser electric field profile is denoted here by $E_i(r, \theta)$ and the field coupling coefficient C_m is given by

$$C_m = \int_S E'_{1m} \times E_i\,\mathrm{d}S. \tag{5.5}$$

If the input electric field is complex (i.e. it has a phase variation across the beam), then the mode coefficients are also complex. The arguments of these complex coefficients C_m give the relative phases of each of the coupled modes.

These coefficients can be used to reconstruct the field from the mode profiles in

the inverse operation

$$E_i = \sum_m C_m E'_{1m}. \tag{5.6}$$

Here it is important to be clear about the meaning of the coefficients in question, as there are four possible numbers of interest: the field coupling coefficient, denoted here by C_m and described above; the field coupling efficiency $\bar{C}_m$, which is a measure of the proportion of the electric field that is distributed into each mode; the energy coupling coefficient ξ_m, which describes the total energy in each mode; and the energy coupling efficiency $\bar{\xi}_m$, which is the fraction of the input energy that is transferred to each mode. These are related by

$$\begin{aligned} \xi_m &= |C_m|^2 & \bar{\xi}_m &= \frac{\xi_m}{\int\limits_S |E_i|^2 \ \mathrm{d}S} \\ \bar{\xi}_m &= \left|\bar{C}_m\right|^2 & \bar{C}_m &= \frac{C_m}{\sqrt{\int\limits_S |E_i|^2 \ \mathrm{d}S}}. \end{aligned}$$

5.3.1 Effect of spot size on coupling

For the case of a linearly polarised Gaussian beam focused to a spot size of w centred on the capillary entrance, the electric field of the laser is given by

$$E = E_0 \exp\left(\frac{-r^2}{w^2}\right). \tag{5.7}$$

The coupling of this perfectly aligned beam into the capillary is parameterised by the single number w/a, the ratio of the spot size to capillary radius. This scenario has been studied by Nubling and Harrington [145]. The radial symmetry of the input laser means only the radially-symmetric, linearly-polarised modes of the capillary, the EH_{1m} modes, need be considered. Figure 5.2 shows the energy coupling efficiency $\bar{\xi}_m$ for each mode as a function of the spot size parameter w/a. For this perfectly aligned beam, 98 % of the energy can be coupled into the EH_{11} mode if the beam has a w/a value of 0.64. Since the EH_{11} mode is the lowest loss mode of the capillary (as discussed in section 2.3), a w/a parameter of 0.64 gives the maximum transmission

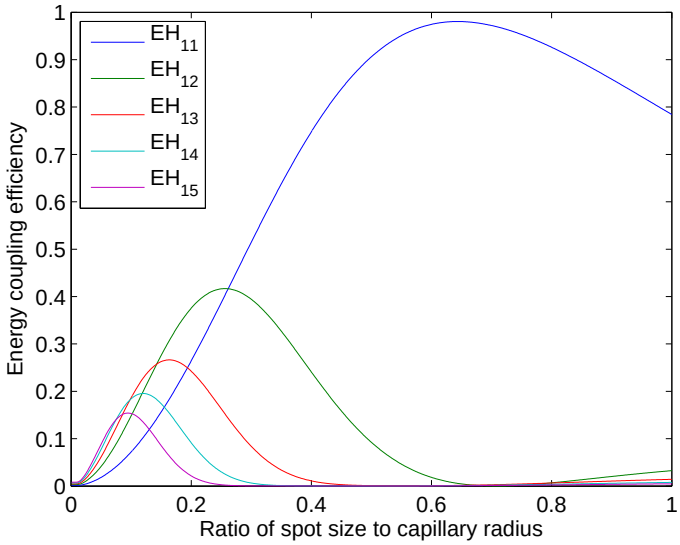

Figure 5.2: *Fraction of energy coupled into each mode ($\bar{\xi}_m$) as a function of the spot size parameter w/a. Each line corresponds to a different capillary mode. Peak coupling into the EH_{11} mode occurs at $w/a = 0.64$.*

through a sufficiently long section of capillary. However, $w/a = 0.64$ is not the point at which the coupling into higher order modes is minimised, and even at the minimum point, it is still impossible to completely eliminate coupling into higher order modes. Thus, for any coupling of a Gaussian beam into a hollow capillary, some energy will be coupled into modes other than the EH_{11}; for a capillary aligned for maximum transmission, ~ 1.1 % of energy is coupled into higher order modes. Since higher order modes attenuate faster, the effect of these modes is lessened with propagation length, but the interference between these modes and the EH_{11} mode must be considered.[2]

5.3.2 Effect of misalignment of the capillary

For the perfectly aligned beam described above, the coupling is easily analysed as the coefficients are a function of only one parameter, the spot size. For the more realistic case of a misaligned beam, there are 6 independent parameters (shown in

[2]A high order mode with only 1 % of the power of the EH_{11} mode will have 10 % of the field strength. This can cause a 33 % peak to peak modulation in the intensity of EH_{11} mode.

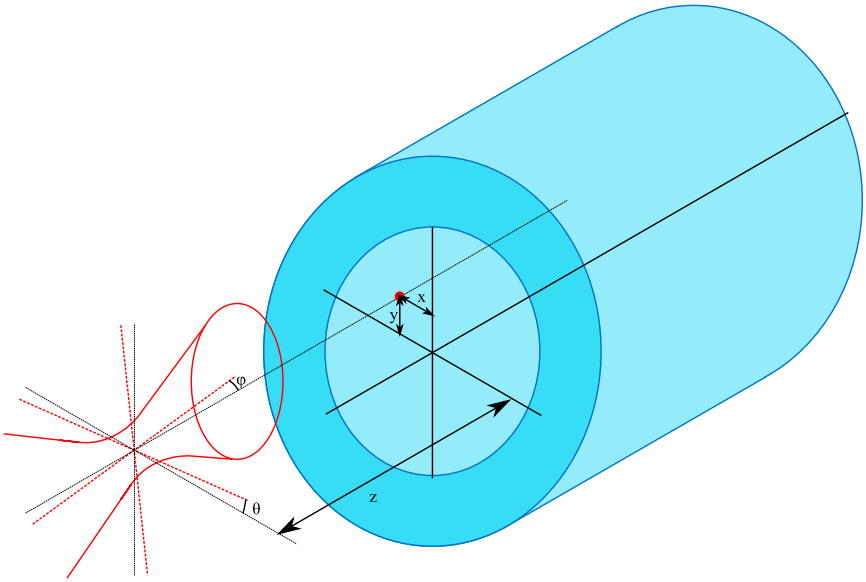

Figure 5.3: *An arbitrarily aligned Gaussian beam incident on a capillary. The focal point may be misaligned in x, y and z, and the beam may be propagating at an arbitrary angle to the z-axis: θ in the plane of the x-axis and φ in the plane of the y-axis.*

figure 5.3): the waist spot size w_0; x_0, y_0 and z_0, the coordinates of the centre of the capillary entrance relative to the beam focal point; and θ and φ, the angles of the beam with respect to the axis of the capillary.

Misalignment in z

For misalignments in the z direction only (that is, with the laser focused slightly in front of or behind the capillary entrance plane) a similar analysis can be carried out to the w/a analysis above. Since the z displacement does not parameterise as neatly, a value for a and w_0 must be set. This analysis uses the experimental capillary size $a = 75$ µm and a perfectly coupled beam at $z_0 = 0$. Therefore $w_0 = 0.64\,a = 48$ µm.

Such a beam propagating in free space is defined mathematically by

$$E_i = E_0 \exp\left(\frac{r^2}{w(z)^2} - i\frac{k}{2R(z)}r^2\right), \tag{5.8}$$

where

$$w(z) = w_0\sqrt{1+\left(\frac{z}{z_R}\right)^2} \tag{5.9a}$$

$$R(z) = z\left[1+\left(\frac{z_R}{z}\right)^2\right] \tag{5.9b}$$

$$z_R = \frac{\pi w_0^2}{\lambda}. \tag{5.9c}$$

Figure 5.4(a) shows how the energy coupling efficiency $\bar{\xi}_m$ varies with z_0. In the case of defocusing however, the coupling is not determined entirely by the efficiency. As the phase of the input beam varies (E_i is complex) the coupling coefficients C_m are also complex, and $\arg(C_m)$ gives the phases of the coupled modes. The variation of these phases with z_0 is shown in figure 5.4(b). As might be expected, the most efficient coupling occurs at $z_0 = 0$ where the phase of the laser is flat and $w = 0.64\,a$. For $z_0 \neq 0$, the coupling efficiency decreases as the beam size w increases. The decrease is not dramatic in the region around $z_0 = 0$, showing that the z position of the focus is not highly critical in determining the efficiency, provided it is correct to within about 5 mm.

The more interesting aspect of these figures is in the phase information shown in figure 5.4(b). This figure shows that sizable adjustments to the phase of the modes can be made by adjusting the position of the capillary in the z direction relative to the focus. The phase difference becomes largest around the Rayleigh range, as that is where the radius of curvature reaches a minimum and hence the curvature of the input is most pronounced. These phase shifts can be used to control the beating pattern observed in the capillary (see section 5.6 below). To obtain a $\frac{\pi}{2}$ rad shift between the EH_{11} and EH_{12} modes, it is necessary to move the capillary by just 4.8 mm. Since the phase shift is in a different direction for positive and negative z

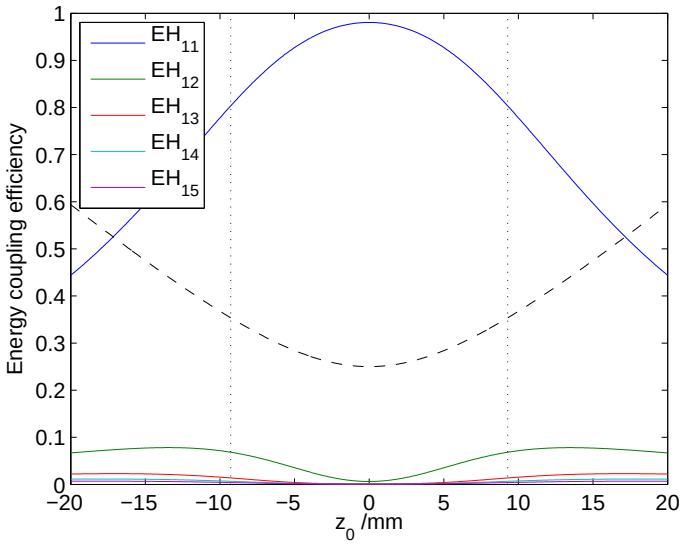

(a) Fraction of energy coupled into each mode ($\bar{\xi}_m$) as a function of z_0. The dashed line shows the width of the input beam w in arbitrary units.

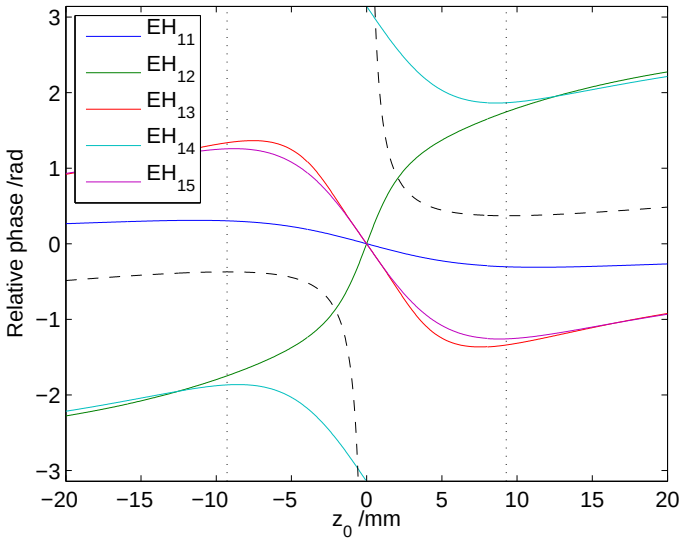

(b) Phase of each mode as a function of z_0. The dashed line shows the radius of curvature of the input Gaussian beam, R, in arbitrary units.

Figure 5.4: *Coupling efficiency and phase of each EH_{1m} mode as a function of z position of the capillary relative to the focus (z_0). Each solid line corresponds to a different mode, and in each figure the Rayleigh range — the points at which $w = \sqrt{2}\,w_0$ — is marked by the dotted lines.*

movement, it is possible to achieve a phase shift of π rad whilst only varying the coupling efficiency from 98 % at $z_0 = 0$ to 93 % at $z_0 = \pm 4.8$ mm.

It might be speculated that, although optimum coupling is at $z_0 = 0$ for $w_0 = 0.64\,a$, for $w_0 < 0.64\,a$ increasing the z offset might improve the coupling (i.e. setting z_0 such that $w(z_0) = 0.64\,a$). Investigation shows that this is not the case, as the increased curvature of the laser wavefronts still reduces the coupling efficiency.

Breaking of radial symmetry

Having investigated the first misalignment parameter, z_0, the remaining four parameters, x_0, y_0, θ and φ, are now considered. The analysis of these is considerably complicated by the fact that if any of these parameters are non-zero, the system is no longer radially symmetric and both the EH_{1m} modes and the composite modes (described in section 2.3.1) must be considered. To model this, the radial symmetry assumption used thus far must be relaxed, and coupling must be investigated as a 2-dimensional, rather than a 1-dimensional, problem. Also, any further modelling of propagation in the capillary must be extended to a 3-dimensional model, rather than the 2-dimensional one that can be used if radial symmetry is assumed.

Another significant problem in investigating this situation is the number of data points that must be sampled to adequately investigate a 6-dimensional space: for a coarse scan of 10 points in each dimension, 1 000 000 points must be sampled; for a more useful scan with 100 points per dimension, 10^{12} points must be calculated.

The following Monte Carlo model is proposed to address these problems and determine the significance of the radial asymmetry in our experimental arrangement. In the case of a hollow capillary with no gas in the core, the losses due to propagation of each mode in the capillary can be determined analytically. Therefore, for any given set of coupling parameters, it is possible to calculate the overall power transmission of the capillary relatively easily. Here the transmission of the capillary is calculated for many different sets of coupling parameters selected at random, and the overall trends are examined. The parameters were selected using a normally distributed

Parameter	**Run 1**		**Run 2**	
	Mean	Std Deviation	Mean	Std Deviation
Spot size parameter $\frac{w_0}{a}$	0.64	0.2	0.64	0.1
x_0 /μm	0	20	0	5
y_0 /μm	0	20	0	5
z_0 /mm	0	3	0	1
Angle θ /°	0	1	0	0.3
Angle φ /°	0	1	0	0.3

Table 5.1: *Mean and standard deviation of each of the coupling parameters used in the Monte Carlo Simulation.*

random number with a given mean and standard deviation (see table 5.1 for a list), and the coupling and capillary transmission were calculated. The capillary used was 7 cm long with a 75 μm radius. The coupling was calculated over a 300 by 300 point Cartesian grid in the entrance plane of the capillary. The first 30 modes (taken from both EH_{1m} and composite modes) were modelled. To obtain a well distributed set of transmissions, two runs of the simulation were performed, each with 10 000 data points, and the results collated. For run 1, the parameter values (as shown in table 5.1) led to a large number of data points with low transmission; for run 2 the data points were clustered towards higher transmissions.

The ratio of power in the EH_{1m} modes to power in the composite modes was calculated for each set of coupling parameters. This ratio of powers is plotted against total transmission in figure 5.5. As the transmission increases, a greater proportion of the energy is found to be in radially symmetric EH_{1m} modes. In the experimental arrangement, typical transmission efficiencies are in the range $70 - 80$ % at optimum alignment with no gas in the capillary. For a transmission of 70 %, the ratio is greater than 35 for all the data points calculated. This means that a negligibly small fraction of the coupled power is found in radially asymmetric modes for the alignments routinely used in our experiments. Radial symmetry may, therefore, be assumed with negligible loss of accuracy.

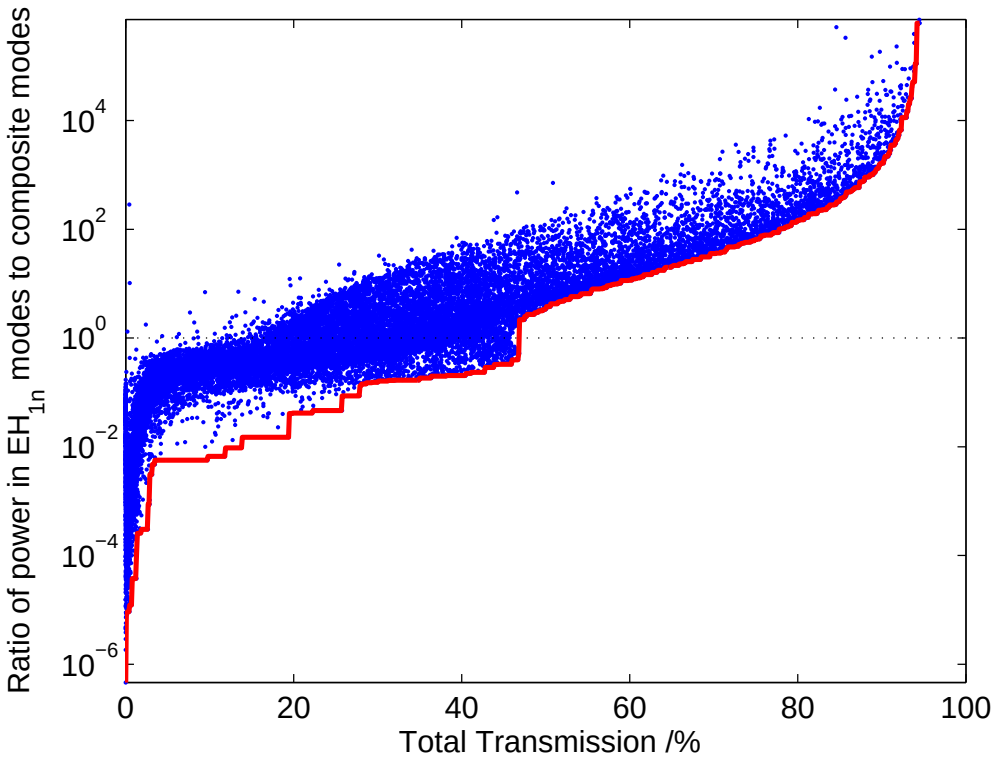

Figure 5.5: *Ratio of power in EH_{1m} modes to power in composite modes for 20 000 random sets of coupling parameters, plotted against total transmission of a* 75 µm *radius,* 7 cm *long capillary. The dotted line is at a ratio of 1:1, and the red line marks the lowest observed ratio for a particular transmission. The ratio is greater than 10:1 for all points with a transmission greater than* 58 %*.*

5.4 Propagation modelling

Once the coupling coefficient of each mode has been found at the start of the capillary, the next step is to propagate the modes along the capillary, taking into account the effects of ionisation. In this model, the pulse shape in time is assumed not to change with propagation.[3] This means that the entire pulse can be described purely by its spatial profile $E(r)$ or, equivalently, by the set of mode coefficients C_m.

A summary of the propagation algorithm is shown in figure 5.1. Once the mode coefficients C_m are determined, each mode can be propagated simply by using the complex propagation constant of the mode γ_m as defined in equation (2.16):

$$C_m\left(z+\Delta z\right) = C_m\left(z\right) \times \exp\left(i\gamma_m \Delta z\right). \tag{5.10}$$

From equation (5.6) we have

$$E(r, z+\Delta z) = \sum_m C_m(z+\Delta z) E_m(r). \tag{5.11}$$

Using these equations it is simple to reconstruct the electric field profile $E(r)$ at a short distance Δz into the capillary. From the electric field, the intensity profile $I(r) = \frac{1}{2} c\epsilon_0 \left|E(r)\right|^2$ can be found.

In principle, to calculate the total ionisation fraction after passage of the pulse, it is necessary to evaluate the ionisation rate $w(r,t)$ for each point in space and time and integrate over the whole pulse in time (*cf.* equation (3.28)). However, given the assumption that the temporal pulse envelope does not change, the ionisation depends only on the peak electric field (or equivalently, peak intensity) at a given radius. The model takes advantage of this fact to dramatically speed up evaluation of the ionisation fraction. The fraction is evaluated for the whole pulse, assuming a Gaussian pulse with a given pulse length, for a set of peak intensities. The model then uses this data as a lookup table to find the ionisation fraction at a given peak

[3] The limitations introduced by this assumption are discussed in section 5.8.

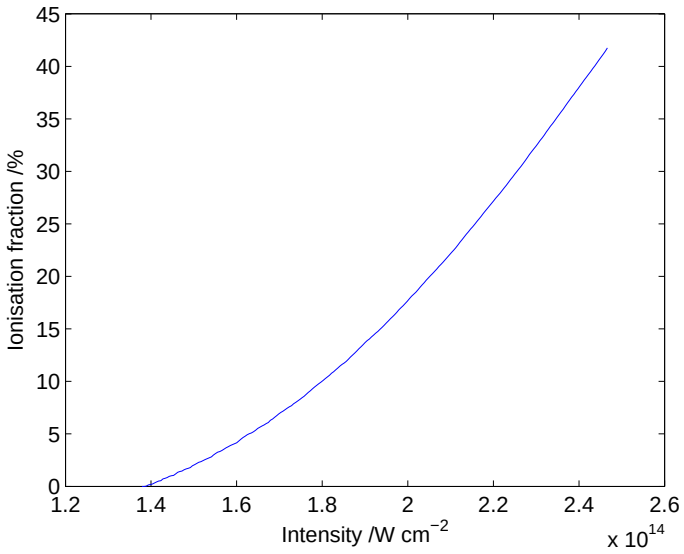

Figure 5.6: *Final ionisation fraction as a function of peak intensity for a* 40 fs *Gaussian pulse. For peak intensities greater than* 2.47×10^{14} W cm^{-2}*, the threshold for BSI is reached, and the gas is completely ionised.*

intensity. A sample lookup table is plotted in figure 5.6 for a 40 fs pulse.

The pulse intensity profile $I(r)$ and ionisation fraction $\eta(r)$ are now known, and it is possible to work out the effect that the ionisation has on the energy of the pulse $\mathcal{E}$. To do this, the known intensity profile must be converted to energy, the energy adjusted for ionisation induced losses and then converted back to give a new intensity profile.

Intensity is defined as energy per second per unit area so, by definition,

$$\mathcal{E} = \iint I(\mathbf{r}, t)\, \mathrm{d}\mathbf{r}\, \mathrm{d}t, \tag{5.12}$$

where $\mathcal{E}$ is the total energy in the laser pulse. In this case, the time profile of the pulse is assumed to be constant and the spatial profile is assumed to be radially symmetric, so

$$I(\mathbf{r}, t) = I(r) \times I(t), \tag{5.13}$$

where $I(r)$ is the peak intensity as a function of radius and $I(t)$ is the temporal

intensity profile. For a Gaussian profile with FWHM τ,

$$I(t) = \exp\left(-\frac{t^2}{\tau_g^2}\right). \tag{5.14}$$

where $\tau_g = \frac{\tau}{2\sqrt{\ln 2}}$ is the Gaussian width corresponding to FWHM τ.

The energy density $\mathcal{E}'(r)$ — energy per unit area — is given by integrating the intensity over time only:

$$\begin{aligned}
\mathcal{E}'(r) &= \int_{-\infty}^{\infty} I(\mathbf{r}, t)\,\mathrm{d}t \\
&= I(r)\int_{-\infty}^{\infty} \exp\left(-\frac{t^2}{\tau_g^2}\right)\,\mathrm{d}t \\
&= \sqrt{\pi\tau_g^2} \times I(r) \\
\mathcal{E}'(r) &= \sqrt{\frac{\pi}{4\ln 2}} \times \tau \times I(r).
\end{aligned} \tag{5.15}$$

From the definition of energy density, the energy $\mathcal{E}(r)$ in a ring of radius r, with thickness Δr, is given by

$$\mathcal{E}(r) = 2\pi r\,\Delta r \times \mathcal{E}'(r). \tag{5.16}$$

Thus the total energy in such a ring at radius r is given by

$$\mathcal{E}(r) = 2\pi\, r\,\Delta r\,\tau\sqrt{\frac{\pi}{4\ln 2}} \times\ I(r). \tag{5.17}$$

As the energy in the laser as a function of radius is now known, it is necessary to determine the loss of energy due to ionisation. Here the loss is assumed to be 1 ionisation potential of the gas involved, I_p, per ionisation event. The loss $\mathcal{E}_{\text{loss}}$ is then simply given by the number of ionisation events N_I multiplied by I_p:

$$\begin{aligned}
\mathcal{E}_{\text{loss}}(r) &= N_I \times I_p \\
&= pN_{\text{atm}} \times 2\pi r\,\Delta r\,\Delta z \times I_p
\end{aligned} \tag{5.18}$$

where p is the pressure of the gas at the relevant position and N_{atm} is the number

density of atoms at atmospheric pressure. The pressure p can vary with z position as is necessary to model the actual capillary system. The pressure profile used in the model is that described in section 2.5.

To calculate the new energy in the ring, $\mathcal{E}_{\text{loss}}(r)$ is subtracted from the original energy $\mathcal{E}(r)$. This energy is then converted back to intensity and then to electric field strength. Since this procedure only yields $|E|$, the original phase values are used, i.e. the ionisation process is assumed not to change the phase of the electric field. The mode coefficients are recalculated using equation (5.5) and the propagation process repeated.

The ionisation mechanism for energy loss causes a reshaping of the beam, as more energy is lost from the centre of the capillary where the ionisation fraction is highest. Therefore, when the mode coefficients are recalculated after loss, energy will have shifted between modes. In general, energy will be shifted from the EH_{11} mode into higher order modes as the intensity profile after ionisation will be flattened. As the beam propagates, these higher order modes attenuate faster than the EH_{11} mode, and so the mode reshaping induces an extra loss in addition to that caused directly by ionisation.

5.5 Numerical implementation and testing

To implement the modal propagation model numerically, the input beam (assumed to be Gaussian, with specified alignment parameters as defined in section 5.3) is sampled on a Cartesian grid in the plane of the capillary entrance with 150 points in each of the x and y directions. The first 30 EH_{1m} capillary modes are sampled on the same grid, and the overlap integral is taken with each mode (equation (5.5)) to find the field coupling efficiency C_m for each mode. Inside the capillary, the calculations are carried out at 300 z points between $z = 0$ and 7 cm. At each z point the summation over modes and loss calculations are carried out on an r grid with 151 points $0 \leq r \leq a$.

To test convergence, the simulation was run with double the number of grid

points (in x, y, z and r seperately) and with double the number of modes modelled. In all cases no significant differences were observed in the higher resolution results. As an example, the total number of ionisation events remained the same to 3 significant figures. If the simulation is run with no gas in the capillary, the numerical propagation code reproduces the analytic predictions of intensity in the capillary as a function of z and r. The results are also stable with respect to small changes in the input physical parameters (alignment parameters and input power). The coupling calculations reproduce those of [145] for the simple case of varying the spot size w.

5.6 Beating of capillary modes

One effect that has been previously predicted [60] and observed [61] elsewhere is the beating of capillary modes. Consider two modes propagating in a capillary, the EH_{11} and EH_{12} modes. As these two modes propagate, they have different propagation constants and the modes develop phase slip relative to each other. This phase slip causes the modes to interfere with each other as they propagate: at point z the two modes add constructively, and at $z+\frac{\zeta}{2}$, where ζ is the distance equivalent to a phase shift of 2π rad, the two modes interfere destructively.

Figure 5.7 shows the difference in intensity profile at the points of complete constructive and destructive interference. The difference is significant, even for an EH_{12} mode with 8 % of the intensity of the EH_{11} mode. Figure 5.8 shows the intensity variation along the capillary for two modes and for only the EH_{11} mode. It can be seen that the peak intensity is actually higher in the case of the two-mode system because — as is seen in figure 5.7 — the intensity profile at the constructive interference point is narrower than that of a pure EH_{11} mode. Also, at the destructive interference point, the intensity profile no longer has a maximum at $r = 0$ and is now a ring, rather than a peak.

For two modes, EH_{1p} and EH_{1q}, the beat length ζ_{pq} can easily be derived by setting

$$\zeta_{pq}\,\Delta\beta_{pq} = 2\pi, \tag{5.19}$$

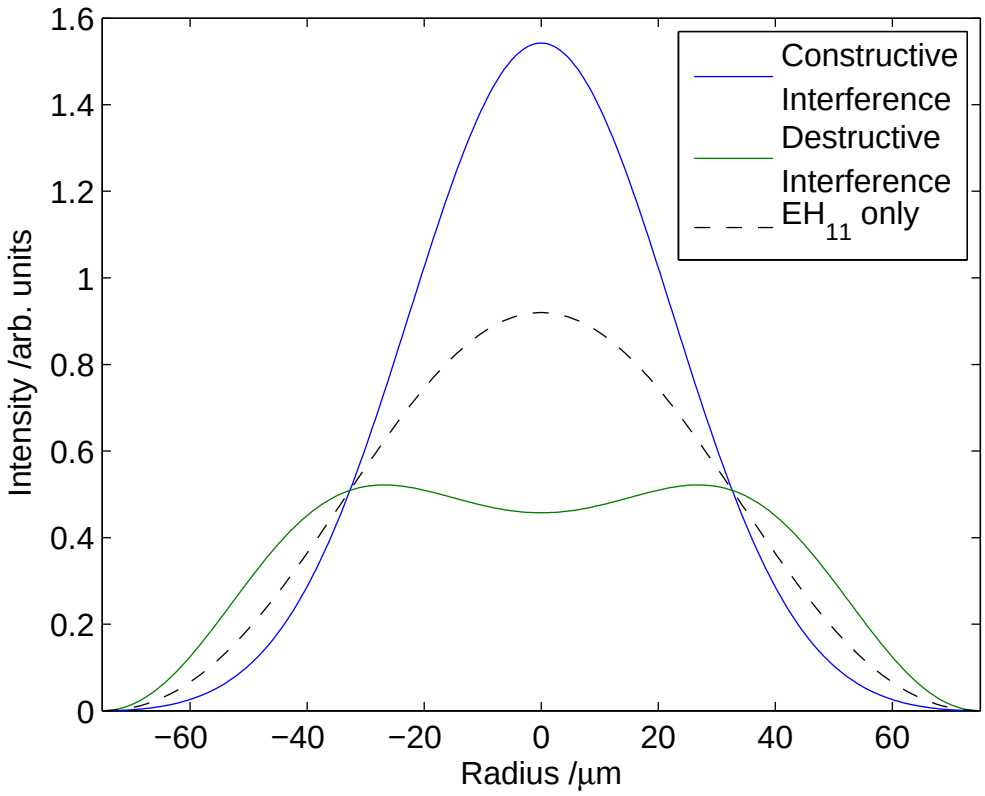

Figure 5.7: *Intensity profiles of constructive and destructive interference of the EH_{11} and EH_{12} modes. The interference is between 92 % power in the EH_{11} mode (shown for comparison) and 8 % power in the EH_{12} mode. The peak intensity is much higher in the constructive interference case than with only the EH_{11} mode.*

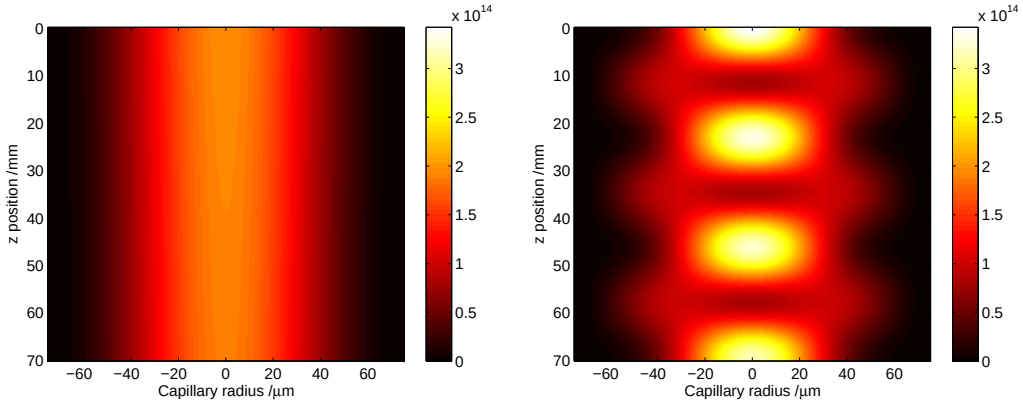

(a) (b)

Figure 5.8: *Peak intensity as a function of length and radius for (a) only the EH_{11} and (b) a mix of EH_{11} and EH_{12} modes. The colour scale used to represent intensity is the same in each case. The total energy in the* 40 fs *pulse at the start of the capillary is* 400 mJ *in each case. In (b)* 92 % *of the energy is in the EH_{11} mode, and* 8 % *is in the EH_{12} mode.*

where $\Delta\beta_{pq} = \beta_{1p} - \beta_{1q}$ and β is defined in equation (2.16a). This gives

$$\zeta_{pq} = \frac{8\pi^2 a^2}{\lambda\left(u_{1q}^2 - u_{1p}^2\right)} \tag{5.20}$$

as given in [60].

The use of this beating for quasi-phasematching has been suggested [146, 147], as the intensity modulation in the driving laser modulates any harmonic generation from the guide. One problem with this scheme is that in order to obtain modulation on a sufficiently small length scale, the beating must be between the EH_{11} mode and high order modes; the shorter the modulation length, the higher order the mode. These high order modes are more lossy, and so tend to decay along the length of the capillary, reducing the beating effect. Also, the group velocity mismatch between modes is sufficient to significantly reduce the overlap in time between pulses in different modes over the capillary length. Dromey *et al.* [147] suggest that the nonlinear mode coupling could be sufficient to repartition energy into higher order modes during propagation, thus overcoming these difficulties, but this repartition is

difficult to control experimentally and so relies on the correct reshaping occurring naturally.

5.7 Comparison of the model to experiment

The experimental data in this section were taken by other members of the group, primarily Chris Froud and Richard Chapman. The theoretical results and analysis are my own.

The propagation model, as described above, has two outputs that can easily be compared to experiment: the output pulse energy and the number of atoms ionised at a given position in the capillary. The output pulse energy can be measured using a power meter to measure the average laser power and dividing by the laser repetition rate. Measurement of the number of ionised atoms was done indirectly by using a CCD camera to record the fluorescence observed though the side of the capillary wall. Figure 5.9 shows a schematic of the arrangement. The number of ions in the capillary is determined from measurement of the intensity of light emitted from the 488 nm emission line in Ar^+. It is assumed that the intensity of emission is proportional to the number of Ar^+ ions in the capillary. This only gives a relative measure of the number of ions at a given point, as the number of emitted photons per ion is not known, but this is sufficient to show the variation of ionisation level in the capillary. Also, the resolution of the imaging is not sufficient to determine emission as a function of radius. This is partially due to the camera resolution and choice of imaging optics, but is also due to the side wall of the capillary itself and the tube in which the capillary is mounted, each of which introduce aberrations in the radial direction.

When comparing the model to experiment, it is necessary to know the input coupling parameters, w_0, x_0, y_0, z_0, θ and φ, as described in section 5.3. For the experimental arrangement, w_0 can be determined by accurate measurements of the beam before focusing and knowledge of the focusing optics, as well as by

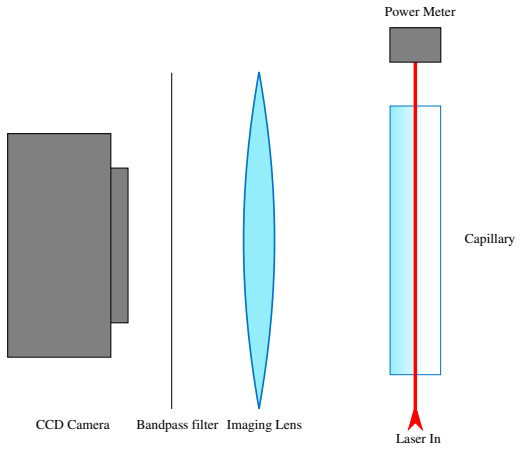

Figure 5.9: *Schematic of the arrangement used for taking measurements of argon ion fluorescence in the capillary for comparison to the modal propagation model. The filter used is a* 488 nm *bandpass filter to isolate emission from the* Ar^+ *ions.*

direct measurement. This parameter can therefore easily be set in the model. The other parameters are harder to measure experimentally. The experimental alignment procedure seeks to minimise all these parameters in order to obtain the best possible coupling — achieved at $x_0 = y_0 = z_0 = \theta = \varphi = 0$. It is likely, however, that perfect alignment is not achieved, as experimental measurements with no gas never reach the theoretically achievable 98 % transmission. This imperfect transmission is seen in various experiments in the literature [79,129,130,141], and is attributed to a variety of plausible causes; for example, pointing instability of the laser [79]; a non-Gaussian input beam [79, 129, 141]; and a slightly elliptical beam [141].

Measurements of the pointing stability indicate that instability is not a significant factor in our experiments. The non-Gaussian and elliptical beam profiles are possibly a contributing factor to the experimental transmissions, but are difficult to quantify. Here, I will investigate the possibility that the reduced transmissions are due to misalignment of the capillary relative to the laser, and use these misalignment parameters to compare my model to experiment.

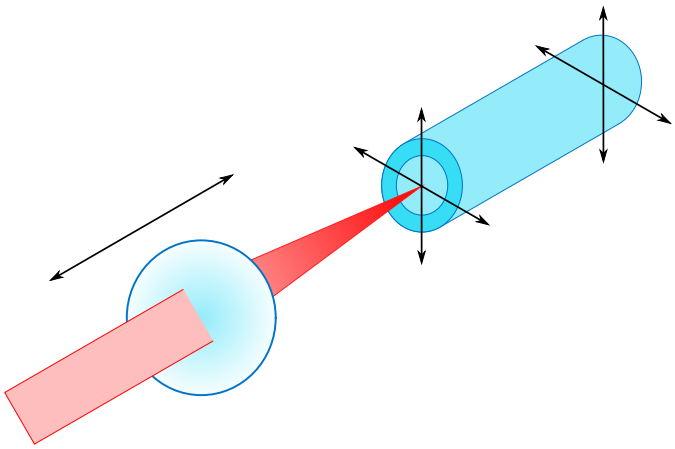

Figure 5.10: *Schematic of the alignment arrangement for the capillary. Each end of the capillary can be translated independently in the x and y directions (perpendicular to the propagation direction). The focusing lens can be translated in the z direction.*

5.7.1 Experimental procedure

The arrangement used is that described in section 2.4. Here, some additional details of alignment arrangements and experimental procedures are given. The alignment arrangement for the capillary is shown in figure 5.10. To align the capillary, first the z position of the lens is set, then the capillary is aligned by alternately moving the entrance and exit faces. The optimum alignment is considered to be when the transmission is at a maximum and the image (recorded at the 'Measurement' position in figure 4.4) is as symmetric as possible. For each z position of the lens, the transmission of the capillary is recorded with no gas present, and then the nominal gas pressure in the capillary is increased from 0–100 mbar in 10 mbar steps. At each pressure, setting the fluorescence from the Ar^+ ions in the capillary is recorded.

In the latest set of experiments, reported here, the transmission of the capillary with gas was not recorded as, at the higher pressures used, the gas caused the fundamental beam to diverge sufficiently that the beam was clipped at the exit window, and so the power could not be reliably measured. This effect indicates that these experiments are reaching the limits of the regime in which this model

can be successful. For accurate modelling of the regime where plasma defocusing has a significant effect, a more sophisticated model, as discussed in section 5.9, is needed. In earlier experiments, with only slightly lower transmission ($\sim$ 60–70 %, rather than the $\sim$ 80 % achieved here) these effects were not observed. The lower transmission experiments are not reported, as the alignment procedure in that case was not consistent, and the pointing stability of the laser was not as good. These effects make comparison with theory more complex.

5.7.2 Results

Figure 5.11 shows the experimentally measured transmission as a function of z_0 for the more recent, high transmission, experiments. As the experimental measurements only give relative values of z_0, the relative values z_{0R} have been centred as $z_0 = z_{0R} - z_c$, where z_c is the centre of mass of the data points. The centre of mass is given by

$$z_c = \frac{\sum z_i T_i}{\sum T_i}, \tag{5.21}$$

where z_i and T_i are the z position and transmission of the ith data point respectively. This selection of a zero point is necessary as the lens can be moved on a translation stage towards and away from the capillary with high accuracy, but accurate measurements of the exact distance between the capillary and lens could not be taken.

The transmission data show a peak in transmission, as is expected from the coupling efficiencies plotted in figure 5.4(a). However, the peak value is at $\sim$ 82 % rather than the value of 98 % that is expected for perfect coupling. Experimental measurements have determined that the spot size w_0 at the capillary is close enough to $0.64a$ that spot size should not have this effect.[4] This leaves the possible explanations for lower coupling efficiency as a non-Gaussian or elliptical beam, an imperfect capillary, or misalignment in the other four degrees of freedom (x_0, y_0, θ and φ).

[4]From examination of figure 5.2 it is seen that the coupling efficiency is not strongly dependent on w_0 in the region $w_0 \approx 0.64a$.

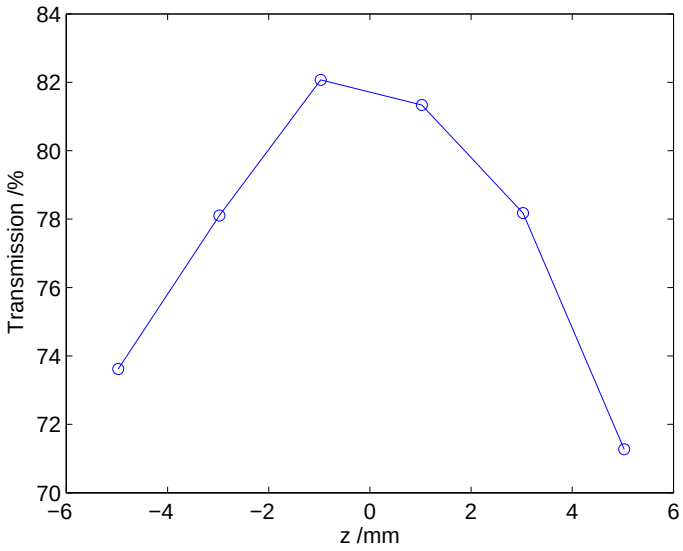

Figure 5.11: *Experimentally measured capillary transmissions as a function of z position of the focusing lens. See text for details of the determination of the values of* z_0.

Any of these are possible causes of the observed low transmissions. Measurements of the beam profile in the region of the focus show approximately Gaussian profiles, but the measured M^2 factor of the beam [123] is 1.8, indicating that the beam is not a perfect Gaussian. The capillary entrance was imaged under an optical microscope before the experiment began, and no imperfections were noted, but the laser may have damaged the capillary during the experiment. The issue of misalignment is complicated by the fact that the alignment changed between each transmission measurement, due to adjustment of the lens. This means that the alignment for the experiment cannot be specified by one particular set of x_0, y_0, θ, φ that are constant for all z_0, but that they can change between z_0 settings.

Even in light of this, it is still instructive to investigate the size of misalignment needed to reduce the transmission to the experimentally observed values. It is possible that the alignment procedure may have a tendency to get stuck in a local maximum of transmission and thus a similar value of the misalignment parameters may be found at all z positions.

To simplify the investigation, the misalignments will be restricted to two degrees

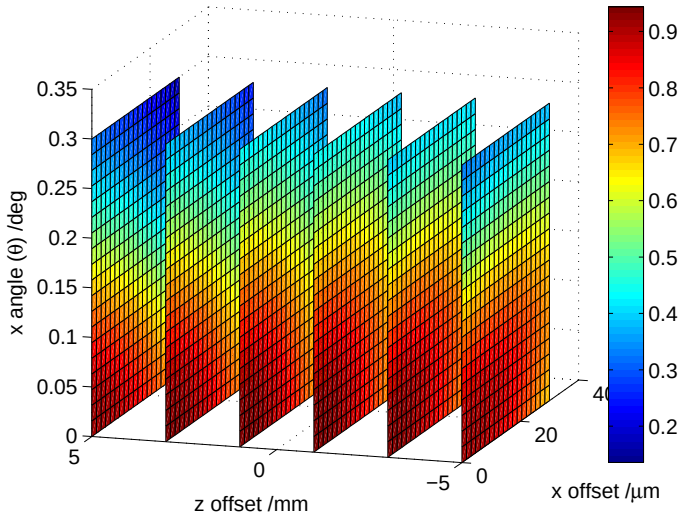

Figure 5.12: *Theoretically predicted transmission of the capillary as a function of x_0, z_0 and θ. Transmission is denoted by the colour scale, as shown in the colour bar. The slices are at the z_0 values used in the experiment.*

of freedom, x_0 and θ, with the other values assumed to be $y_0 = \varphi = 0$. As the field profile in the capillary can be assumed to be radially symmetric (section 5.3.2), x_0 and y_0 are equivalent, as are θ and φ. Therefore, this approximation still allows the model to account for all effects except those caused by an angular misalignment out of the plane of a translational misalignment.

Figure 5.12 shows the predicted transmission of the capillary with no gas as a function of the three misalignment parameters z_0, x_0 and θ. This figure shows an interesting feature of the misalignment in multiple dimensions. For negative z_0 and a positive x_0, the transmission actually increases with θ, as the laser rotates around its focal point to line up with the capillary entrance. This is shown more clearly in figure 5.13 which plots the surface in (x_0, z_0, θ) space for which the transmission is 80 %. (This value was chosen as it is around the experimentally measured values.) The region of interest is on the right hand side, where the surface "bulges" as θ increases. In the rest of the plot, transmission decreases with increasing θ; here the transmission has a peak at $\theta \neq 0$.

The main use of figure 5.13 from the point of view of determination of exper-

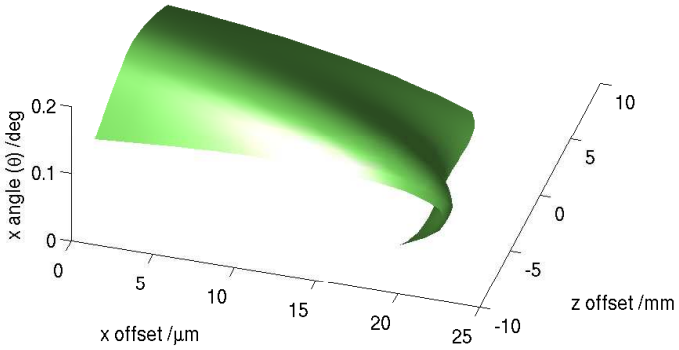

Figure 5.13: *Surface for which the theoretically predicted transmission with no gas is* 80 %. *The region in which a misalignment in angle increases the transmission is clearly seen on the right hand side.*

imental parameters, is that it may be used to reduce the degrees of freedom that must be considered in misalignment. Consider the case for one z position (plotted in figure 5.14 for $z_0 = -1$ mm). In principle, the actual experimental alignment could lie anywhere on this plane. However, if the transmission with no gas is known, the experiment is restricted to those points along the line with the correct transmission. This means that for each z_0 position, there is only one free parameter; if x_0 is free, θ is known, and if θ is free, x_0 is known. This analysis reduces the parameter space that must be searched to fit experiment to theory from a 2-dimensional space to a 1-dimensional one.

Pressure variation

The results of the experimental runs are shown in figure 5.15. The experimental pulse is Gaussian in time with a FWHM pulse length of 40 fs and a pulse energy of 768 μJ. These images show the variation in intensity of fluorescence from Ar^+ ions as a function of propagation distance z and nominal pressure. The actual pressure profile in the capillary is described in section 2.5. Briefly, it consists of a constant region at the nominal pressure between the gas inlet holes, a step of ~ 20 % and

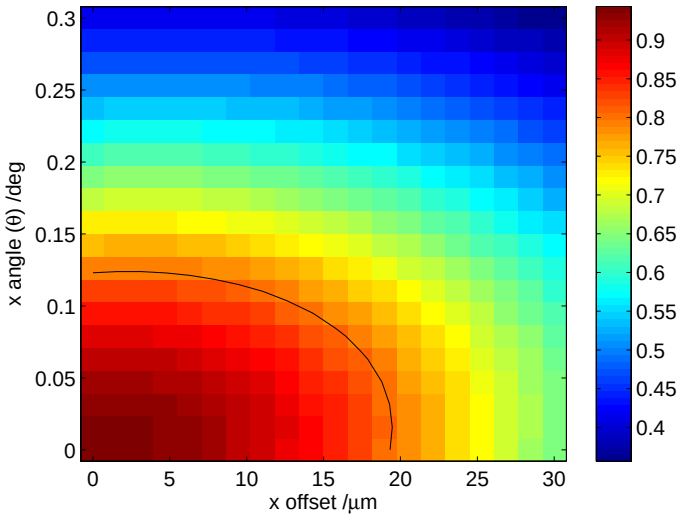

Figure 5.14: *Theoretical transmission with no gas as a function of x_0 and θ for $z_0 = -1$ mm. The black line is the 80 % contour. The experimental parameters x_0 and θ must lie somewhere on the black line.*

then a linear gradient to zero at the entrance and exit faces. The expected beating between modes is seen, although the complex structure makes it difficult to resolve the exact beats from these plots. This beating is discussed as a function of z_0 below.

To compare these data to the theory, the experimental values of z_0, pulse length, pulse energy and capillary geometry are used as input to the modal propagation model. The transmission with no gas was used to reduce the choice of coupling conditions to one free parameter: the ratio of x_0 to θ. The theoretical predictions for four values of this parameter are shown in figure 5.16 for $z_0 = -1$ mm. Comparing the various plots in figure 5.16, it is seen that the main features remain constant over the coupling changes, but that in general increasing x_0 and reducing θ leads to an increase in fine structure in z. The experimental data do not show this fine structure, but this may be due to the resolution of the experimental measurements as scattering of emitted light by the capillary and containing tube walls may be smoothing the observed data. The increase in fine structure can be qualitatively explained by looking at the effect of x_0 and θ on an otherwise perfectly coupled capillary (figure 5.17).

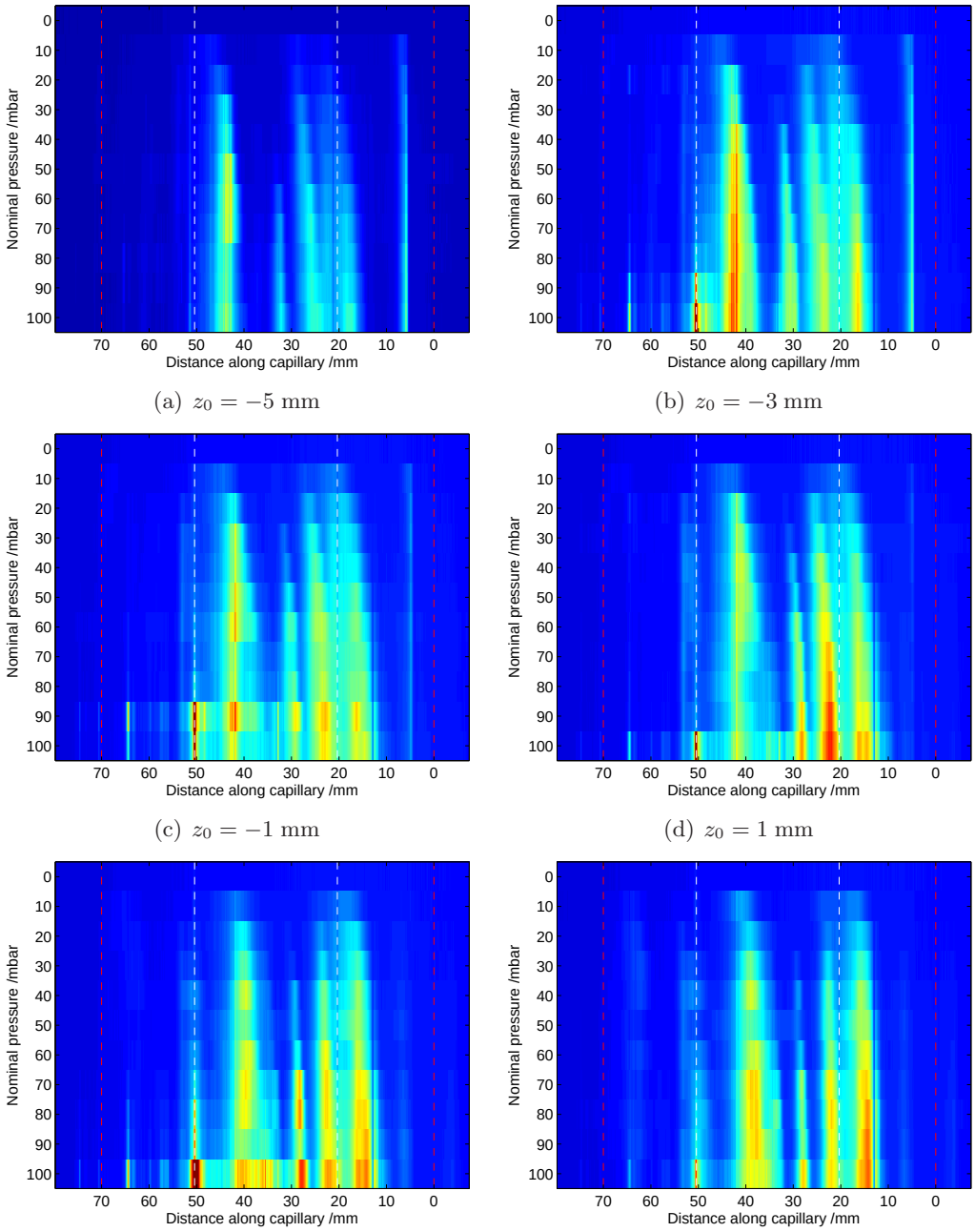

(a) $z_0 = -5$ mm

(b) $z_0 = -3$ mm

(c) $z_0 = -1$ mm

(d) $z_0 = 1$ mm

(e) $z_0 = 3$ mm

(f) $z_0 = 5$ mm

Figure 5.15: *Experimentally observed capillary fluorescence as a function of propagation distance and nominal pressure. Colour is proportional to the intensity of the observed fluorescence, with the same colour scale across all figures. The red dotted lines mark the capillary entrance and exit. The white dotted lines mark the two gas inlet holes in the capillary. The beam propagates from right to left, i.e. the capillary entrance is at* $z = 0$ mm.

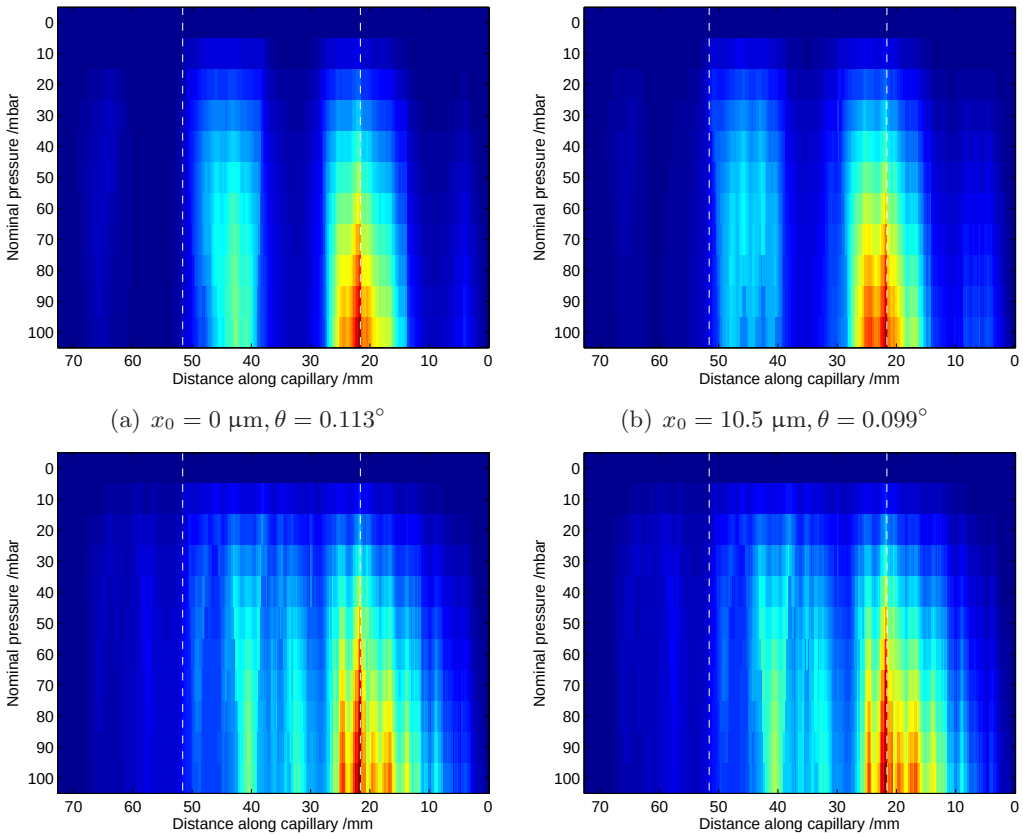

(a) $x_0 = 0\ \mu\text{m}, \theta = 0.113^\circ$

(b) $x_0 = 10.5\ \mu\text{m}, \theta = 0.099^\circ$

(c) $x_0 = 17.9\ \mu\text{m}, \theta = 0.016^\circ$

(d) $x_0 = 17.7\ \mu\text{m}, \theta = 0^\circ$

Figure 5.16: *Theoretically predicted capillary fluorescence as a function of propagation distance and nominal pressure for various different misalignment parameters. In all figures* $z_0 = -1$ mm *and the transmission with no gas is the experimentally measured value of* 82 %*. These theoretical figures correspond to the experimental results in figure 5.15(c). Colour is proportional to the number of* Ar^+ *ions present. The capillary entrance and exit are at the edges of the figure. The white dotted lines mark the two gas inlet holes in the capillary. The beam is propagating from right to left.*

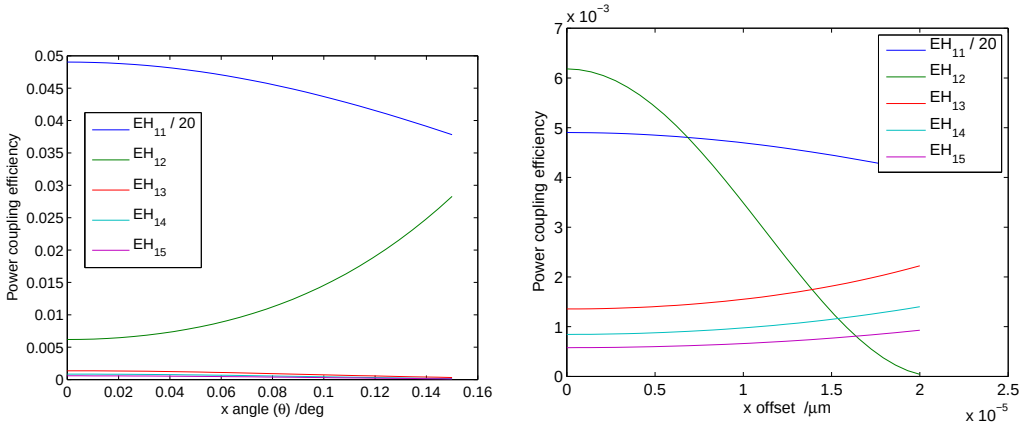

(a) (b)

Figure 5.17: *Power coupling efficiency of each mode as a function of (a) θ and (b) x_0. Note that increasing θ increases the proportion of the EH_{12} mode, while increasing x_0 decreases it. The efficiency of the EH_{11} mode has been divided by 20 to fit on the same scale.*

In figure 5.17 it is seen that the response of the EH_{12} mode to the different misalignments is very different. For similar reductions in EH_{11} coupling (~ 20 %), the EH_{12} mode increases in intensity by a factor of ~ 3 if the capillary is misaligned in angle, while the higher order modes ($m > 2$) reduce in intensity. In contrast, if the capillary is misaligned in x_0, the EH_{12} mode is suppressed, while the higher order modes are more strongly excited. This leads to the observed strong beats at a beat length of 23 mm — the beat length between the EH_{11} and EH_{12} modes — in the angle misaligned case, and suppression of these beats and beating at many higher frequencies in the offset case.

A qualitative comparison of figure 5.16 and figure 5.15(c) shows that figure 5.16(c) is the best match between experiment and theory, with a similar pressure response and three strong, sharp beats: one at ~ 23 mm; one at ~ 30 mm; and one at ~ 42 mm. Thus, these parameters, or their equivalent when adjusted for z_0 and the experimentally measured transmission, are used in the remainder of this discussion.

Figure 5.18 shows the theoretically predicted Ar^+ concentrations for all the experimentally used z_0 values. The agreement between experiment and theory is rea-

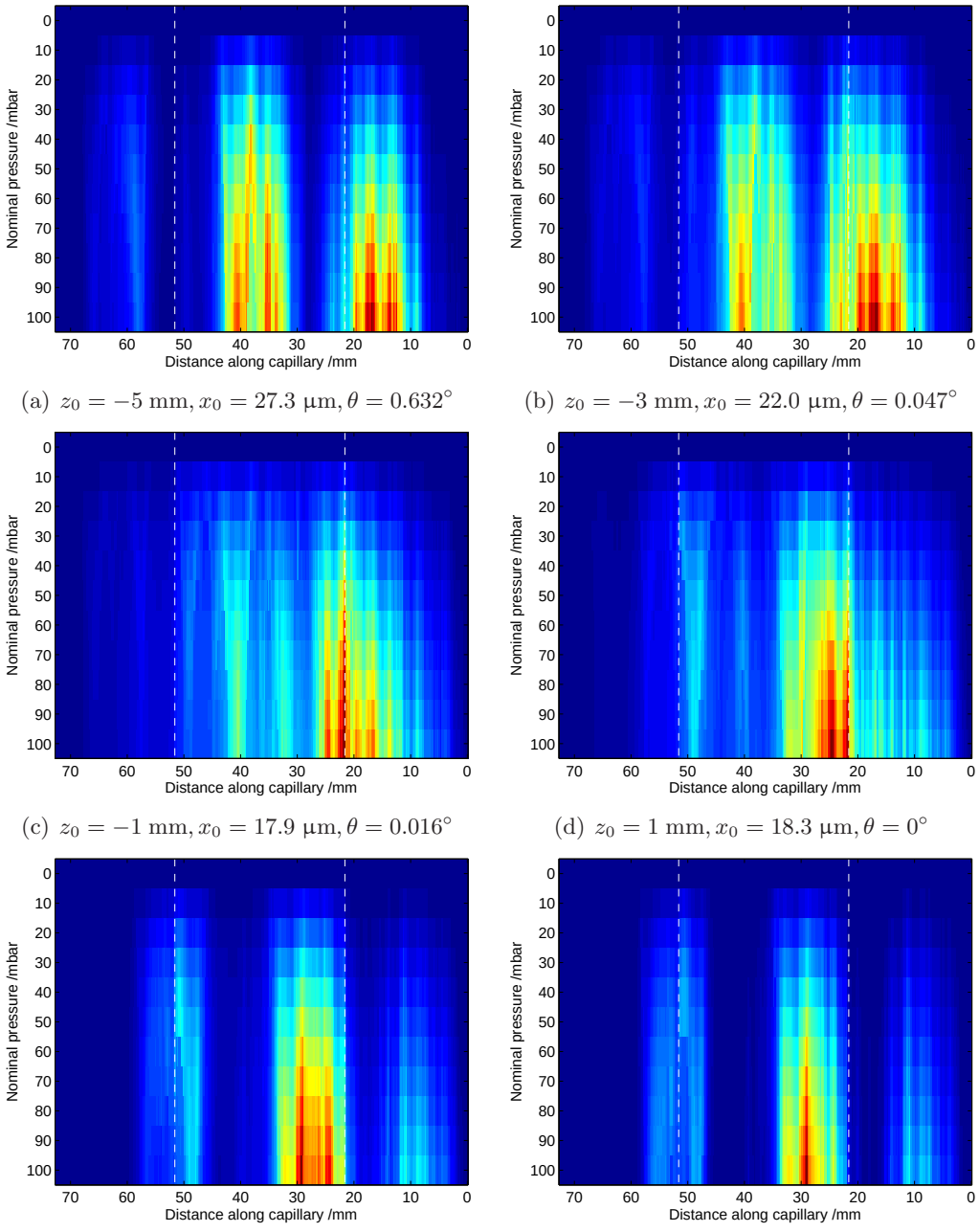

(a) $z_0 = -5$ mm, $x_0 = 27.3$ µm, $\theta = 0.632°$

(b) $z_0 = -3$ mm, $x_0 = 22.0$ µm, $\theta = 0.047°$

(c) $z_0 = -1$ mm, $x_0 = 17.9$ µm, $\theta = 0.016°$

(d) $z_0 = 1$ mm, $x_0 = 18.3$ µm, $\theta = 0°$

(e) $z_0 = 3$ mm, $x_0 = 20.8$ µm, $\theta = 0°$

(f) $z_0 = 5$ mm, $x_0 = 26.1$ µm, $\theta = 0°$

Figure 5.18: *Theoretically predicted Ar^+ concentrations as a function of propagation distance and nominal pressure for the experimental z_0 values and best fit misalignment parameters. In each figure the transmission with no gas is the experimentally measured value (figure 5.11). These theoretical figures correspond to the experimental results in figure 5.15. Colour is proportional to the number of Ar^+ ions present. The capillary entrance and exit are at the edges of the figure. The white dotted lines mark the two gas inlet holes in the capillary. The beam is propagating from right to left.*

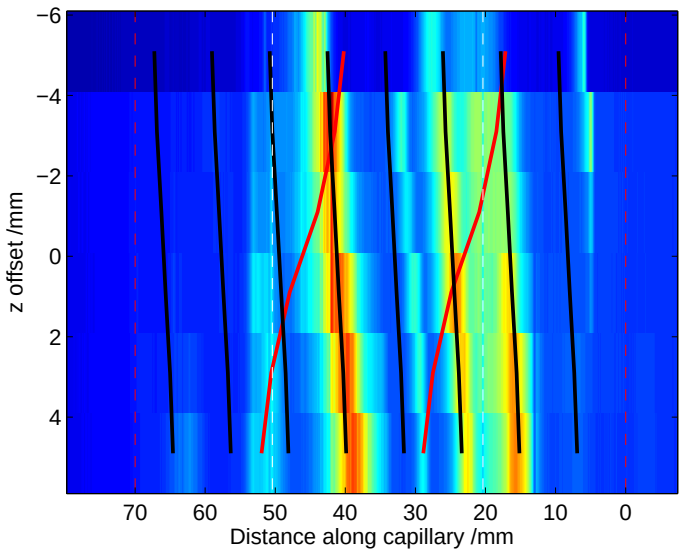

Figure 5.19: *Experimentally observed fluorescence as a function of z and z_0 at a fixed pressure of* 40 mbar*. The solid red lines mark the expected position of the EH_{11}–EH_{12} beat and the solid black lines mark the position of the EH_{11}–EH_{13} beat (see text for explanation). The EH_{11}–EH_{12} beats are not observed. Colour is proportional to the intensity of the observed fluorescence. The red dotted lines mark the capillary entrance and exit. The white dotted lines mark the two gas inlet holes in the capillary. The beam is propagating from right to left.*

sonably good, though quantitative comparisons are difficult between the plots. A more quantitative comparison can be made by looking at the variation of emission with z_0 at a single pressure, as is done in the next section.

Variation with z displacement

For comparison at a single pressure, the value of 40 mbar is chosen. This pressure is in the middle of the experimental range, and is low enough that the ionisation effects should play a small role, yet high enough that a reasonable fluorescence signal is recorded. Figure 5.19 shows the experimentally observed fluorescence as a function of z and z_0 for a fixed pressure of 40 mbar. The solid lines in the figure show the expected position of the beats between the EH_{11} mode and each of the EH_{12} and EH_{13} modes. These are calculated using equation 5.20, with a modification of the first beat length due to the phase shift between modes at coupling. In figure 5.4(b)

it was seen that the relative phases of the modes at the capillary entrance were dependent on z_0. This shift should change the position of the first beat in the capillary, and all subsequent beats should follow the first at the standard beat length. Investigation of the coupling phases as a function of x_0 and θ shows that these misalignments do not affect the phase, so only phase shift due to z_0 is relevant here. If the difference between phases of mode EH_{1p} and EH_{1q} due to coupling is $\Delta\phi = \phi_p - \phi_q$, then the length of the first beat, in terms of the standard beat length ζ_{pq}, is

$$\zeta'_{pq} = \left(1 - \frac{\Delta\phi}{2\pi}\right)\zeta_{pq}. \tag{5.22}$$

This value is used to calculate the positions of the beats in figure 5.19; for each z_0 value, lines are plotted at $z = \zeta'_{pq} + n\zeta_{pq}$ where $n = 0, 1, 2, \ldots$.

In figure 5.19 the beats of the experimental data are clearly seen to correspond to the EH_{11}–EH_{13} beat, with no evidence of beating between the EH_{11} and EH_{12} modes, which indicates that the EH_{12} mode is being suppressed. The same pattern of beats is also seen at all experimental pressures, which indicates that ratios of the modes are not significantly changed by propagation, i.e. that the nonlinear coupling between modes is weak at pressures up to 100 mbar.

The theoretical data (figure 5.20), in contrast to the experiment, show strong EH_{11}–EH_{12} beats, and overall little evidence of EH_{11}–EH_{13} beats. In the two centre z_0 positions, $z_0 = \pm 1$ mm, there is evidence of beating at the points expected for the EH_{11}–EH_{13} beats, but it is weak compared to the EH_{11}–EH_{12} beats. This effect is yet to be explained fully by the theory, but it could be due to alignment effects because, as demonstrated in figure 5.17, misalignment can suppress the EH_{12} mode. It is also possible that it is due to coupling effects not included in the model, for example an elliptical or non-Gaussian beam. One extension to this analysis is to look at whether suppression of the second mode is possible in more complex misalignments, those with multiple non-zero misalignment parameters, and if so, in what regions of the (z_0, x_0, θ) space it can occur.

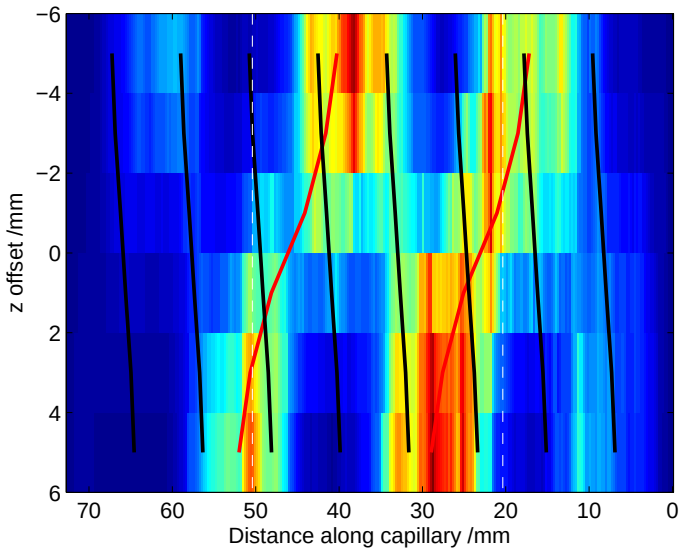

Figure 5.20: *Theoretically predicted Ar^+ ion concentration as a function of z and z_0 at a fixed pressure of* 40 mbar. *The solid red lines mark the expected position of the EH_{11}–EH_{12} beat and the solid black lines mark the position of the EH_{11}–EH_{13} beat (see text for explanation). In contrast to the experimental data (figure 5.19) the EH_{11}–EH_{12} beats are present and the EH_{11}–EH_{13} beats are not discernable. Colour is proportional to the intensity of the observed fluorescence. The capillary entrance and exit are at the edges of the figure. The white dotted lines mark the two gas inlet holes in the capillary. The beam is propagating from right to left.*

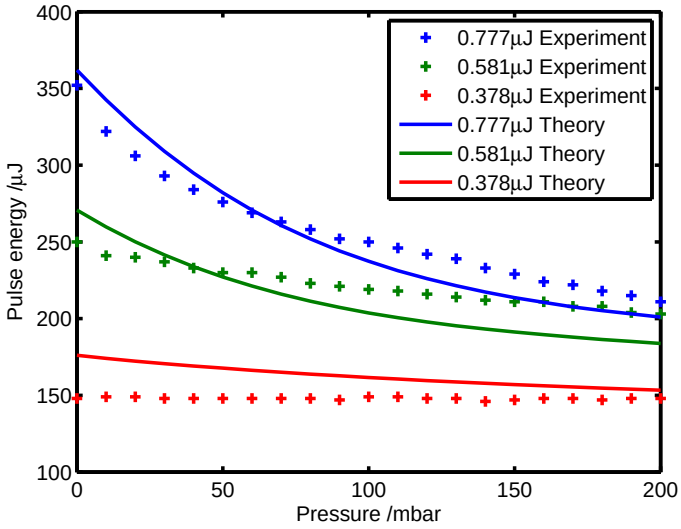

Figure 5.21: *Output pulse energy as a function of nominal pressure in the capillary for various input pulse energies at low coupling efficiencies. The analysis of these experimental data is not as extensive as that above, but the best fit coupling parameters were determined in a similar way. The agreement is good, and shows that modifying the experimental arrangement to allow power measurements at high coupling efficiencies is worthwhile.*

5.8 Uses and limitations of the model

The modal propagation model described above has demonstrated good qualitative agreement with experiment with respect to the observed fluorescence, and has given insight into the effect of coupling alignments in the capillary. Due to experimental limitations, it has not been possible to compare the observed output pulse energies with the theoretical predictions for the most recent data sets. However, initial results for various input powers at lower coupling efficiencies (figure 5.21) show that the results are promising. The next stage is to refine the experimental arrangement to allow power measurements at high transmissions.

This modal propagation model has several uses when applied to the experiments described. The analysis of coupling effects can be used to refine the experimental alignment procedure to obtain the desired coupling. This will normally be coupling for maximum transmission, but may also include suppression of various modes to obtain a particular beating pattern.

The agreement between experiment and theory in the magnitude of fluorescence observed in the pressure gradient regions relative to the centre region, gives an independent experimental verification of the pressure profile predicted by CFD modelling (section 2.5). This gives confidence in the use of further CFD modelling that has been undertaken to design capillaries with tailored pressure profiles for optimum harmonic generation.

The optimisation of capillary design is an area where the modal propagation model can be of direct use, as well as confirming gas flow simulations. In order to generate high harmonics, it is necessary to ionise the generating gas. Therefore, in a simplistic picture (avoiding the complications of, for example, phasematching), the XUV generation at particular a z coordinate is simply proportional to the number of ions created at that z coordinate. However, any XUV radiation is strongly absorbed by the gas. For this reason, the ideal capillary for generation would have a constant pressure region with a sharp drop to very low pressure and a peak in ionisation at the end of the high pressure region (figure 5.22). This design requires a combination of the gas flow CFD modelling and propagation modelling to determine the optimum capillary profile.

The limitations of the modal propagation model lie in the lack of temporal and spatial variation of the pulse, and the neglect of plasma defocusing effects. The plasma defocusing is caused by the refractive index of the capillary being lower in the centre due to the higher concentration of free electrons; this should cause nonlinear coupling between modes. The nonlinear coupling is weak in the experimental results, as discussed previously, so the neglect of plasma defocusing is a small effect.

The temporal reshaping of the pulse, on the other hand, may be having a significant effect, as the intensities used in the experiment are approaching those at which temporal and spectral effects have been observed in other experiments [140, 141]. The main effects introduced by temporal modelling are temporal amplitude reshaping of the beam, where the leading edge of the beam is more strongly absorbed due to ionisation; phase reshaping, where the trailing edge of the pulse is travelling in

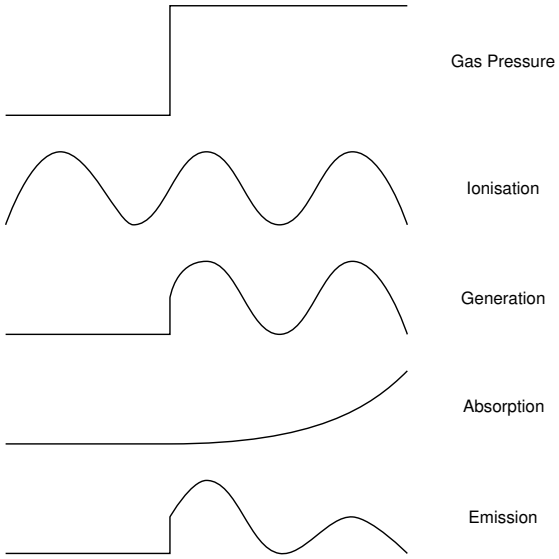

Figure 5.22: *Schematic of an idealised capillary for high harmonic generation, in a simplistic scenario where generation is proportional to ionisation. The pressure profile is constant, with a sharp drop to zero pressure; the ionisation fraction is oscillating, as observed, due to mode beating. The generation is simply the product of these two functions. Absorption from a particular z coordinate is also shown, and the last curve shows emission from a particular z coordinate, given by the emission from that point multiplied by the absorption. An ideal capillary has a peak ionisation rate coinciding with the end of the high pressure region.*

a lower refractive index medium, and so should "catch up" with the leading edge; and temporal walk-off between capillary modes, as each mode has a different group velocity in the capillary. These effects are included in the more sophisticated model currently in development and described in section 5.9.

5.9 Further work

The modal propagation model (MPM) presented above has many uses in predicting experimental output and improving experimental procedures and design. It is also computationally fast, and provides a qualitative measure of the XUV generation. However, the model also has several limitations: it is not able to model spectral or temporal evolution of the pulse and it does not take into account the plasma defocusing effects that should lead to coupling between modes. The uses of this model suggest that the development of a more sophisticated model that can take into account plasma defocusing and temporal effects is worthwhile, and such a model is being now being developed.

5.9.1 Time-dependent model development

This section is a collaboration with Peter Horak of the Optoelectronics Research Centre. The analytic and computational development of this model is being undertaken by Peter Horak. The model is being guided by the experimental and theoretical results presented above.

This more sophisticated model — which will here be called the multimode nonlinear Schrödinger equation (MM-NLSE) model, due to the form of propagation equation used — was originally developed for modelling nonlinear propagation in optical fibres [148] and has subsequently been converted to use the nonlinear effects of plasma generation in place of the standard nonlinear effects of fibre optics.[5] As with the MPM, the new model treats the electric field within the capillary as a

[5]See [144] for a discussion of nonlinear propagation in optical fibres.

sum of capillary modes with coefficients $C_m(z)$. However, instead of the coefficients being the same for the whole pulse, they are now a function of time $C_m(z,t)$ so the electric field profile is now changing in time. The other major difference between the MPM and the MM-NLSE model, is that the MM-NLSE model does not propagate each mode coefficient separately (equation (5.10)), but instead derives an equation for propagation that takes into account the coupling between modes due to the presence of the plasma. The MPM assumes that

$$\frac{\mathrm{d}C_m(z)}{\mathrm{d}z} = i\gamma_m z C_m(z) \quad \Longrightarrow \quad C_m(z) = C_m(0)\exp\left(i\gamma_m z\right), \tag{5.23}$$

which allows no coupling or cross-talk between modes, as the value of C_m depends only on previous values of C_m. In the new MM-NLSE, C_m is not only a function of z but also of t, as described above, and a propagation equation of the form

$$\frac{\partial C_m(z,t)}{\partial z} = f\Big(C_1\left(z,t\right), C_2\left(z,t\right), \ldots, C_M\left(z,t\right)\Big) \tag{5.24}$$

is derived. This equation implies that the change in C_m between points z and $z+\Delta z$ is dependent, in principle, on the coefficients of all modes present. A simple example that shows the necessity of this more complex approach is that of an intense pulse propagating in a medium with a nonlinear refractive index n_2. The total refractive index is then given by $n = n_0 + n_2 I$, where n_0 is the linear refractive index. To propagate this beam, it is necessary to know the intensity at each point, and therefore the propagation of each mode depends on the total intensity of all modes. The case in question here is more complex, and the refractive index is not determined by a simple dependence on total intensity. Instead, it is determined by the ionisation fraction, which is a more complex function of the total electric field at preceding times. Propagation using equation (5.24) allows coupling between modes due to plasma defocusing that was not possible with the MPM.

The MM-NLSE model also introduces a time dependence of the electric field, rather than dealing solely with the peak value and assuming a Gaussian pulse in time.

This change allows the incorporation of several new effects: temporal reshaping due to ionisation losses at the peak of the pulse; temporal reshaping due to the trailing edge of the pulse propagating in a plasma, with the leading edge in neutral gas; and group velocity walk-off between capillary modes. The temporal information also allows calculation of the spectrum at any point in the capillary, and hence the evolution of the spectrum along the capillary.

The major disadvantage of the MM-NLSE model compared to the MPM is the computational time needed to run. For a single run, this model takes ~ 30 min to run, compared to a few seconds for the MPM. This makes it unsuitable for parameter scans (over coupling parameters) in the way the previous model was used, without very significant increases in computational resources. In order to keep the computational effort tractable, compromises have also been made in the precision of results obtained. The number of radial points has been reduced as far as possible while still keeping the ability to decompose into capillary modes, thus the number of points radially is set equal to the number of modes modelled. This is typically 10-30 points, compared to the 150 that were used in the MPM.

The MM-NLSE model also does not include BSI, as to do so introduces large temporal and spatial step changes in ionisation fraction. These abrupt steps require that a very small step size in z is used to maintain the accuracy of the simulation and increase the computing requirements to high levels.

Since the MM-NLSE model is difficult to use for large parameter scans, it may be beneficial to determine the coupling parameters using the MPM model, as demonstrated above, and then use the MM-NLSE to confirm, and possibly correct, the parameters on the small scale, and also to determine the spectral and temporal profile of the beam during and after propagation. This use would combine the benefits of the computationally fast MPM and the extra information provided by the MM-NLSE model.

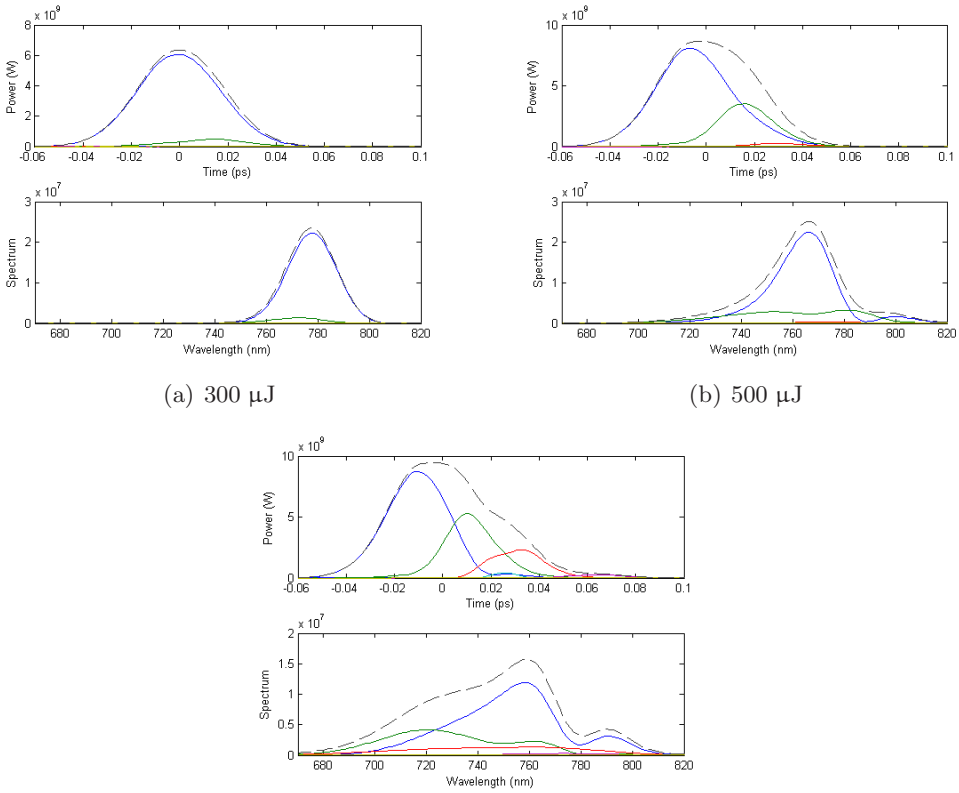

(a) 300 μJ

(b) 500 μJ

(c) 650 μJ

Figure 5.23: *Temporal and spectral profiles of a laser pulse of various pulse energies after propagation through a capillary, as predicted by the MM-NLSE model. In each case, the top plot shows the time profile, and the bottom plot the spectrum. The lines are: solid blue line – EH_{11} mode; solid green line – EH_{12} mode; solid red line – EH_{13} mode; black dotted line – sum over all modelled capillary modes. The input pulse length is* 40 fs*; the capillary nominal pressure is* 80 mbar*.*

Time-dependent model results

The MM-NLSE model is still under development, and no systematic comparison of the predictions of theory to experimental results has yet been undertaken. Here, some preliminary results are presented to show the type of information provided by the MM-NLSE model.

Figure 5.23 shows the results of three sample runs of the MM-NLSE model at different input powers. These are all for optimum coupling, so the 650 μJ plot is close to the experimental conditions used above. The results show that at 300 μJ,

the pulse spectrum and temporal profile are largely unchanged by propagation, with a slight shift in time of the EH_{12} mode relative to the EH_{11} mode due to the differing group velocities of the two modes. At 500 μJ the spectrum of the pulse has begun to evolve, but the temporal profile is largely unchanged, still being roughly Gaussian in shape with a 40 fs pulse length. Only at the 650 μJ pulse energy is any significant temporal pulse distortion seen, and this is at 80 mbar, which is at the high end of the experimental pressures used in the results presented above. In principle, this shows that, as expected, the approximations of the MPM model break down at around the high pressure end of the experimental parameters used, and that the MM-NLSE model is better suited to higher powers and pressures than those used above. These higher powers and pressures are available experimentally, and so modelling of these regimes is of interest. The results also show that at high powers and pressures, the EH_{12} and EH_{13} modes are more strongly excited, implying that nonlinear mode coupling is having a significant effect. Only nonlinear mode coupling due to amplitude reshaping is accounted for in the MPM model, whereas the MM-NLSE model also includes coupling due to plasma defocusing. For this reason, the MM-NLSE model should be more accurate as mode coupling becomes significant.

The plots show that in general, the different spatial modes of the capillary have different temporal and spectral profiles, and it would therefore be useful to have a way of separating these modes experimentally, so that the spectral content of each mode, for example, could be measured. If the capillary mode profiles (as defined in section 2.3) are propagated into the far field using Fraunhofer diffraction (as described in section 4.4.3), then the intensity profiles of each mode at a large distance from the capillary can be found. These intensity profiles are plotted in figure 5.24 as a function of angle. For each mode other than the EH_{11}, there is a position where there is a peak of intensity coinciding with a zero of intensity for all the other modes. In principle, if a sufficiently small detector can be used to sample this spatial region, it could obtain information about the spectral properties of that mode. However, this analysis is carried out for a quasi-monochromatic beam, and beams with a large

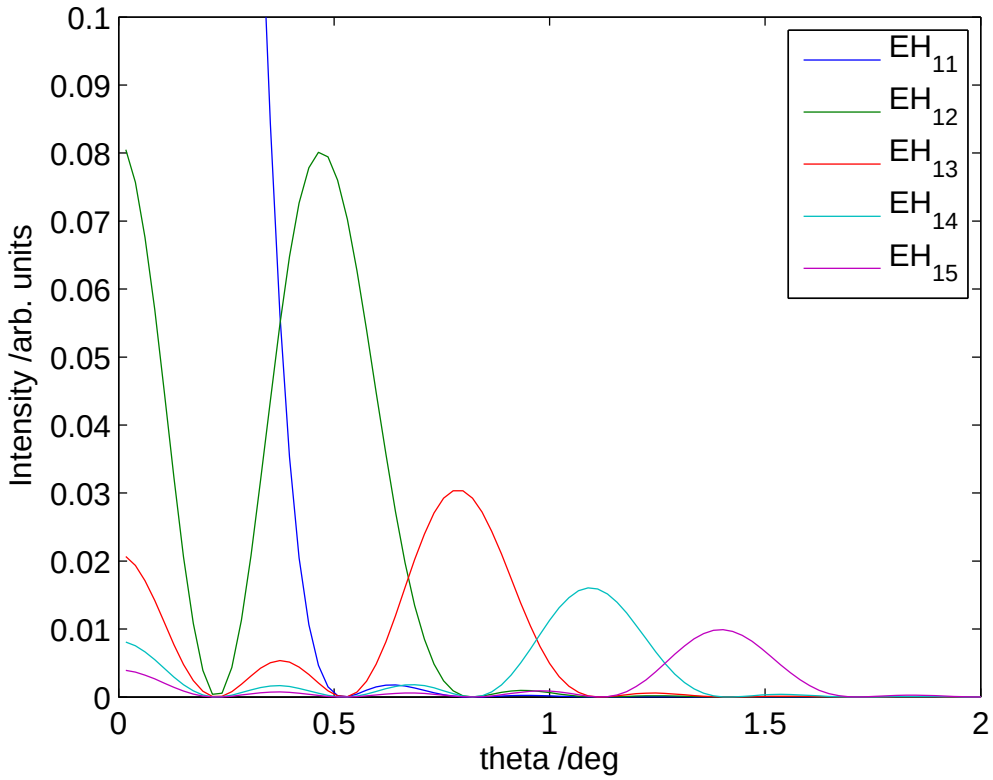

Figure 5.24: *Angular intensity profiles of the first five capillary modes after propagation into the far field. For each mode EH_{1m}, where $m \geq 2$, there is a peak at some angle at which all the other modes have zeros of intensity.*

bandwidth will smear out the propagated structure, leading to washing out of the zeros of intensity. If the propagation equations are analysed, it is found that the angle to which a particular spatial frequency is diffracted is proportional to the wavelength of the light. This means that a beam with a 700–800 nm bandwidth, as shown in figure 5.23(c), will have a $\pm \sim 7$ % spreading of the angular intensity profile. Further work is needed to determine whether the resolution of this spatial method of mode selection is sufficient to resolve spectrally broadened beams.

5.9.2 Propagation model as input to phasematching calculations

A further development that could be applied to either of the propagation models studied here, is to use the output of the model as an input to the phasematching model described in chapter 3. This would prediction of the XUV flux, spectrum and spatial profile, given a set of input coupling parameters and a gas profile. This would be most useful after the effects of pressure gradients have been taken into account (section 4.5.1) to fully model the whole capillary length.

The greatest benefit would be obtained by using the output of the MM-NLSE model rather than the MPM, as the MM-NLSE predicts the full spatial and temporal profile of the laser field and would thus provide most information to the spatially and temporally dependent phasematching calculations. The use of the MPM model would provide greater spatial information than is currently used in the phasematching model, but would not provide any new temporal information.

While the temporal profile from a propagation model could easily be included in the phasematching model, the use of a multimode generation beam would require further work, as the current model assumes a single propagation constant for the fundamental beam (the propagation constant of the EH_{11} mode β_{11}). While this is easily corrected for any other single mode — i.e. the propagation constant of mode EH_{1m}, β_{1m}, can be used in place of β_{11} — a multimode beam is more complex, as it has no single propagation constant. In principle, each mode of the capillary should phasematch differently with the generated XUV radiation. In practice, it

may be acceptable to neglect generation from all modes other than the EH_{11} mode, as higher order modes phasematch ($\Delta k = 0$) for lower ionisation fractions than the fundamental.

Recall that the phase mismatch is given by (equation (3.12))

$$\Delta k \approx q\frac{u_{1m}^2\lambda_0}{4\pi a^2} + N_e r_e\left(q\lambda_0 - \lambda_q\right) - \frac{2\pi P}{\lambda_q}\left\{\delta(\lambda_0) - \delta(\lambda_q)\right\}. \tag{5.25}$$

Setting $\Delta k = 0$ and solving for $\eta = \frac{N_e}{PN_{\mathrm{atm}}}$ gives

$$\eta = \frac{P\Delta k_{\mathrm{gas}} - u_{1m}^2\frac{q\lambda_0}{4\pi a^2}}{P\Delta k_{\mathrm{plasma}}}, \tag{5.26}$$

where $\Delta k_{\mathrm{gas}} = \frac{2\pi}{\lambda_q}\left\{\delta(\lambda_0) - \delta(\lambda_q)\right\}$ and $\Delta k_{\mathrm{plasma}} = N_{\mathrm{atm}} r_e\left(q\lambda_0 - \lambda_q\right)$. So the ionisation fraction at which a particular harmonic is phasematched decreases as m increases. For argon at 50 mbar, the required ionisation fraction for phasematching with the EH_{12} mode is negative for all harmonics. Clearly a negative ionisation fraction is unphysical, and so the second harmonic will never phasematch. As the pressure increases, it becomes possible to phasematch with the EH_{12} mode, but still at a lower ionisation fraction than that at which the EH_{11} mode phasematches. Since the ionisation fraction is monotonically increasing, any generation that is phasematched with a high order mode must occur earlier in the pulse than generation phasematched with the EH_{11} mode. As all phasematched generation occurs on the leading edge of the pulse, generation that is phasematched with high order modes must be driven by a lower strength electric field, and consequently will be of lower flux.

Another complication introduced by the use of a propagation model to determine the laser pulse to use for phasematching, is that the pulse produced by the propagation model varies with z position. The assumption made in the phasematching calculations is that the pulse does not change over the generation region. To use the model of phasematching presented in chapter 3, it will be necessary to take the laser pulse at one z and assume that it does not change. This is probably still a good

assumption because, as described in the assumptions of the phasematching theory, the generation length is short.

5.10 Conclusions

A modal propagation model has been presented in this chapter for modelling propagation in a capillary filled with ionising gas in a low power, low pressure regime. The model is computationally undemanding and has demonstrated good agreement with experiment in its intended use. However, it is limited in that it will not work for the higher powers and pressures now available experimentally. A more sophisticated model has been outlined that is currently under development in collaboration with others within the department, and initial results have been shown that confirm the validity of the MPM in the low intensity regime. A possible method for investigating the spectral content of different capillary modes at the output of the capillary has been suggested, although further work is needed to check the validity for a polychromatic beam. Finally, the use of the propagation models as inputs to the phasematching model (chapter 3) has been discussed, along with some of the complications that would result from a combination of the models. Such a combination could be very useful in predicting the output of a complete capillary HHG experiment: from input laser coupling to output XUV intensity.

Chapter 6

Conclusions

Two new models have been presented in this thesis for use in understanding capillary high harmonic generation. The first is a spatio-temporal model of phasematching in capillary HHG, and the second is a modal propagation model of high intensity laser propagation through a hollow waveguide filled with ionising gas.

Phasematching model

The phasematching model takes into account the full spatio-temporal variation of ionisation fraction to determine the emitted XUV pulse as a function of time, radius and harmonic number. The model begins by calculating the ionisation fraction as a function of space and time, which allows calculation of the phase mismatch for each harmonic at each space and time coordinate. This phase mismatch, together with knowledge of the absorption characteristics of the gas, allows the full XUV build-up to be calculated. The model assumes a very simple single atom response, that of a plateau and hard cutoff at $E_c = I_p + 3.17\,U_p$. A number of simplifying assumptions can be made because build-up length is limited to the absorption depth of the harmonic in the medium, and so is of the order of a few millimetres.

A number of conclusions can be drawn from the model at this stage, the most notable of which is that the harmonic generation process is self limiting and that attempts to improve either the flux of photons or the cutoff energy by increasing the

intensity have a limited effect; in the case of cutoff, the effect is far smaller than is predicted by simply calculating the cutoff energy at the peak of the pulse.

The model has been compared to experimentally measured spectra for a number of gases, and found to predict accurately the distribution of energy between harmonics and the position of the high energy cutoff for argon, nitrogen, nitrous oxide and neon. The model has been applied to gas mixtures, where helium is mixed with argon in an attempt to balance the refractive index of the plasma generated by the argon atoms with that of the neutral helium. This balancing should allow generation of higher energy harmonics, as the time at which generation is phase-matched moves closer to the peak of the pulse. When compared to experiment, qualitative agreement in the movement of the cutoff is seen; however, the theory tends to over-estimate the magnitude of the increase.

The spatial predictions of the phasematching model, together with semi-classical predictions of the phase of the harmonics, have been used to investigate the propagation of the XUV beam after it leaves the capillary and propagates in free space. The methods used for propagation are the angular spectrum method, in the near field region, and Fraunhofer diffraction, in the far field, the computational limits of which are briefly discussed. Propagation calculations are used to predict the divergence of the XUV beam and give a value which is found to be in agreement with preliminary experimental measurements. It is also noted that, for a highly polychromatic beam, such as that generated by an HHG experiment, the M^2 measure of beam quality must be carefully considered, as it depends on the definition of a single wavelength for the beam which cannot easily be calculated for a polychromatic beam.

Modal propagation model

The modal propagation model is simple and computationally fast, and is based on the assumptions that the temporal profile does not vary with propagation and the nonlinear coupling between modes due to phase effects is weak. These assumptions are shown to be valid in the low pressure, low intensity regime of the experiments

described, but not for higher intensities — including those caused by higher coupling efficiencies — or higher pressures. A more sophisticated model for these regimes has been proposed, and is currently being developed in collaboration with Peter Horak of the Optoelectronics Research Centre.

The effect of misalignment of the capillary on the coupling efficiency of various modes is discussed, and it is found that for well aligned capillaries, the effect of non-radially symmetric modes can be neglected even for a non-radially symmetric input beam. Experimentally, measurements of argon ion fluorescence are taken through the side wall of the capillary. Comparison of these measurements with predicted numbers of argon ions, as a function of pressure in the capillary, shows good agreement. However, when the results are analysed as a function of the z position of the capillary entrance relative to the beam waist, it is found that there is strong evidence in the experimental data of suppression of the EH_{12} mode and this suppression is not seen in the theoretical data. However, analysis of coupling efficiencies shows that, in simple cases, certain misalignments can cause suppression of the EH_{12} mode. Further work is needed to discover whether this suppression can extend to complicated misalignments.

The modal propagation model has uses in validating the CFD modelling previously done by Matthew Praeger that determines the pressure profile in the capillary, and in designing capillaries for optimum harmonic generation. The optimum capillary would have a pressure profile with a sharp drop just after a peak in ion density, to generate efficiently with minimum subsequent absorption of the harmonics.

The greatest use of the propagation model would be obtained if the output of the propagation model, either the modal model or the more sophisticated time-dependent model, were used as input to the phasematching calculations. This would provide an end-to-end model of the generation process. Firstly, the input laser beam is coupled into the capillary and propagated in the presence of the ionising gas. The generation is then calculated using the phasematching model, and finally the XUV beam is propagated from the capillary to the detection equipment, whatever that

may be. This end-to-end model would, in principle, allow optimisation of every step of the generation experiment.

References

[1] T. H. Maiman. "Stimulated Optical Radiation in Ruby". *Nature*, 187:493–494, 1960.

[2] P. A. Franken, A. E. Hill, C. W. Peters, and G. Weinreich. "Generation of Optical Harmonics". *Physical Review Letters*, 7(4):118–119, 1961.

[3] N Bloembergen. "Nonlinear optics: past, present and future". In DB Ostrowsky and R Reinicch, editors, *Guided wave nonlinear optics*, NATO ASI Series, pages 1–9, Dordrecht, The Netherlands, 1992. Kluwer Academic Publishers.

[4] J. A. Giordmaine. "Mixing of Light Beams in Crystals". *Physical Review Letters*, 8(1):19–20, 1962.

[5] P. D. Maker, R. W. Terhune, M. Nisenoff, and C. M. Savage. "Effects of Dispersion and Focusing on the Production of Optical Harmonics". *Physical Review Letters*, 8(1):21–22, 1962.

[6] RP Feynman, RB Leighton, and M Sands. *The Feynman lectures on physics*, volume 1, chapter 30–31. Addison-Wesley Publishing Company, Reading, Mass., USA, 1963.

[7] C. V. Raman and K. S. Krishnan. "A New Type of Secondary Radiation". *Nature*, 121(348):501–502, 1928.

[8] P. B. Corkum. "Plasma perspective on strong-field multiphoton ionization". *Physical Review Letters*, 71(13):1994–1997, 1993.

[9] M. Lewenstein, Ph. Balcou, M. Yu. Ivanov, Anne L'Huillier, and P. B. Corkum. "Theory of high-harmonic generation by low frequency laser fields". *Physical Review A*, 49(3):2117–2132, 1994.

[10] KJ Schafer, B Yang, LF Dimauro, and KC Kulander. "Above threshold ionization beyond the high harmonic cutoff". *Physical Review Letters*, 70(11):1599–1602, 1993.

[11] JL Krause, KJ Schafer, and KC Kulander. "High-order harmonic-generation from atoms and ions in the high-intensity regime". *Physical Review Letters*, 68(24):3535–3538, 1992.

[12] A. L'Huillier, M. Lewenstein, P. Salières, Ph. Balcou, M. Yu. Ivanov, J. Larsson, and C. G. Wahlström. "High-order harmonic-generation cutoff". *Physical Review A*, 48(5):R3433–R3436, 1993.

[13] G Doumy, S Dobosz, P D'Oliveira, P Monot, M Perdrix, F Quere, F Reau, P Martin, P Audebert, JC Gauthier, and JP Geindre. "High order harmonic generation by non-linear reflection of a pedestal-free intense laser pulse on a plasma". *Applied Physics B: Lasers and Optics*, 78:901–904, 2004.

[14] RA Ganeev, JA Chakera, M Raghuramaiah, AK Sharma, PA Naik, and PD Gupta. "Peculiarities of harmonics generated from interaction of 27 ps laser radiation with solid aluminium targets". *Physica Scripta*, 65(2):155–159, 2002.

[15] D von der Linde and K Rzàzewski. "High-order optical harmonic generation from solid surfaces". *Applied Physics B: Lasers and Optics*, 63(5):499–506, 1996.

[16] P Gibbon. "High-order harmonic generation in plasmas". *IEEE Journal of Quantum Electronics*, 33(11):1915–1924, 1997.

[17] PA Norreys, M Zepf, M Bakarezos, M CastroColins, D Chambers, CN Danson, A Dyson, AP Fews, P Gibbon, MH Key, P Lee, P Loukakos, S Moustaizis, D Neely, SG Preston, FN Walsh, JS Wark, J Zhang, and AE Dangor. "Extreme ultraviolet harmonic generation from ultra-intense picosecond laser-solid interactions: Results and perspectives.". *Multiphoton Processes 1996*, (154):211–220, 1997.

[18] W Kornelis, CP Hauri, A Heinrich, EW Helbing, MP Anscombe, P Schlup, JWG Tisch, J Biegert, and U Keller. "Frequency-sheared, time-delayed extreme-ultraviolet pulses produced by high-harmonic generation in argon". *Optics Letters*, 30(13):1731–1733, 2005.

[19] E Takahashi, Y Nabekawa, M Nurhuda, and K Midorikawa. "Generation of high-energy high-order harmonics by use of a long interaction medium". *Journal of the Optical Society of America B*, 20(1):158–165, 2003.

[20] Zenghu Chang, Andy R. Rundquist, Haiwen Wang, Margaret M. Murnane, and Henry C. Kapteyn. "Generation of Coherent Soft X-Rays at 2.7 nm Using High Harmonics". *Physical Review Letters*, 79(16):2967–2970, 1997.

[21] H Mashiko, A Suda, and K Midorikawa. "Focusing coherent soft-x-ray radiation to a micrometer spot size with an intensity of 10^{14} W cm^{-2}". *Optics Letters*, 29(16):1927–1929, 2004.

[22] M Nisoli, G Sansone, S Stagira, S De Silvestri, C Vozzi, M Pascolini, L Poletto, P Villoresi, and G Tondello. "Effects of carrier-envelope phase differences of few-optical-cycle light pulses in single-shot high-order-harmonic spectra". *Physical Review Letters*, 91(21):213905, 2003.

[23] S. L. Stebbings, E. T. F. Rogers, A. M. De Paula, M. Praeger, C. A. Froud, B. Mills, D. C. Hanna, J. J. Baumberg, W. S. Brocklesby, and J. G. Frey.

"Molecular variation of capillary-produced soft x-ray high harmonics". *Journal of Physics B: Atomic, Molecular and Optical Physics*, 41:145602, 2008.

[24] Bing Shan, Xiao-Min Tong, Zengxiu Zhao, Zenghu Chang, and C. D. Lin. "High-order harmonic cutoff extension of the O_2 molecule due to ionization suppression". *Physical Review A*, 66(6):061401, 2002.

[25] C Altucci, R Velotta, JP Marangos, E Heesel, E Springate, M Pascolini, L Poletto, P Villoresi, C Vozzi, G Sansone, M Anscombe, JP Caumes, S Stagira, and M Nisoli. "Dependence upon the molecular and atomic ground state of higher-order harmonic generation in the few-optical-cycle regime". *Physical Review A*, 71(1):013409, 2005.

[26] JP Marangos, C Altucci, R Velotta, E Heesel, E Springate, M Pascolini, L Poletto, P Villoresi, C Vozzi, G Sansone, M Anscombe, JP Caumes, S Stagira, and M Nisoli. "Molecular orbital dependence of high-order harmonic generation". *Journal of Modern Optics*, 53:97–111, 2006.

[27] S. X. Hu and L. A. Collins. "Attosecond Pump Probe: Exploring Ultrafast Electron Motion inside an Atom". *Physical Review Letters*, 96(7):073004, 2006.

[28] T Pfeifer, C Spielmann, and G Gerber. "Femtosecond x-ray science". *Reports on Progress in Physics*, 69(2):443–505, 2006.

[29] E N Ragozin and I I Sobel'man. "Laser sources in the soft X-ray spectral region". *Physics — Uspekhi*, 48(12):1249–1250, 2005.

[30] G Sansone, E Benedetti, F Calegari, C Vozzi, L Avaldi, R Flammini, L Poletto, P Villoresi, C Altucci, R Velotta, S Stagira, S De Silvestri, and M Nisoli. "Isolated single-cycle attosecond pulses". *Science*, 314(5798):443–446, 2006.

[31] "FLASH website". [Online] `http://flash.desy.de/` [29/08/2008], 2008.

[32] "FLASH HASYLAB website". [Online] `http://hasylab.desy.de/-facilities/flash/` [29/08/2008], 2008.

[33] "Diamond website". [Online] `http://www.diamond.ac.uk/` [29/08/2008], 2008.

[34] C Finot, F Parmigiani, P Petropoulos, and DJ Richardson. "Parabolic pulse evolution in normally dispersive fiber amplifiers preceding the similariton formation regime". *Optics Express*, 14(8):3161–3170, 2006.

[35] P Dupriez, C Finot, A Malinowski, JK Sahu, J Nilsson, DJ Richardson, KG Wilcox, HD Foreman, and AC Tropper. "High-power, high repetition rate picosecond and femtosecond sources based on Yb-doped fiber amplification of VECSELs". *Optics Express*, 14(21):9611–9616, 2006.

[36] A Malinowski, A Piper, JHV Price, K Furusawa, Y Jeong, J Nilsson, and DJ Richardson. "Ultrashort-pulse Yb3+-fiber-based laser and amplifier system producing $>$ 25 W average power". *Optics Letters*, 29(17):2073–2075, 2004.

[37] E Betzig, JK Trautman, TD Harris, JS Weiner, and RL Kostelak. "Breaking the diffraction barrier - optical microscopy on a nanometric scale". *Science*, 251(5000):1468–1470, 1991.

[38] RD Grober, TD Harris, JK Trautman, and E Betzig. "Design and implementation of a low-temperature near-field scanning optical microscope". *Review Of Scientific Instruments*, 65(3):626–631, 1994.

[39] DW Pohl, W Denk, and M Lanz. "Optical stethoscopy - image recording with resolution $\lambda/20$". *Applied Physics Letters*, 44(7):651–653, 1984.

[40] J. B. Pendry. "Negative Refraction Makes a Perfect Lens". *Physical Review Letters*, 85(18):3966–3969, 2000.

[41] M. Born and E. Wolf. *Principles of optics.* Pergamon Press Ltd., Oxford, 3rd edition, 1965.

[42] M. E. Haine and V. E. Cosslett. *The Electron Microscope: The Present State of the Art. Including a Chapter on Specimen Techniques and Applications*. Interscience Publishers, 1961.

[43] J. W. S. Hearle, J. T. Sparrow, and P. M. Cross. *The use of the scanning electron microscope*. Pergamon Press, Oxford, UK, 1972.

[44] R Neutze, R Wouts, D van der Spoel, E Weckert, and J Hajdu. "Potential for biomolecular imaging with femtosecond X-ray pulses". *Nature*, 406(6797):752–57, 2000.

[45] SP Hau-Riege, RA London, and A Szoke. "Dynamics of biological molecules irradiated by short x-ray pulses". *Physical Review E*, 69(5):051906, 2004.

[46] HN Chapman, A Barty, MJ Bogan, S Boutet, M Frank, SP Hau-Riege, S Marchesini, BW Woods, S Bajt, H Benner, RA London, E Plonjes, M Kuhlmann, R Treusch, S Dusterer, T Tschentscher, JR Schneider, E Spiller, T Moller, C Bostedt, M Hoener, DA Shapiro, KO Hodgson, D Van der Spoel, F Burmeister, M Bergh, C Caleman, G Huldt, MM Seibert, FRNC Maia, RW Lee, A Szoke, N Timneanu, and J Hajdu. "Femtosecond diffractive imaging with a soft-X-ray free-electron laser". *Nature Physics*, 2(12):839–43, 2006.

[47] G Webster and R Hilgenfeld. "Perspectives on Single Molecule Diffraction Using the X-Ray Free Electron Laser". *Single Molecules*, 3(1):63–68, 2002.

[48] Jianwei Miao, Keith O. Hodgson, and David Sayre. "An approach to three-dimensional structures of biomolecules by using single-molecule diffraction images". *Proceedings of the National Academy of Sciences of the United States of America*, 98(12):6641–6645, 2001.

[49] JR Fienup. "Reconstruction of an object from modulus of its fourier-transform". *Optics Letters*, 3(1):27–29, 1978.

[50] J. Miao, D. Sayre, and H. N. Chapman. "Phase retrieval from the magnitude of the Fourier transforms of nonperiodic objects". *Journal of the Optical Society of America A*, 15(6):1662–1669, 1998.

[51] S. Marchesini, H. He, H. N. Chapman, S. P. Hau-Riege, A. Noy, M. R. Howells, U. Weierstall, and J. C. H. Spence. "X-ray image reconstruction from a diffraction pattern alone". *Phys. Rev. B*, 68(14):140101, 2003.

[52] Henry N. Chapman, Anton Barty, Stefano Marchesini, Aleksandr Noy, Stefan P. Hau-Riege, Congwu Cui, Malcolm R. Howells, Rachel Rosen, Haifeng He, John C. H. Spence, Uwe Weierstall, Tobias Beetz, Chris Jacobsen, and David Shapiro. "High-resolution ab initio three-dimensional x-ray diffraction microscopy". *Journal of the Optical Society of America A*, 23(5):1179–1200, 2006.

[53] JW Miao, P Charalambous, J Kirz, and D Sayre. "Extending the methodology of X-ray crystallography to allow imaging of micrometre-sized non-crystalline specimens". *Nature*, 400(6742):342–344, 1999.

[54] M. Meckel, D. Comtois, D. Zeidler, A. Staudte, D. Pavicic, H. C. Bandulet, H. Pepin, J. C. Kieffer, R. Dorner, D. M. Villeneuve, and P. B. Corkum. "Laser-Induced Electron Tunneling and Diffraction". *Science*, 320(5882):1478–1482, 2008.

[55] S Baker, JS Robinson, CA Haworth, H Teng, RA Smith, CC Chirila, M Lein, JWG Tisch, and JP Marangos. "Probing proton dynamics in molecules on an attosecond time scale". *Science*, 312(5772):424–427, 2006.

[56] MI Stockman, MF Kling, U Kleineberg, and F Krausz. "Attosecond nanoplasmonic-field microscope". *Nature Photonics*, 1(9):539–544, 2007.

[57] CA Froud. *Designing a Nanoscale X-ray Source: Towards Single Molecule X-ray Scattering*. PhD thesis, University Of Southampton, 2007.

[58] EE Fill, SJ van Enk, J Zhang, and P Lambropoulos. "Stimulated Raman scattering in helium with soft-x-ray laser radiation". *Physical Review A*, 54(6):5374–5377, 1996.

[59] L Misoguti, IP Christov, S Backus, MM Murnane, and HC Kapteyn. "Nonlinear wave-mixing processes in the extreme ultraviolet". *Physical Review A*, 72(6):063803, 2005.

[60] R. M. Jenkins and R. W. J. Devereux. "Effect of field regeneration on the TEM_{00} transmission characteristics of a circular-section wave-guide". *Applied Optics*, 31(24):5086–5091, 1992.

[61] T. Pfeifer and M. C. Downer. "Direct experimental observation of periodic intensity modulation along a straight hollow-core optical waveguide". *Journal of the Optical Society of America B*, 24(5):1025–1029, 2007.

[62] Pascal Salières, Philippe Antoine, Armelle de Bohan, and Maciej Lewenstein. "Temporal and Spectral Tailoring of High-Order Harmonics". *Physical Review Letters*, 81(25):5544–5547, 1998.

[63] P. Dietrich, N. H. Burnett, M. Ivanov, and P. B. Corkum. "High-harmonic generation and correlated two-electron multiphoton ionization with elliptically polarized light". *Physical Review A*, 50(5):R3585–R3588, 1994.

[64] F. Lindner, W. Stremme, M. G. Schatzel, F. Grasbon, G. G. Paulus, H. Walther, R. Hartmann, and L. Struder. "High-order harmonic generation at a repetition rate of 100 kHz". *Physical Review A*, 68(1):013814, 2003.

[65] M. Lewenstein, P. Salières, and A. L'Huillier. "Phase of the atomic polarization in high-order harmonic-generation". *Physical Review A*, 52(6):4747–4754, 1995.

[66] B H. Bransden and C. J. Joachain. *Physics of atoms and molecules*. Prentice Hall, 2nd edition, 2003.

[67] L. V. Keldysh. "Ionization in the field of a strong electromagnetic wave". *Soviet Physics JETP*, 20(5):1307–1314, 1965.

[68] V. S. Popov. "Tunnel and multiphoton ionization of atoms and ions in a strong laser field (Keldysh theory)". *Physics — Uspekhi*, 47(9):855–885, 2004.

[69] M. V. Ammosov, N. B. Delone, and V. P. Kraĭnov. "Tunnel ionization of complex atoms and of atomic ions in an alternating electromagnetic field". *Soviet Physics JETP*, 64(6):1191–1194, 1986.

[70] TDG Walsh, FA Ilkov, JE Decker, and SL Chin. "The tunnel ionization of atoms, diatomic and triatomic-molecules using intense 10.6 μm radiation". *Journal of Physics B: Atomic, Molecular and Optical Physics*, 27(16):3767–3779, 1994.

[71] W. A. Bryan, S. L. Stebbings, E. M. L. English, T. R. J. Goodworth, W. R. Newell, J. McKenna, M. Suresh, B. Srigengan, I. D. Williams, I . C. E. Turcu, J. M. Smith, E. J. Divall, C. J. Hooker, and A. J. Langley. "Geometry- and diffraction-independent ionization probabilities in intense laser fields: Probing atomic ionization mechanisms with effective intensity matching". *Physical Review A*, 73(1):013407, 2006.

[72] A A Radzig and B M Smirnov. *Reference Data on Atoms, Molecules, and Ions*. Springer-Verlag, Berlin, 1985.

[73] S. Augst, D. D. Meyerhofer, D. Strickland, and S. L. Chin. "Laser ionization of noble gases by Coulomb-barrier suppression". *Journal of the Optical Society of America B*, 8(4):858–867, 1991.

[74] XM Tong, ZX Zhao, and CD Lin. "Theory of molecular tunneling ionization". *Physical Review A*, 66(3):033402, 2002.

[75] C Guo, M Li, JP Nibarger, and GN Gibson. "Single and double ionization of diatomic molecules in strong laser fields". *Physical Review A*, 58(6):R4271–R4274, 1998.

[76] S.G. Lias. "Ionization Energy Evaluation". In P.J. Linstrom and W.G. Mallard, editors, *NIST Chemistry WebBook, NIST Standard Reference Database Number 69*. National Institute of Standards and Technology, Gaithersburg MD, 20899 (`http://webbook.nist.gov`), 2005.

[77] E. A. J. Marcatili and R. A. Schmeltzer. "Hollow metallic and dielectric waveguides for long distance optical transmission and lasers". *Bell System Technical Journal*, 43:1783–1809, 1964.

[78] G Tempea and T Brabec. "Theory of self-focusing in a hollow waveguide". *Optics Letters*, 23(10):762–764, 1998.

[79] C. Courtois, A. Couairon, B. Cors, J.R. Marqués, and G. Mattieussent. "Propagation of intense ultrashort laser pulses in a plasma filled capillary tube: Simulations and experiments". *Physics Of Plasmas*, 8(7):3445–3456, 2001.

[80] Phillip M Morse and Herman Feshbach. *Methods Of Theoretical Physics*, volume 2, chapter 10, page 1322. McGraw-Hill Book Company Inc, New York, 1953.

[81] Julius Adams Stratton. *Electromagnetic theory*, chapter 9.15, page 254. McGraw-Hill Book Company Inc, New York, 1st edition, 1941.

[82] C. A. Froud, E. T. F. Rogers, D. C. Hanna, W. S. Brocklesby, M. Praeger, A. M. De Paula, J. J. Baumberg, and J. G. Frey. "Soft-x-ray wavelength shift induced by ionization effects in a capillary". *Optics Letters*, 31(3):374–376, 2006.

[83] M Praeger. *Development and spatio-spectral mapping of a capillary high harmonic source*. PhD thesis, University Of Southampton, 2007.

[84] A. Dalgarno and A. E. Kingston. "The Refractive Indices and Verdet Constants of the Inert Gases". *Proceedings of the Royal Society of London. Series A, Mathematical and Physical Sciences (1934-1990)*, 259(1298):424–431, 1960.

[85] E. R. Peck and B. N. Khanna. "Dispersion of nitrogen". *Journal of the Optical Society of America*, 56:1059–1063, 1966.

[86] C. Cuthbertson and M. Cuthbertson. "On the Refraction and Dispersion of the Halogens, Halogen Acids, Ozone, Steam, Oxides of Nitrogen and Ammonia". *Philosophical Transactions of the Royal Society of London. Series A, Containing Papers of a Math. or Phys. Character (1896-1934)*, 213:1–26, 1914.

[87] P. E. Ciddor. "Refractive index of air: 3. The roles of CO2, H2O, and refractivity virials". *Applied Optics*, 41(12):2292–2298, 2002.

[88] Atkins P. W. *Physical Chemistry*. Oxford University Press, Great Clarendon St, Oxford, UK, 6th edition, 1998.

[89] C.T. Chantler, K. Olsen, R.A. Dragoset, J. Chang, A.R. Kishore, S.A. Kotochigova, and D.S. Zucker. "X-Ray Form Factor, Attenuation and Scattering Tables (version 2.1)". [Online] Available: `http://physics.nist.gov/ffast` [2008, July 16], 2005. National Institute of Standards and Technology, Gaithersburg, MD. Originally published as [91, 92].

[90] B. L. Henke, E. M. Gullikson, and J. C. Davis. "X-ray interactions - photoabsorption, scattering, transmission and reflection at e=50-30,000 ev, z=1-92 (vol 54, pg 181, 1993)". *Atomic Data And Nuclear Data Tables*, 55(2):349–349, 1993.

[91] C. T. Chantler. "Detailed tabulation of atomic form factors, photoelectric absorption and scattering cross section, and mass attenuation coefficients in the vicinity of absorption edges in the soft X-ray (Z=30-36, Z=60-89, E=0.1 keV-

10 keV), addressing convergence issues of earlier work". *Journal Of Physical And Chemical Reference Data*, 29(4):597–1048, 2000.

[92] C. T. Chantler. "Theoretical form-factor, attenuation and scattering tabulation for z=1-92 from e=1-10 ev to e=0.4-1.0 mev". *Journal Of Physical And Chemical Reference Data*, 24(1):71–591, 1995.

[93] Orazio Svelto. *Principles of Lasers*. Kluwer Academic / Plenum Publishers, 4th edition, 1998.

[94] J. Bokor, P. H. Bucksbaum, and R. R. Freeman. "Generation of 35.5-nm coherent radiation". *Optics Letters*, 8(4):217–219, 1983.

[95] A. McPherson, G. Gibson, H. Jara, U. Johann, T. S. Luk, I. A. McIntyre, K. Boyer, and C. K. Rhodes. "Studies of multiphoton production of vacuum-ultraviolet radiation in the rare gases". *Journal of the Optical Society of America B*, 4(4):595–601, 1987.

[96] M Ferray, A L'Huillier, X F Li, L A Lompre, G Mainfray, and C Manus. "Multiple-harmonic conversion of 1064 nm radiation in rare gases". *Journal of Physics B: Atomic, Molecular and Optical Physics*, 21(3):L31–35, 1988.

[97] XF Li, A L'Huillier, M Ferray, LA Lompré, and G Mainfray. "Multiple-harmonic generation in rare-gases at high laser intensity". *Physical Review A*, 39(11):5751–5761, 1989.

[98] K. C. Kulander and B. W. Shore. "Calculations of Multiple-Harmonic Conversion of 1064-nm Radiation in Xe". *Physical Review Letters*, 62(5):524–526, 1989.

[99] BW Shore and KC Kulander. "Generation of optical harmonics by intense pulses of laser-radiation I. Propagation effects". *Journal of Modern Optics*, 36(7):857–75, 1989.

[100] K. C. Kulander and B. W. Shore. "Generation of optical harmonics by intense pulses of laser radiation II. Single-atom spectrum for xenon". *Journal of the Optical Society of America B*, 7(4):502, 1990.

[101] R. M. Potvliege and Robin Shakeshaft. "Multiphoton processes in an intense laser field: Harmonic generation and total ionization rates for atomic hydrogen". *Physical Review A*, 40(6):3061–3079, 1989.

[102] J. H. Eberly, Q. Su, and J. Javanainen. "Nonlinear Light Scattering Accompanying Multiphoton Ionization". *Physical Review Letters*, 62(8):881–884, 1989.

[103] J. H. Eberly, Q. Su, and J. Javanainen. "High-order harmonic production in multiphoton ionization". *Journal of the Optical Society of America B*, 6(7):1289–1298, 1989.

[104] Gunadya Bandarage, Alfred Maquet, and J. Cooper. "Harmonic generation by a classical hydrogen atom in the presence of an intense radiation field". *Physical Review A*, 41(3):1744–1746, 1990.

[105] W. Becker, S. Long, and J. K. McIver. "Higher-harmonic production in a model atom with short-range potential". *Physical Review A*, 41(7):4112–4115, 1990.

[106] Bala Sundaram and Peter W. Milonni. "High-order harmonic generation: Simplified model and relevance of single-atom theories to experiment". *Physical Review A*, 41(11):6571–6573, 1990.

[107] A L'Huillier, P Balcou, S Candel, KJ Schafer, and KC Kulander. "Calculations of high-order harmonic-generation processes in xenon at 1064 nm". *Physical Review A*, 46(5):2778–2790, 1992.

[108] IP Christov. "Propagation of ultrashort pulses in gaseous medium: breakdown of the quasistatic approximation". *Optics Express*, 6(2):34–9, 2000.

[109] Ivan P. Christov. "Control of high harmonic and attosecond pulse generation in aperiodic modulated waveguides". *Journal of the Optical Society of America B*, 18(12):1877–1881, 2001.

[110] A. L'Huillier, K. J. Schafer, and K. C. Kulander. "High-order harmonic generation in xenon at 1064 nm: the role of phase matching". *Physical Review Letters*, 66(17):2200–2203, 1991.

[111] P. Salieres, A. L'Huillier, and M. Lewenstein. "Coherence control of high-order harmonics". *Physical Review Letters*, 74(19):3776–3779, 1995.

[112] C. Altucci, R. Bruzzese, C. de Lisio, M. Nisoli, E. Priori, S. Stagira, M. Pascolini, L. Poletto, P. Villoresi, V. Tosa, and K. Midorikawa. "Phase-matching analysis of high-order harmonics generated by truncated Bessel beams in the sub-10-fs regime". *Physical Review A*, 68:033806, 2003.

[113] Ivan P. Christov, Henry C. Kapteyn, and Margaret M. Murnane. "Quasi-phase matching of high-harmonics and attosecond pulses in modulated waveguides". *Optics Express*, 7(11):362–367, 2000.

[114] PL Shkolnikov, A Lago, and AE Kaplan. "Optimal quasi-phase-matching for high-order harmonic-generation in gases and plasma". *Physical Review A*, 50(6):R4461–R4464, 1994.

[115] T Auguste, B Carre, and P Salieres. "Quasi-phase-matching of high-order harmonics using a modulated atomic density". *Physical Review A*, 76(1):011802(R), 2007.

[116] A Paul, EA Gibson, XS Zhang, A Lytle, T Popmintchev, XB Zhou, MM Murnane, IP Christov, and HC Kapteyn. "Phase-matching techniques for coherent soft X-ray generation". *IEEE Journal of Quantum Electronics*, 42:14–6, 2006.

[117] G Tempea, M Geissler, M Schnurer, and T Brabec. "Self-phase-matched high harmonic generation". *Physical Review Letters*, 84(19):4329–332, 2000.

[118] Charles G. Durfee III, Andy R. Rundquist, Sterling Backus, Catherine Herne, Margaret M. Murnane, and Henry C. Kapteyn. "Phase matching of high-order harmonics in hollow waveguides". *Physical Review Letters*, 83(11):2187–2190, 1999.

[119] AN Naumov, AM Zheltikov, AB Fedotov, DA Sidorov-Biryukov, AP Tarasevitch, P Zhou, and D von der Linde. "Pressure control of phase matching in high-order harmonic generation in hollow fibers filled with an absorbing weakly ionizing gas". *Journal of the Optical Society of America B*, 18(6):811–817, 2001.

[120] AN Naumov, AM Zheltikov, AB Fedotov, DA Sidorov-Biryukov, AP Tarasevitch, P Zhou, and D Von der Linde. "Ionization and absorption effects in high-order harmonic generation in gas-filled hollow fibers". *Laser And Particle Beams*, 19(1):75–79, 2001.

[121] M. Nisoli, S. Stagira, S. De Silvestri, O. Svelto, S. Sartania, Z. Cheng, G. Tempea, C. Spielmann, and F. Krausz. "Toward a terawatt-scale sub-10-fs laser technology". *IEEE Journal of selected topics in quantum electronics*, 4(2):414–420, 1998.

[122] M Uiberacker, T Uphues, M Schultze, AJ Verhoef, V Yakovlev, MF Kling, J Rauschenberger, NM Kabachnik, H Schroder, M Lezius, KL Kompa, HG Muller, MJJ Vrakking, S Hendel, U Kleineberg, U Heinzmann, M Drescher, and F Krausz. "Attosecond real-time observation of electron tunnelling in atoms". *Nature*, 446(7136):627–632, 2007.

[123] A. E. Siegman, G. Nemes, and J. Serna. "How to (Maybe) Measure Laser Beam Quality". In M. Dowley, editor, *DPSS (Diode Pumped Solid State) Lasers: Applications and Issues*, volume 17 of *OSA Trends in Optics and Photonics*, page MQ1. Optical Society of America, 1998.

[124] K. W. DeLong, Rick Trebino, J. Hunter, and W. E. White. "Frequency-resolved optical gating with the use of second-harmonic generation". *Journal of the Optical Society of America B*, 11(11):2206–2215, 1994.

[125] DJ Kane and R Trebino. "Characterization of arbitrary femtosecond pulses using frequency-resolved optical gating". *IEEE Journal of Quantum Electronics*, 29(2):571–579, 1993.

[126] DJ Kane and R Trebino. "Single-shot measurement of the intensity and phase of an arbitrary ultrashort pulse by using frequency-resolved optical gating". *Optics Letters*, 18(10):823–825, 1993.

[127] C. Iaconis and I.A. Walmsley. "Spectral phase interferometry for direct electric-field reconstruction of ultrashort optical pulses". *Optics Letters*, 23(10):792–794, 1998.

[128] Ariel Gordon and Franz X. Kärtner. "Quantitative Modeling of Single Atom High Harmonic Generation". *Physical Review Letters*, 95:223901, 2005.

[129] F. Dorchies, J. R. Marquès, B. Cros, G. Matthieussent, C. Courtois, T. Vélikoroussov, P. Audebert, J. P. Geindre, S. Rebibo, G. Hamoniaux, and F. Amiranoff. "Monomode Guiding of 10^{16} W cm^{-2} Laser Pulses over 100 Rayleigh Lengths in Hollow Capillary Dielectric Tubes". *Physical Review Letters*, 82(23):4655–4658, 1999.

[130] Nicholas L. Wagner, Emily A. Gibson, Tenio Popmentchev, Ivan P. Christov, Margaret M. Murnane, and Henry C. Kapteyn. "Self-Compression of Ultrashort Pulses through Ionization-Induced Spatiotemporal Reshaping". *Physical Review Letters*, 93(17), 2004.

[131] Okan K. Ersoy. *Diffraction, Fourier Optics and Imaging.* Wiley, 2007.

[132] A. E. Siegman. *Lasers*, chapter 16, page 661. University Science Books, Sausalito, CA, USA, 1986.

[133] M Guizar-Sicairos and JC Gutiérrez-Vega. "Computation of quasi-discrete Hankel transforms of integer order for propagating optical wave fields". *Journal of the Optical Society of America A*, 21(1):53–58, 2004.

[134] Adam Wyatt. "MATLAB Central File Exchange - Hankel Transform". [Online] `http://www.mathworks.com/matlabcentral/fileexchange/-loadFile.do?objectId=15623&objectType=file` [19/08/2008], 2007.

[135] O. A. Kolevatova, A. N. Naumov, and A. M. Zheltikov. "Guided high-intensity laser pulses through hollow fibers: self-phase modulation and cross-talk of guided modes". *Optics Communications*, 217:169–177, 2003.

[136] D Homoelle and AL Gaeta. "Nonlinear propagation dynamics of an ultrashort pulse in a hollow waveguide". *Optics Letters*, 25(10):761–63, 2000.

[137] V Tosa, A Bende, TD Silipas, HT Kim, and CH Nam. "Modelling plasma fluorescence induced by femtosecond pulse propagation in ionizing gases". *Romanian Journal of Physics*, 50(7):741–748, 2005.

[138] M Lax, JH Batteh, and GP Agrawai. "Channeling of intense electromagnetic beams". *Journal of Applied Physics*, 52(1):109–125, 1981.

[139] M Mlejnek, EM Wright, and JV Moloney. "Femtosecond pulse propagation in argon: A pressure dependence study". *Physical Review E*, 58(4):4903–4910, 1998.

[140] SC Rae and K Burnett. "Detailed simulations of plasma-induced spectral blueshifting". *Physical Review A*, 46(2):1084–1090, 1992.

[141] AA Babin, DV Kartashov, AM Kiselev, VV Lozhkarev, AN Stepanov, and AM Sergeev. "Ionization spectrum broadening and frequency blue-shift of high-intensity femtosecond laser pulses in gas-filled capillary tubes". *Applied Physics B: Lasers and Optics*, 75:509–514, 2002.

[142] G Tempea and T Brabec. "Nonlinear source for the generation of high-energy few-cycle optical pulses". *Optics Letters*, 23(16):1286–1288, 1998.

[143] NE Andreev, B Cros, G Maynard, P Mora, and F Wojda. "Coupling efficiency of intense laser pulses to capillary tubes for laser wakefield acceleration". *IEEE Transactions on Plasma Science*, 36(4):1746–1750, 2008.

[144] Govind Agrawal. *Nonlinear Fiber Optics*. Academic Press Inc.(London) Ltd, 3rd edition, 2001.

[145] RK Nubling and JA Harrington. "Launch conditions and mode coupling in hollow-glass waveguides". *Optical Engineering*, 37(9):2454–2458, 1998.

[146] M Zepf, B Dromey, M Landreman, P Foster, and SM Hooker. "Bright quasi-phase-matched soft-x-ray harmonic radiation from argon ions". *Physical Review Letters*, 99(14):143901, 2007.

[147] B Dromey, M Zepf, M Landreman, and SM Hooker. "Quasi-phasematching of harmonic generation via multimode beating in waveguides". *Optics Express*, 15(13):7894–7900, 2007.

[148] F. Poletti and P. Horak. "Description of ultrashort pulse propagation in multimode optical fibers". *Journal of the Optical Society of America B*, 25(10):1645–1654, 2008.